Search for Heavy Stable Charged Particles at CMS Using Tracker dE/dx Measurement

BY

Jie Chen

Submitted to the graduate degree program in Physics
and the Graduate Faculty of the University of Kansas
in partial fulfillment of the requirements for the degree of
Doctor of Philosophy.

_____
Chairperson

Committee members* _____ *

_____ *

_____ *

_____ *

Date defended: _____

The Dissertation Committee for Jie Chen certifies
that this is the approved version of the following dissertation:

Search for Heavy Stable Charged Particles at CMS Using

Tracker dE/dx Measurement

Committee:

_____
Chairperson∗

_____

_____

_____

_____

Date approved: _____

To My Little Angel — Kaye

All truths are easy to understand once they are discovered; the point is to discover them.

—Galileo Galilei

Contents

List of Figures

List of Tables

Acknowledgements

It's a long and winding journey for me to reach the point to write down this Ph.D. dissertation. Through my graduate school life, I benefit intellectually from lots of great and nice people from BES, CLEO, and CMS collaborations.

First of all, I would like to thank my dissertation advisor Prof. Alice Bean for her excellent supervision on this dissertation. It's Prof. Bean who gives me all those precious opportunities to touch all the aspects of the CMS experiment. She lets me start with the power supply burn-in system setup and test software development. The burn-in system is for the detector control system (DCS) of the silicon strip tracker. Then we exported our experience on DCS data analysis to web based monitoring software development at FNAL. Meanwhile we also make the online tracker display better by developing a user-friendly control panel inside online PVSS environment. The OnlineDBLoader package we developed later in CMSSW enables the CMS detector geometry to be loaded to Online database in an efficient manner. This facilities the online 3D PVSS displaying to read the up to date geometry. We also made a better tracker calibration possible by developing the DCS data online to offline transfer CMSSW package. All these service work made me understand in detail how the CMS detector works in both hardware and

software ways. These knowledge made a sound foundation for heavy stable charge particle study and Tracker Integration Facility (TIF) dE/dx analysis, which turn out to be this dissertation. Prof. Bean also helped me a lot in my life. I still clearly remember the joyful baby shower for my little daughter Kaye, at Prof. Bean's home.

I would also thank Prof. Frank Hartmann (Universitat Karlsruhe) for supervising me on DCS power supply burn-in and online PVSS control panel software development. It's fun and productive when I work with him at CERN. DCS group is like a family, we have dinner and play board game together. I learned a lot from Frank in effectively cooperating with people from around the world.

Thanks also should be given to Michael Case (UC-Davis) and Frank Glege (CERN) for their help on understanding CMS geometry and developing OnlineDBLoader CMSSW package, Giacomo Bruno (UCL) and Marcin Bogusz (CERN) in developing SiStripDCS CMSSW package, Andrea Rizzi (ETH) for his help on HSCP analysis, and Carsten Noeding (FNAL) for the help on TIF data analysis.

I am also grateful to my dissertation committee: Prof. Phil Baringer, Prof. Brian Laird, Prof. Danny Marfatia, and Prof. Graham Wilson for their useful inputs.

I must acknowledge my two former advisers: Prof. Roy Briere and Prof. Xue-qian Li. They lead me into the fascinating world of experimental particle physics, and helped me develop the solid theoretical understanding and experimental techniques. These are valuable assets for my research at CMS.

I would also like to acknowledge those people from CLEO and BES collab-

orations who had major influences on my research learning. They're Prof. Helmut Vogel, Dr. Guangpei Chen, Dr. Feng Liu, Dr. Michael Watkins, Prof. Yucan Zhu, Prof. Bingsong Zou, Dr. Shuangshi Fang, and Dr. Xiaobin Ji.

I would express my deepest appreciation for Rachel (Xin in Chinese), my soul-mate, for always being there for me.

Finally, last but surely not the least, I thank my family for their love and continuous support.

Abstract

This dissertation starts with an overview of the physics of heavy stable charged particles, which arise in various models beyond the standard model like supersymmetry and universal extra dimensions. Then it describes the current experimental status on searching for these particles. The main content of this dissertation is discussing the physics potential of the compact muon solenoid (CMS) detector at the large hadron collider (LHC) in detecting such high-mass particles, primarily using dE/dx information from the silicon strip tracker system of CMS, based on Monte-Carlo simulation data. Cosmic data from the Tracker Integration Facility is also used to better understand the performance of tracker dE/dx measurements.

Chapter 1

Theoretical Models and Previous Experiments

1.1 Introduction

Many models beyond standard model suggest the existence of a heavy stable charged particle (HSCP) like, staus in the Gauge Mediated Supersymmetry Breaking (GMSB) model [1], R hadrons in the split supersymmetry model [2], Kaluza-Klein (KK) leptons in the Minimal Universal Extra Dimension (MUED) model [3], and stops in the Minimal Standard Supersymmetric Model (MSSM) [4]. The possibility of an absolutely heavy stable charged particle is constrained by cosmological considerations. But long-lived particles on an experimental scale ($<$ 100 ns) are only constrained by direct searches. By stable, we refer to lifetimes long enough to escape the detector before decaying.

1.2 Standard Model

The Standard Model (SM) of particle physics [5] is a SU(3)×SU(2)×U(1) gauge field theory which describes three fundamental interactions (electromagnetic, strong, and weak) between the elementary particles (quarks, leptons, and gauge bosons) that make up all matter. To date, almost all experimental tests of the three forces described by the Standard Model have agreed with its predictions.

However, new physics beyond the SM is still expected, primarily due to several theoretical arguments. First, the SM lacks the inclusion of gravity. Second, an explanation of the gauge hierarchy problem (the smallness of M_Z/M_{Planck}, or the question of why the weak force is 10^{32} times stronger than gravity) demands new physics at the TeV-scale [6]. Third, unification of the three gauge couplings at the Planck scale does not occur in the SM. Fourth, the existence of dark matter and dark energy, which make up 96% of the energy density of the universe [7], cannot be explained by the SM.

1.3 Supersymmetry

Supersymmetry is the most popular theoretical model beyond the standard model. It encompasses gauge coupling unification. Its light super particle is a natural candidate for dark matter, and it has an elegant solution to the so-called hierarchy problem. But so far little is known about the nature of the SUSY-breaking mechanism, therefore, there are lots of variants of supersymmetry models.

In supersymmetry models, all Standard Model particles have partner particles with the same quantum numbers but spin differing by $1/2\hbar$. The partner of a fermion is called s-fermion, and the partner of a quark is called s-quark. The partner of a boson is named with a suffix -ino, so the superpartners of the Z boson, photon, and neutral Higgs are expressed as zino, bino, and higgsino, respectively. The zino, photino and higgsino can mix to form four eigenstates of the mass operator called "neutralinos". In many models the lightest of the four neutralinos turns out to be the lightest supersymmetric particle (LSP).

1.3.1 Minimal Supersymmetric Standard Model

The Minimal Supersymmetric Standard Model (MSSM) is defined in a way which contains all possible SUSY-breaking interactions, which are consistent with gauge and Poincaré invariance, and which do not cause the hierarchy problem to reappear (so-called soft SUSY-breaking).

The MSSM possesses 124 independent free parameters in total [8], and essentially allows any sparticle to be a heavy stable particle. In models with the neutralino as the LSP, the next to lightest sparticle (NLSP) can be long-lived if its decay phase space is small or zero. An interesting scenario here is that of a light stop ($\tilde{t}_1$) NLSP, as motivated by electroweak baryogenesis [4], a model which explains the baryon asymmetry of the Universe at the electroweak phase transition in the Minimal Supersymmetric Standard Model, in the presence of light stops. In this scenario non-universal squark mass terms are used to arrange a small mass difference between the $\tilde{t}_1$ and the LSP $\tilde{\chi}_1^0$

, while the lightest chargino is kept too heavy for the decay $\tilde{t}_1 \rightarrow \tilde{b}_1\tilde{\chi}_1^+$ to occur. In this case, $\tilde{t}_1$ can only decay via the radiative process $\tilde{t}_1 \rightarrow \tilde{c}_1\tilde{\chi}_1^0$, thus $\tilde{t}_1$ can become long-lived.

Another interesting scenario in which a stop would be stable (actually the LSP), can be obtained by breaking the electroweak symmetry and supersymmetry by a compact extra dimension [9]. In this case, the favored stop mass range is between 130 and 800 GeV.

Stop production in hadron collisions proceeds mainly via the coupling of the stop to the gluon. Therefore the production is basically model independent and depends only on the strong coupling constant (α_s) and the stop mass. Fig. 1.1 shows the leading order Feynman diagrams for stop pair production [10, 11].

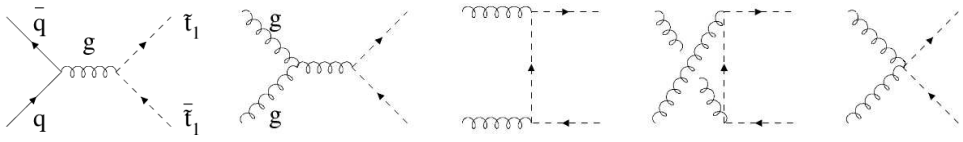

Figure 1.1: Stop production modes at large hadron collider (LHC).

1.3.2 Gauge Mediated Supersymmetry Breaking

In Gauge Mediated SUSY-breaking (GMSB) [1], the gravitino is very light ($m_G < 1$ keV) and hence the LSP for any relevant choice of parameters. Minimal models are cast in terms of six parameters, typically N, Λ, M, $tan\beta$, sgn(μ), and c_{grav} . The meaning of these parameters is that N chiral SU(5) multiplets are added to the theory at the scale M $\sim 10^{15}$ GeV. If not only

SU(5) multiplets are added, the counting gets more complicated, but there is still an effective N. These "messengers" couple directly both to the MSSM fields (via the ordinary SM gauge interactions) and also to an unspecified source of SUSY-breaking. $\Lambda = 10 \sim 100$ TeV is the effective SUSY-breaking scale, related to the fundamental SUSY-breaking scale F by a relation $\Lambda =$ F/M. The next-to-lightest sparticle decays only via the gravitational coupling and can be very long-lived. In a tiny and near-excluded parameter region at small values of the model parameters Λ and M, the NLSP is a sneutrino, otherwise it is the $\tilde{\tau}_1$.

Fig. 1.2 from Ref. [12] shows the smallest messenger index N required to have a $\tilde{\tau}_1$ NLSP for $\mu > 0$, as a function of $tan\beta$ and Λ. The term c_{grav}, which is the factor multiplying effective mass of gravitino, is unspecified because it only affects the decay. Only the light grey areas at small Λ are theoretically excluded due to unstable vacua and/or non-perturbative couplings at the GUT scale.

In spite of the large parameter space for a long-lived $\tilde{\tau}_1$, it is still not the only stable massive particle possibility in GMSB. If the mixing and consequently the mass splitting in the stau sector is not too large (small $tan\beta <$ 8), then the $\tilde{e}_1$ and $\tilde{\mu}_1$ may be nearly mass-degenerate (co-NLSP) with the $\tilde{\tau}_1$ and hence can simultaneously be a stable massive particle.

Production of the stau can proceed directly via a virtual photon or Z or via production of heavier supersymmetric particles (mainly squarks and gluino pairs). In the latter case, which is in general dominant due to the electroweak nature of the direct production process, one or more stau will appear in the final state as final products of the decay chain of sparticles.

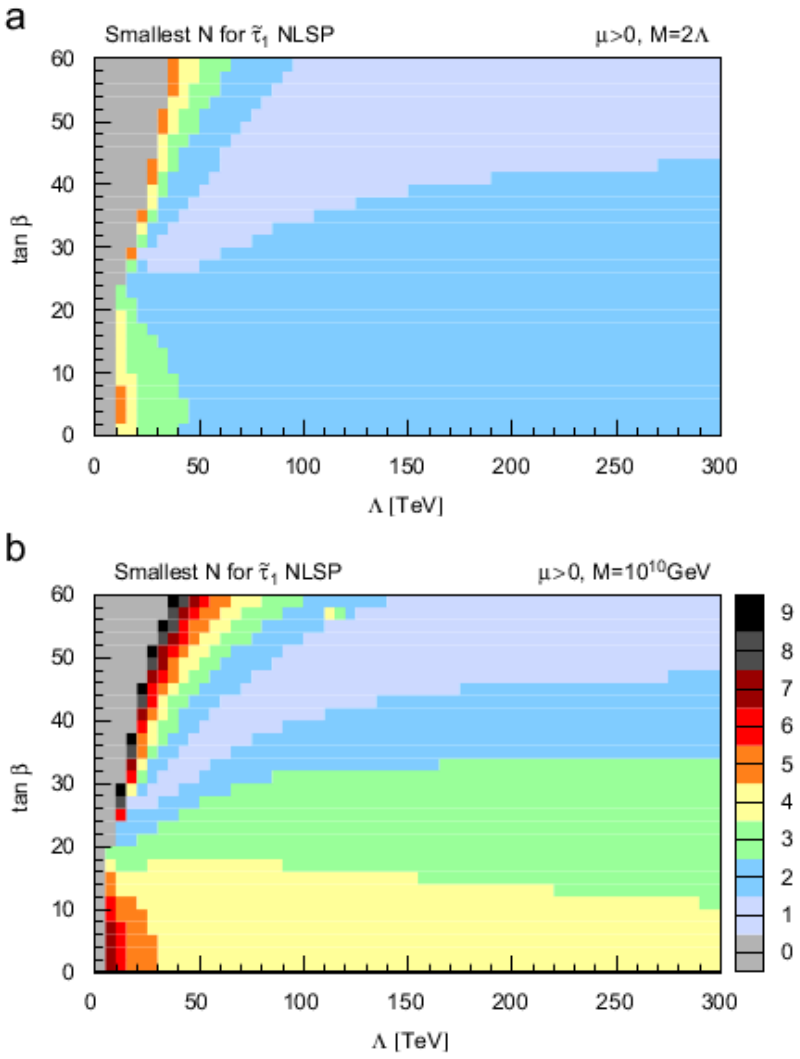

Figure 1.2: GMSB: the smallest index number N required to obtain a $\tilde{\tau}_1$ NLSP as a function of Λ and $tan\beta$ for (a) light messengers (M = 2 Λ) and (b) heavy messengers (M = 10^{10} GeV). The color coding is the same for both plots and corresponds to the legend shown with (b). See text for reference.

For non-minimal GMSB models, like SUSY GUT extensions of GMSB [13], the colored messengers are naturally much heavier than their Weak counterparts, resulting in a gluino $\tilde{g}$ NLSP or even LSP, depending on the gravitino mass. Since gluinos can only decay via squarks, the gluino lifetime can be very large in this scenario. The gluino may also be hadronized to a hadron-like particle ($\tilde{g}u\bar{d}$ for example) inside the detector by picking up some Standard Model quarks. These particles are named R-hadrons, where the 'R' refers to the fact that they can only be stable hadrons if R-parity (defined as R = $(-1)^{2j+3B+L}$, with spin j, baryon number B, and lepton number L. All Standard Model particles have R-parity of 1 while supersymmetric particles have R-parity -1) is conserved. R-hadrons can consist of any colored squarks C_3 ($\tilde{u}$, $\tilde{d}$, $\tilde{c}$, etc..) or color octet C_8 (8 types of $\tilde{g}$ which carries both a color and a different anticolor). Therefore, we can get lots of R-hadrons such as $C_3\bar{q}$, C_3qq, $\bar{C}_3q$, $C_8q\bar{q}$, C_8qqq and C_8g. These are all the combinations a R-hadron can have due to the fact that it has to be color singlet (or colorless).

R-hadrons are strongly interacting massive particles, electrically either neutral or charged. A neutral R-hadron may convert into a charged hadron when the internal light quark or gluon is knocked off and replaced by another light quark and vice versa. This is called the charge flipping effect for R-hadrons. The probability of such a scattering depends crucially on the mass spectrum of the hadrons formed by the gluino and light quarks and gluons. If the hadron is electrically charged, it also undergoes ionization energy loss in the detector.

1.3.3 Split Supersymmetry

Other non-GMSB SUSY models like split SUSY [2] also predict the existence of R-hadrons.

In Split SUSY, all the SUSY scalar particles have very large masses, while only the gaugino and the higgsino masses are relatively much lighter and still around the Weak scale (order of TeV). Split SUSY can be viewed as a subset of the MSSM in a certain parameter space. The most distinct feature of the theory is that the gluino becomes stable [14], because all the sfermions are very heavy and gluinos can only decay to the LSP via a virtual sfermion. The gluino produced in this scenario will also hadronize into a R-hadron. Due to the high squark masses, split SUSY Gluino production at the LHC depends only on the gluino mass and is dominated by the $g + g \rightarrow \tilde{g} + \tilde{g}$ process, as shown in Fig. 1.3. The process $q + \bar{q} \rightarrow \tilde{g} + \tilde{g}$ contributes only a small fraction of the total crosssection. Take a 200 GeV gluino as an example, the gg process has a cross section of about 2 nb while the $q\bar{q}$ contribution is only about 0.1 nb at LHC.

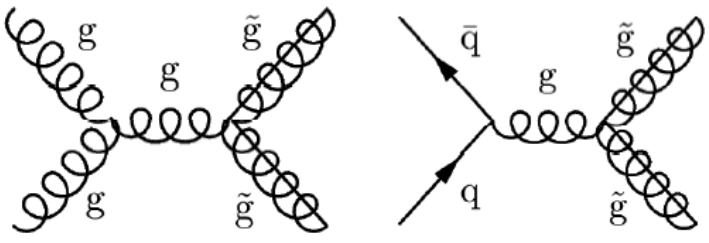

Figure 1.3: Gluino production modes at LHC.

1.4 Extra Dimensions

Extra dimensions were proposed in 1914 by Gunar Nordstrom [15], with the aim to unify the electromagnetic force and gravity, the two fundamental forces known at that time. In 1919 Theodor Kaluza [16] found that the 5-dimensional generalization of Einstein's theory can simultaneously describe the electromagnetic force and gravity. Oskar Klein [17] applied Kaluza's theory to quantum theory and explained the physical meaning of the compacted extra dimension. More recently, people realized that extra dimensions with a size of order TeV^{-1} can solve the hierarchy problem [18]. This results in direct implications for collider experiments.

1.4.1 Standard Model Fields in Extra Dimensions

Not only gravity, but also Standard Model fields could live in the extra dimensions [19]. Universal extra dimensions [20] (UED) is such a model in which all SM particles uniformly propagate in extra dimensions of size $R^{-1} \sim$ TeV. It predicts that for all SM particles there exist corresponding Kaluza Klein (KK) states in extra dimensions. They have the same quantum numbers and spins as their SM partners. The masses of KK states follow approximately

$$m_n^2 \sim m_0^2 + n^2/R^2 + \text{boundary terms}, \tag{1.1}$$

where n is the KK excitation level, R is the radius of extra dimensions, and m_0 is the SM partner mass. All KK states conserve a KK parity symmetry, which makes the lightest KK state stable. This lightest KK particle (LKP)

becomes naturally a dark matter candidate. UED also holds that the first KK mode is always pair-produced and looks quite like SUSY. The LKP is normally a KK photon, but it also can be a KK graviton [21].

1.4.2 Minimum Universal Extra Dimension

Instead of an indefinite number of extra dimensions of UED, the Minimum Universal Extra Dimensions (MUED) theory is defined in 4+1 dimensions, with only 3 free parameters R, Λ (cut off scale in MUED) and m_{higgs} (SM higgs mass). KK masses are degenerate at tree level, and mass splitting is introduced from radiative corrections. Here the KK lepton l^1 decays by $l^1 \rightarrow l^0 + \gamma^1$, where γ^1 is the lightest KK photon (LKP in UED) and l^0 is the SM lepton.

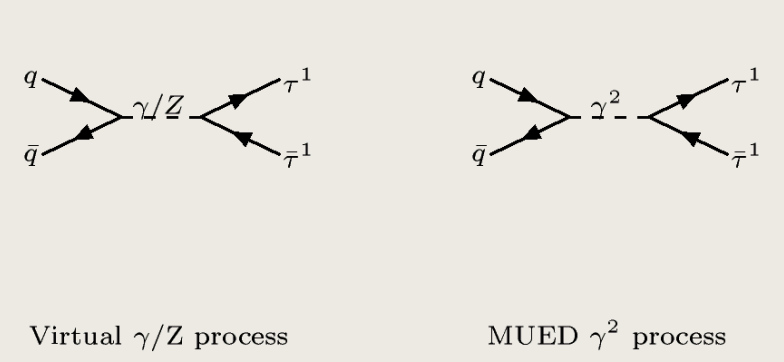

Figure 1.4: KK-tau production modes at LHC.

For a certain (Λ, R) parameter space, the mass splitting can become less than the SM lepton mass. Here, the KK leptons thus can only decay via virtual SM W, such as $\mu^1 \rightarrow \gamma^1 + \nu_\mu^0 + \bar{\nu_e^0} + e^0$. Thus, the μ^1's lifetime becomes longer than the life time of the SM μ [3], and becomes one kind of

lepton-like HSCP. From experimental limits (direct search and EW precision measurement constraints), $R^{-1} <\sim 300$ GeV [22] or 250 GeV [23] assuming a heavy higgs. The parameter space allowed for the KK lepton is very narrow. As shown in Appendix A.1, only a right-handed KK τ with mass ~ 300 GeV can become a candidate for HSCP.

The KK tau at LHC is mainly pair-produced, through a virtual photon/Z, or a second level of KK photon (γ^2, where n=2 in Eq. 1.1), as shown in Fig. 1.4.

1.5 Comparison between Models

As seen from the previous discussion, there are mainly two categories of HSCPs among these beyond standard models: lepton-like(e.g. stau in mGMSB and KK tau in MUED) and hadron-like (e.g. R-hadron in Split SUSY and stop in MSSM). Most models suggest HSCPs are pair-produced (to conserve R parity in SUSY or KK parity in UED). Hadron-like HSCPs may undergo hadronization (forming "R-hadrons" by picking up standard model partons) or inelastic scattering from the nuclei of the material in the detector and may deposit large amounts of energy in the calorimeters. The interactions for hadron-like HSCPs in material are often model dependent. Several different theoretical models [12] of R-hadron interaction are shown in Fig. 1.5. We see that although different models predict different energy loss for the R-hadron, the value is always around a few GeV energy per hadronic interaction. The physics behind it is that the heavy parton (gluino or stop) acts only as a spectator, only behaving as a reservoir of kinetic energy. The

kinetic energy available to each hadronic interaction is considered to be only a small fraction of the total energy, proportional to the mass fraction of light partons to spectator. This means we won't expect a large shower in the calorimeters.

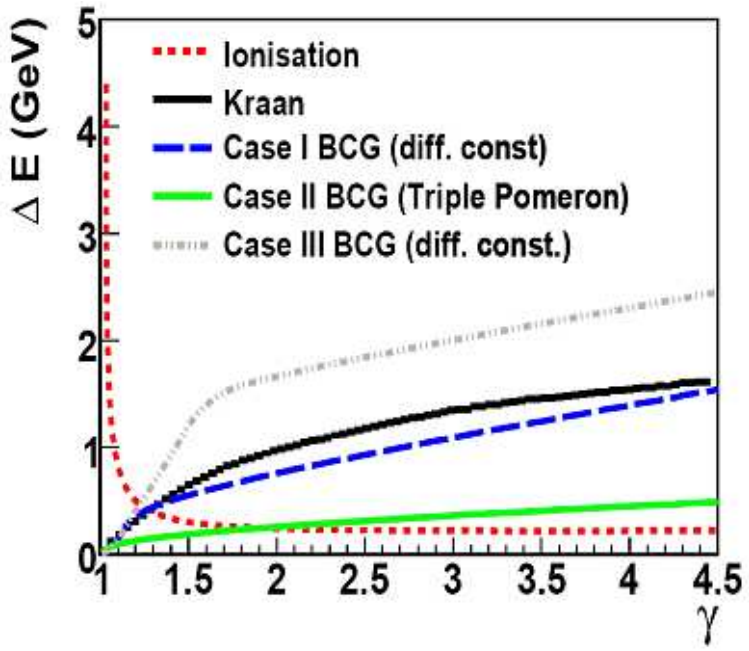

Figure 1.5: Predictions from four phenomenological models (a constant geometrical cross section used by Kraan, and three different cases for the functional form of cross section proposed by Baur, Cheung and Gunion (BCG)) of expected hadronic energy loss per interaction as a function of the Lorentz factor γ. Also shown is the ionization energy loss corresponding to the passage of an R-hadron with charge $\pm e$ through 18 cm of iron. See text for reference.

Lepton-like HSCPs don't have hadronic interactions and thus are not necessarily associated with jets. This makes the detection of new lepton-like HSCPs much easier, although their direct cross section would be suppressed compared to colored HSCPs [12].

Table 1.1: HSCP models used in this dissertation and their expected cross sections.

Theoretical Model	Expected Cross Section (pb)
mGMSB stau (156 GeV)	1.19
mGMSB stau (247 GeV)	0.097
MUED KK tau (300 GeV)	0.020
Split SUSY gluino (200 GeV)	2.2×10^3
Split SUSY gluino (300 GeV)	100
Split SUSY gluino (600 GeV)	5.00
Split SUSY gluino (900 GeV)	0.46
Split SUSY gluino (1200 GeV)	61×10^{-3}
Split SUSY gluino (1500 GeV)	10×10^{-3}
Split SUSY stop (130 GeV)	1.11×10^3
MSSM stop (200 GeV)	177
MSSM stop (300 GeV)	27.4
MSSM stop (500 GeV)	1.27
MSSM stop (800 GeV)	0.078

In this dissertation, we'll use four benchmark models to study the HSCP discovery potential at CMS for both hadron-like and lepton-like cases. Table 1.1 lists the expected crosssections and masses of the HSCP we will use in this dissertation.

1.6 Previous Experimental Searches

The most stringent mass limit on lepton-like HSCP is from the L3 detector at LEP2, giving 95% CL lower mass limits up to 100 GeV [24], by mainly using ionization energy loss per path length for a track, i.e., dE/dx (8% average resolution) information for particle identification and assumes HSCPs are pair produced (back to back in the L3 detector). Three candidate events (with masses less than 90 GeV) were recorded with 4.1 $\pm$ 1.8 estimated

background events from 450 pb^{-1} of e^+e^- annihilation data taken during 1999 at $\sqrt{s}$ = 192-202 GeV and 2000 at $\sqrt{s}$ = 200-208 GeV, with an overall $\sim$ 30% efficiency.

CDF [25] also performed searches for both strongly and weakly produced HSCPs with 90 pb^{-1} of $p\bar{p}$ Run I data and gave cross section limits of about $\sim$ 1 pb for hadron-like HSCPs with masses up to 250 GeV. CDF mainly used dE/dx (13% average resolution). Three different trigger data sets were used in the search: a muon trigger, a missing transverse energy $\not\!\!E_T > 35$ GeV trigger and an electron trigger. The muon trigger gave the most accurate result for lepton-like HSCPs. It selects events with hits in the muon chambers which match a track with $p_T > 12$ GeV/c in the central tracking chamber. Only triggers in the region $|\eta| < 0.6$ were used. They also required $\beta\gamma < 0.85$ for background rejection at lower momentum. To be considered in the weak production (lepton like HSCP) search, tracks must additionally pass an isolation cut requiring less than 4 GeV of calorimeter energy or total track p_T within a cone of $\sqrt{|\delta\eta|^2 + |\delta\phi|^2} < 0.4$ around the track. The main backgrounds for CDF arise from tracks for which the dE/dx measurement fluctuated high or included extra ionization from an unreconstructed overlapping particle.

Fig. 1.6 shows both the L3 lepton-like HSCP and CDF hadron-like HSCP results. CDF doesn't get a better limit for lepton-like HSCP due to their low luminosity and less clean environment (low efficiency $\sim$ 3%) in $p\bar{p}$ collisions. For hadronic HSCP results, CDF uses three different models to predict the lower cross section limits. The q=1/3 and q=2/3 lines in Fig. 1.6 are cross section limits for a fourth generation quark with charge 1/3 or 2/3. The

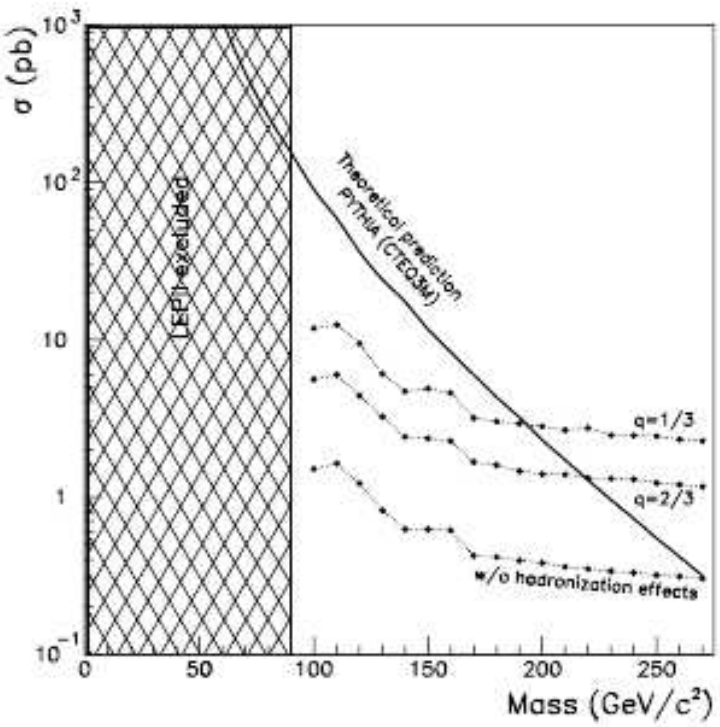

Figure 1.6: L3 lepton-like HSCP mass result with 100 GeV upper limit and CDF hadron-like HSCP cross section limits vs mass, set at a 95% confidence level, compared with the theoretical prediction for long-lived fourth generation quarks(Note this Fig. takes 90 GeV as LEP excluded limit, which is wrong). q=1/3 and q=2/3 lines are cross section upper limits for a fourth generation quark with charge 1/3 or 2/3. The line labeled "w/o hadronization effects" is for the squark that doesn't undergo the hadronic interaction after it's produced, i.e. it doesn't exchange its charge in the detector. The solid line shows the Pythia prediction from the generic fourth generation fermions model in Pythia. See text for reference.

line labeled "w/o hadronization effects" is for a fourth generation quark that doesn't undergo the hadronic interaction after it's produced, i.e. it doesn't exchange its charge in the detector. The squarks used are from the generic fourth generation fermions model in Pythia. The pair-produced lepton-like HSCP limit result CDF obtains is from 1.3 pb at 80 GeV to 0.75 pb at 120 GeV, while the expected cross section is over an order of magnitude lower than this sensitivity. Therefore, it's not included in Fig. 1.6.

Chapter 2

Collider and Detector

As we learned from Chapter 1, the main production modes for HSCPs are through pair production. To produce HSCPs, the center of mass energy of the $q\bar{q}/gg$ system has to reach the threshold of twice the HSCP mass. As theories expect HSCP masses to range from 100 GeV to 1.5 TeV, we need to have at least 3 TeV energy available for the $q\bar{q}/gg$ system, so that we can search for the full possible mass range of HSCPs.

The Large Hadron Collider (LHC) will collide two counter-rotating proton beams with 7 TeV each, giving a total collision energy $\sqrt{s}$ of 14 TeV. Thus, the LHC is capable of producing a pair of HSCPs for the mass range we're interested in, even considering the fact that partons (q, g) inside the proton carry only fractions of the proton momentum.

2.1 Large Hadron Collider

The Large Hadron Collider(LHC) at CERN, Geneva, Switzerland, sits about 100 m underground near the French-Swiss border. It is scheduled to start taking data in the autumn of 2008.

The main motivation for constructing the LHC is to elucidate the nature of electroweak symmetry breaking for which the Higgs mechanism is presumed to be responsible. Alternatives to the Standard Model (supersymmetry, extra dimensions) are also expected to show up at the TeV scale. New models are expected to explain the nature of dark matter, dark energy, and could possibly pave the way toward a unified theory under extra dimension theory, which requires modification of gravity at the TeV scale. The LHC will also aim at B-physics and CP violation. Previous experiments have already observed a small CP violation effect, but it's not enough to account for the apparent matter-antimatter imbalance in the Universe. The LHC will also provide high-energy heavy-ion beams at energies over 30 times higher than at previous accelerators, allowing us to further extend the study of QCD matter under extreme conditions of temperature, density, and parton momentum fraction (low-x). Hence, there are many compelling reasons to investigate the TeV energy scale with the LHC.

To achieve this unprecedented 14 TeV energy, the LHC is taking advantage of the existing CERN accelerator complex. As shown in Fig. 2.1, protons are obtained by removing electrons from hydrogen atoms and injecting them from the linear accelerator (LINAC2) into the Proton Synchrotron (PS) Booster, then the PS, followed by the Super Proton Synchrotron (SPS),

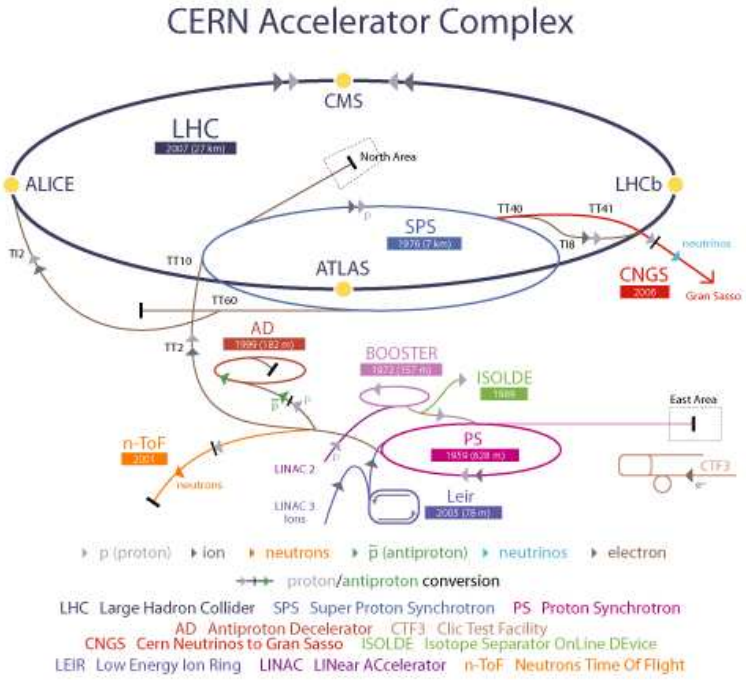

Figure 2.1: CERN Accelerator Complex and the LHC.

which brings protons from an energy of 26 GeV up to an energy of 450 GeV before entering the LHC ring. Protons will circulate in the LHC for 20 minutes to reach the designed 7 TeV energy. The average energy gain per turn needed in the LHC is only 0.485 MV.

The designed luminosity of the LHC is $10^{34} cm^{-2} s^{-1}$ with 2835 bunches, each containing 10^{11} protons, with a bunching crossing time of only 25 ns. The total proton-proton cross-section at $\sqrt{s} = 14$ TeV is expected to be roughly 100 mb[7]. Thus, at the designed LHC luminosity of $10^{34} cm^{-2} s^{-1}$, a detector expects to have an event rate of approximately 10^9 events/s. This challenges the on-line event selection process (trigger) to reduce the interaction rate to about 100 events/s for storage and subsequent analysis. During each bunch crossing (25ns), 25 inelastic interactions produce about 2500 particles/event (a very high radiation environment). The products of an interaction under study may be confused with those from other interactions in the same bunch crossing. The effect of this pile-up requires a detector to have very high granularity to keep occupancy low and resolve nearby tracks. To make the momentum measurement, a high B field and/or a large sized detector is needed to gain enough bending power. Also, the LHC bunch spacing time (25ns) requires a fast detector response to resolve the bunch crossing. If the ability to tag b-jets and identify B-hadrons is needed, a detector has to have good impact parameter resolution.

Four detectors are being installed in the caverns around the LHC collision points. Two of them are multipurpose experiments, ATLAS and CMS, the other two are dedicated experiments, one is for heavy ion physics, ALICE, and the other is for B-physics and precision measurements of CP violation,

LHCb. CMS is installed close to the French village of Cessy, between Lake Geneva and the Jura mountains.

2.1.1 Large Hadron Collider Commissioning

The LHC will be commissioned in four sequential stages, as shown in Fig. 2.2.

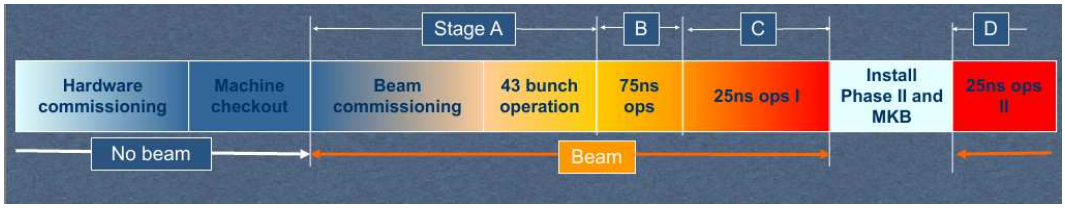

Figure 2.2: LHC Commission Stages, where MKB stands for Diluter Dump Kicker, an accelerator machine tuning technique.

Stage A includes the beam commissioning and the first/pilot physics run. The number of bunches will be gradually increased from 43 x 43 to 156 x 156, luminosity will be increased from $1.1 \times 10^{30} cm^{-2} s^{-1}$ to $1 \times 10^{32} cm^{-2} s^{-1}$. There's no need for a crossing angle due to the initial large bunch spacing time. The pilot physics run starts once $1 \times 10^{32} cm^{-2} s^{-1}$ luminosity is achieved and will last for about 40 days of beam time. Stage B will achieve a 75 ns bunch crossing time, and push the luminosity to $1 \times 10^{33} cm^{-2} s^{-1}$. Stage C is the nominal 25ns operation phase I, with a designed crossing angle of 300 $\mu rad$and designed luminosity at $2 \times 10^{33} cm^{-2} s^{-1}$. After Stage C, a period of shutdown time is allocated for machine tuning. In Stage D, the LHC will push towards its ultimate design performance with a luminosity of $1 \times 10^{34} cm^{-2} s^{-1}$ and 2835 x 2835 bunches.

A recent schedule predicts the LHC will be cooled down by June 1st,

2008, and the first proton beam will be injected in mid-June. Thirty days of beam time is needed to make the first collision at 7 TeV. After another 30 days of collision running, the pilot physics run begins and lasts for about 40 days of beam time (about 3×10^6 s). Assuming an above average beam efficiency (50%) for the LHC (the typical efficiency is 40%), we expect first physics collisions to begin in Nov. and continue until the end of 2008.

So we expect to accumulate about 300 pb^{-1} of data in 2008 with a luminosity of $1 \times 10^{32} cm^{-2} s^{-1}$ in the pilot physics running. This pilot run may already produce some interesting physics results. Remember, the expected cross sections for HSCPs in Table 1.1 are of the order of pb.

2.2 The Compact Muon Solenoid Detector

The Compact Muon Solenoid (CMS) experiment [26] is a detector which can endure the harsh environment of the LHC and provide accurate measurements at the same time. As shown in Fig. 2.3, the heart of CMS is a 13 m long, 5.9 m in diameter superconducting magnet with a 4 Tesla magnetic field. The tracking system, the electromagnetic calorimeter and the hadronic calorimeter are all installed inside the superconducting solenoid. The muon system is located outside the magnet, integrated with 4 muon stations to ensure full geometric coverage. Each muon station consists of several layers of aluminum drift tubes (DTs) in the barrel region and cathode strip chambers (CSCs) in the endcap region, complemented by resistive plate chambers (RPCs). The tracking volume is given by a cylinder of length 5.8 m and diameter 2.6 m. In order to deal with high track multiplicities, CMS employs 10

layers of silicon microstrip detectors, which provide the required granularity and precision. In addition, 3 layers of silicon pixel detectors are placed close to the interaction region to improve the measurement of the impact parameter of charged-particle tracks, as well as the position of secondary vertices. The electromagnetic calorimeter (ECAL) uses lead tungstate (PbWO) scintillating crystals. The light is detected by silicon avalanche photo-diodes in the barrel region and vacuum photo-triodes in the endcap region. The ECAL is surrounded by a brass/scintillator sampling hadron calorimeter (HCAL). The scintillation light is converted by wavelength shifting fibers embedded in the scintillator tiles and channeled to photodetectors via clear fibers. This light is detected by novel photodetectors (hybrid photo-diodes) that can provide gain and operate in high axial magnetic fields.

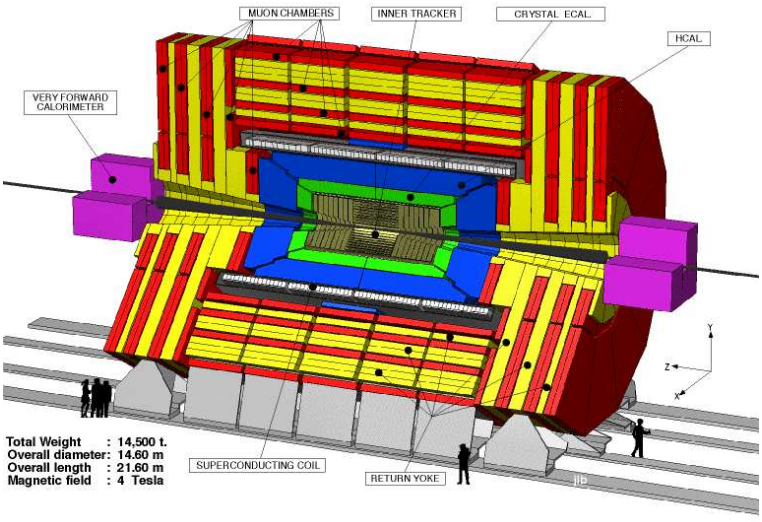

Figure 2.3: Annotated picture of the CMS detector.

2.2.1 Data Acquisition

Due to the very high total interaction rate compared to the relatively small rate of interesting interactions, it is indispensable to have a sophisticated data acquisition system able to extract the most interesting physics events from the huge number of collisions.

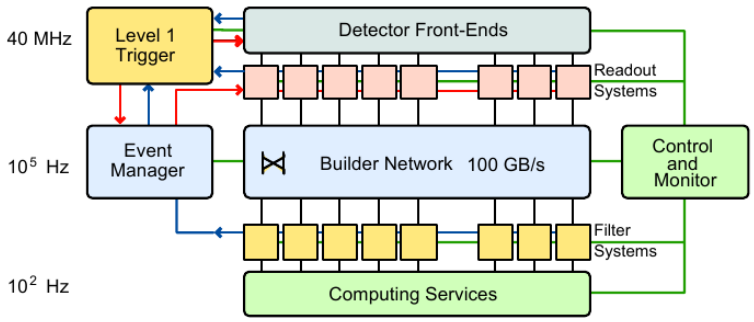

Figure 2.4: CMS DAQ system.

As shown in Fig. 2.4, the CMS Data Acquisition (DAQ) system reduces the event rate in two steps. Initially, various sub-detector front-end systems (FES) store data continuously in 40-MHz pipelined buffers. The first step of reducing the event rate, called Level 1 (L1), is a very fast hardware trigger, which uses coarse information from the calorimeters and the muon system to determine the basic event properties in order to decide if the event should be discarded. The Level-1 decision is based on the presence of "trigger primitive" objects such as photons, electrons, muons, and jets above set E_T or p_T thresholds. It also employs global sums of E_T and E_T^{miss}. Upon arrival of a synchronous L1 trigger via the Timing, Trigger and Control (TTC) system, the corresponding data are extracted from the front-end buffers and pushed

into the DAQ system by the Front-End Drivers (FEDs). The data from the FEDs are read into the Front-end Read-out Links (FRLs) that are able to merge data from two FEDs. The sub-detector read-out and FRL electronics are located in the Underground Service Cavern (USC). The event builder assembles the event fragments belonging to the same L1 from all FEDs into a complete event and transmits it to one Filter Unit (FU) in the Event Filter for further processing. The event builder has the ability to be deployed in up to 8 DAQ slices, each of which is a nearly autonomous system, capable of handling a 12.5 kHz event rate. So a maximum event rate of 100 kHz is then forwarded to the High Level Trigger (HLT), the second step to reduce the event rate.

The HLT is a software trigger and is based on about 1000 processors grouped in a so-called farm. The data from the detector front-end electronics are passed to the processor farm using a high bandwidth switching network. The data flow through the switch is about one Terabit per second. The functionality of the CMS HLT is three-fold: first to perform the readout of the front-end electronics after a Level 1 trigger accept, second to execute physics selection algorithms on the events read-out, in order to accept the ones with the most interesting physics content, and finally to forward these events, as well as a small sample of rejected events, to the online services that monitor the performance of CMS. The accepted events are finally archived in mass storage, on tapes.

2.2.2 Pixel and Silicon Strip Tracker

Due to the importance of particle identification for HSCPs with the Silicon Tracker and Muon Drift Tube information, we will explain some more details for these two subdetectors.

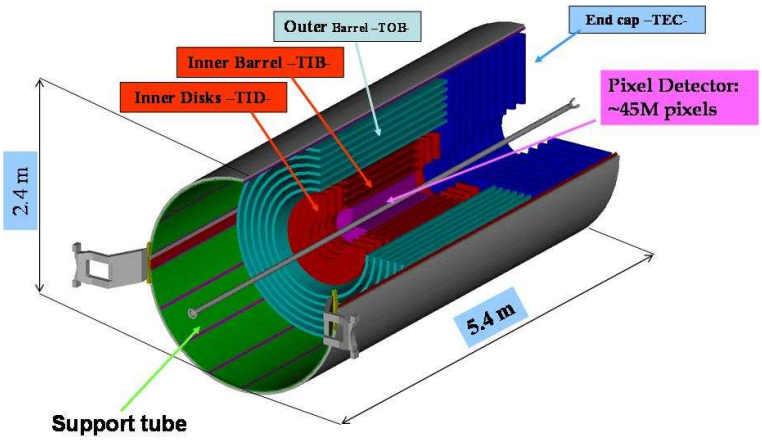

Figure 2.5: CMS tracker.

As shown in Fig. 2.5, the central tracker of CMS consists of a pixel tracker, which is located close to the interaction point and a Silicon Strip Tracker (SST) which is situated in the intermediate and outer regions.

The pixel detector has three cylindrical layers of pixel detector modules at 4, 7 and 11 cm in the r direction, which provides 3 high resolution hits in the $|\eta|$ <2.4 region. Two disks of pixel modules are located at 36 and 46 cm in each z direction, resulting in 2 hits in the 2.4< $|\eta|$ <2.8 region. There're in total 48 M pixels in the barrel part, and 18 M pixels in the endcaps. Fig. 2.6 shows a pixel sensor which is divided in cells of 100μm $\times$ 150μm with a thickness 250 μm. The signal from a single track is shared among several cells (charge-sharing), so it's possible to take the center of charges as the

crossing position when the particle passes pixel sensors. This way, the pixel hit resolution obtained is $\sigma_{r\phi} \sim 10\mu$m and $\sigma_{rz} \sim 20\mu$m. The pixel detector plays a vital role in precisely measuring the impact parameters, which allows reconstruction of a primary or secondary vertex in an event and consequently b-tagging.

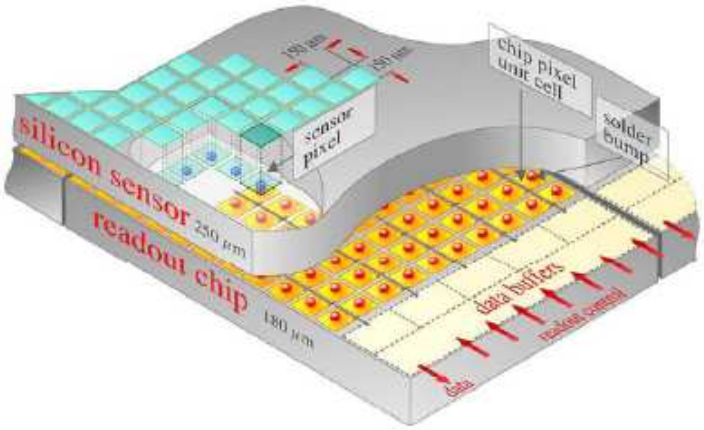

Figure 2.6: Pixel detector

The SST is composed of four subsystems. The central region up to a pseudo-rapidity of $|\eta|$ <1 is covered by the Tracker Inner Barrel (TIB) and the Tracker Outer Barrel (TOB). At each side of the TIB, the remaining volume inside the TOB is filled by the Tracker Inner Disks (TID). The silicon strip system is completed by two Tracker End Caps (TEC), extending the acceptance of the tracker up to a pseudo-rapidity of $|\eta|$ <2.5. The basic building block for the SST is a silicon strip module, as shown in Fig. 2.7. Each module contains one or two silicon sensors, a Kapton circuit layer is used to insulate the silicon from the module frame and to provide bias voltage supply

and temperature probe read-out. In addition, the module frame carries the front-end hybrid (multi-chip front-end read-out electronics module mounted onto a silicon module) and the pitch adapter.

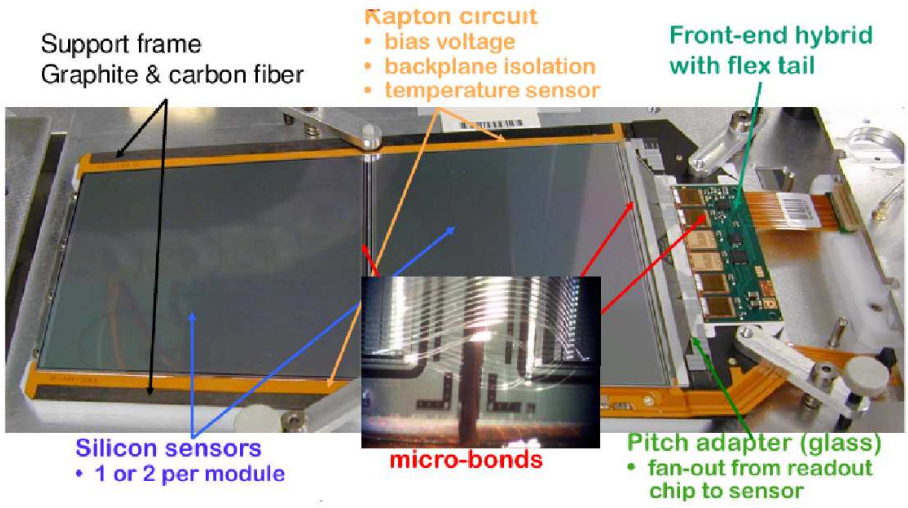

Figure 2.7: Silicon Strip Module

The TIB is composed of four layers, which use 320 μm thick silicon micro-strip sensors. The strip pitch is 80 μm on layers 1 and 2 and 120 μm on layers 3 and 4. The TID consists of three disks on each side, also employing 320 μm thick silicon micro-strip sensors. Its mean pitch varies between 100 μm and 141 μm. The TOB surrounds the TIB/TID and consists of six layers of 500 μm thick sensors with strip pitches of 183 μm on the first four layers and 122 μm on layers 5 and 6. The TEC is composed of nine disks on each side, carrying up to seven rings of silicon micro-strip detectors. The sensor width is 320 μm on the inner four rings and 500 μm on the outer three rings, the mean pitch varies from 97 μm to 184 μm.

The SST is equipped with both single-sided and double sided modules. Single-sided modules have their strips parallel to the beam axis in the barrel region and radial axis in the disks region. The double-sided (stereo) modules are a pair of single-sided modules, mounted back-to-back with a stereo angle of 100 mrad, resulting in a measurement of z in the barrel region and r on the disks. Double-sided modules are equipped in the first two layers and rings of TIB, TID, and TOB as well as rings 1, 2 and 5 in the TECs. The SST is composed of 15,148 silicon modules in total and the total number of silicon sensors in the strip tracker is 24,244.

The readout is done by the Front End Hybrid, which has four or six APV25 readout chips (analogue pipeline memory chips made by IBM). The APV uses radiation hard 0.25 m CMOS technology and can multiplex 128 channels into one analog output. Two APV outputs then combine into one data line by a MUX (Multiplexer). The PLL (Phase-locked loop) chip is used to decode clock and trigger signals, and the DCU (Detector Control Unit) is a 12-bit ADC for eight channels, which monitors hybrid and sensor temperatures, silicon sensor leakage current, and the hybrid low voltages. The analog signal from the APV is then fed into the FED (Front End Driver) via a 100 m long optical fiber. The FED can perform pedestal and common mode subtraction, cluster finding, and optional zero suppression. It stores the raw data until requested by the high level DAQ.

The impact parameter resolution in the plane perpendicular to the beams (r direction), is better than 35 μm over the full $|\eta| \leq 2.5$ range for particles with p_T about 10 GeV, as shown in Fig. 2.8 [27]. The longitudinal impact parameter (z) resolution is significantly better than 75 μm over most of the

rapidity range. These estimates do not take into account any degradation due to detector misalignment. Tails due to errors in track reconstruction are at a level well below the rate of displaced vertices due to long-lived particles.

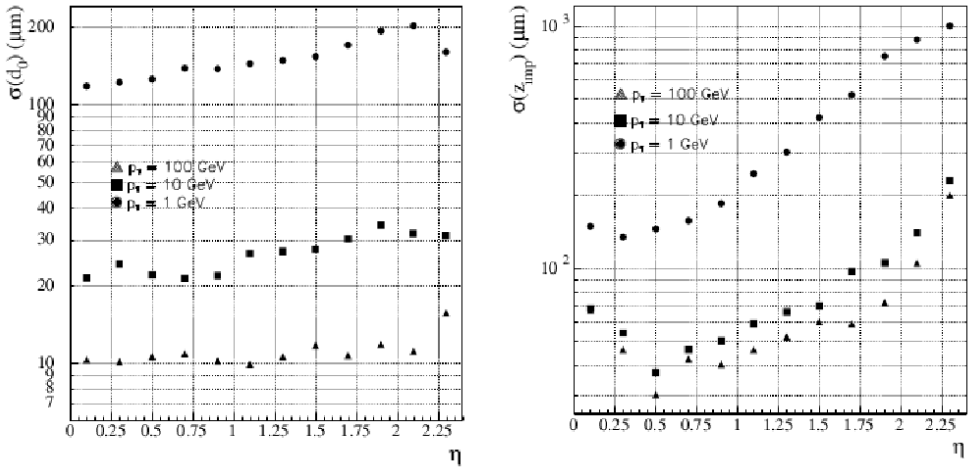

Figure 2.8: Transverse (Left) and Longitudinal (Right) impact parameter resolutions as a function of η, for muons of p_T = 1, 10 and 100 GeV.

2.2.3 Muon System

The muon system is used to identify muons, as shown in Fig. 2.9. The muon detector is composed of Cathode Strip Chambers (CSC) and Resistive Plate Chambers (RPC) in the end cap region and Drift Tubes (DT) in the barrel region. Together with the SST information, a global momentum resolution can be achieved on an order of several percent [27], shown in Fig. 2.10.

The importance of the muon system for our HSCP analysis is that it provides HSCP identification by a time-of-flight (TOF) measurement from DT.

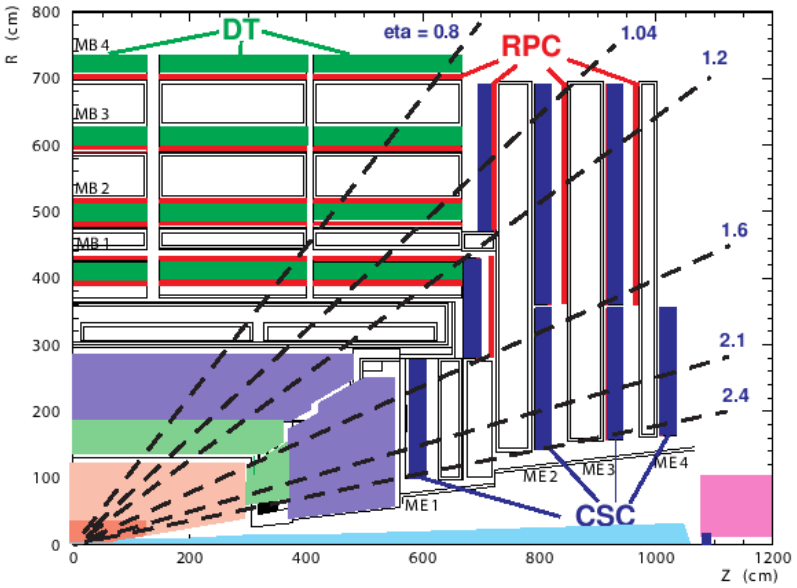

Figure 2.9: A slice of the Muon system of the CMS detector.

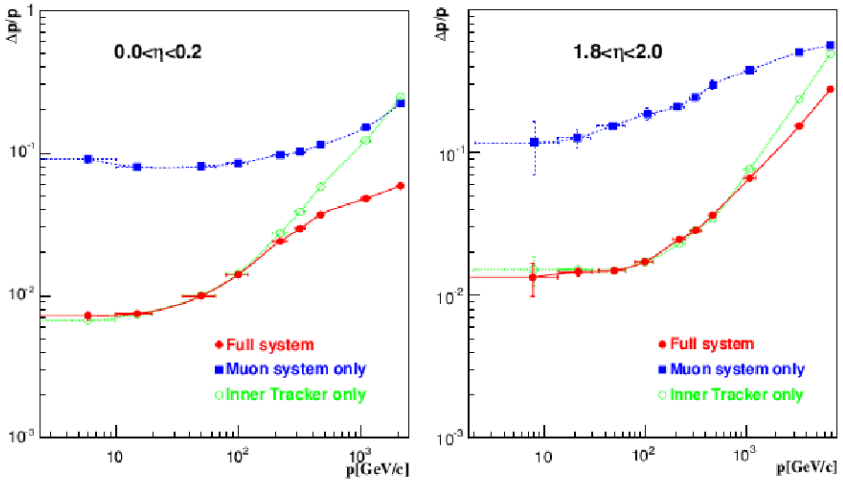

Figure 2.10: Momentum resolution versus p using the muon system only, tracker only or both (full system). Left: Barrel, $|\eta| < 0.2$; Right: Endcap, $1.8 < |\eta| < 2.0$.

Drift Tubes Chambers

The DT is the CMS barrel muon detector, made of four stations forming concentric cylinders around the beam line: three of them consist of 60 drift chambers each, the fourth, of 70. In the longitudinal direction, the detector is segmented in five wheels, whereas in the azimuthal angle the segmentation is in twelve sectors. Fig. 2.11 shows one of five wheels for the muon barrel system.

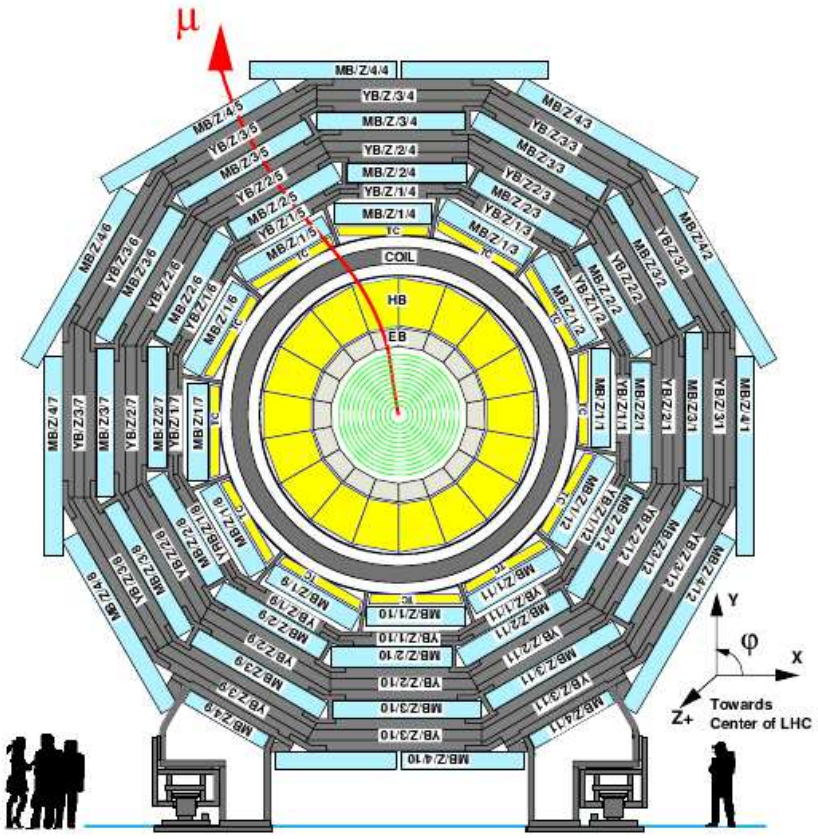

Figure 2.11: : Layout of the CMS barrel muon DT chambers in one wheel. In each of the 12 sectors of the yoke there are 4 muon chambers per wheel, labeled MB1, MB2, MB3, and MB4.

A drift-tube (DT) chamber, as in Fig. 2.12, is made of three (or two) superlayers (SL), each made of four layers of rectangular drift cells staggered by half a cell. The SL is the smallest independent unit of the design. The basic element of a drift chamber is the cell, a tube 42 mm wide and 13 mm high containing a sensitive anode wire. Cathode and electrode strips shape the electric field within the cell. The total number of anode wires is about 195,000. The time of drift is 380 ns in a gas mixture 15%Ar + 85%CO. Drift tubes are arranged in layers; four layers, staggered by half a tube, are grouped in a superlayer. A drift chamber is made up of two superlayers having anodes parallel to the beam line and possibly a third superlayer with anodes orthogonal to these two.

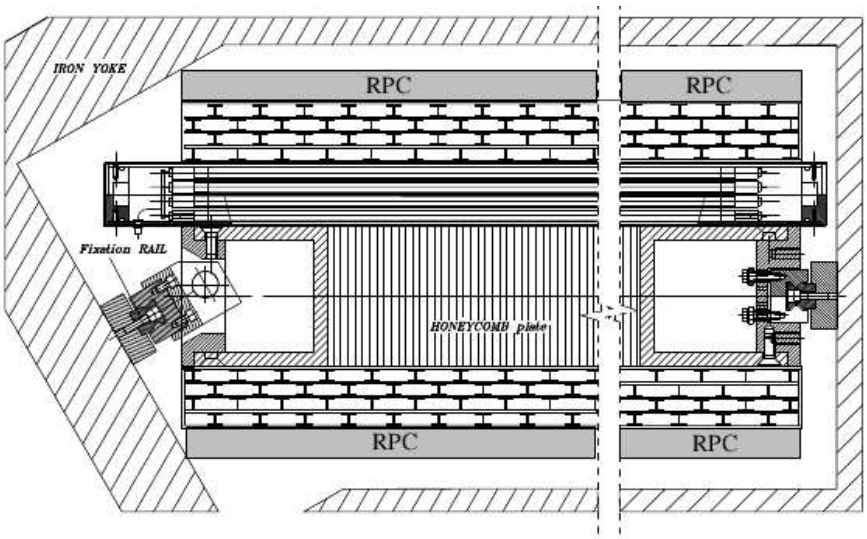

Figure 2.12: A DT chamber (about 2 m wide and 40 cm thick, as seen from Fig. 2.9) view in r-ϕ plane, one can see the 2 SLs with wires along the beam direction and the other perpendicular to it. In between is a honeycomb plate with supports attached to the iron yoke.

The SL gives excellent time-tagging capability, with a time resolution

of a few nanoseconds. This capability provides local, stand-alone, and efficient bunch-crossing identification. The time tagging is delayed by a constant amount of time equal to the maximum possible drift-time, which is determined by the size of the tube, the electrical field, and the gas mixture. Bunch-crossing tagging is performed independently in each of the 3 SLs by fast pattern-recognition circuitry. Together with the bunch-crossing assignment, this circuit delivers the position of the center of gravity of the track segment and its angle in the SL reference system with precisions of 1.5 mm and 20 mrad, respectively.

2.2.4 CMS Detector Control System

The control systems of all LHC experiments are realized in a complete hierarchical way. Independently functioning sub-parts can be included or excluded in the given hierarchy. An excerpt of the final tracker hierarchy, including the final number of items is shown in Fig. 2.13. The main TOP node is the CMS node followed by the sub-detectors Muon, HCAL, ECAL and the Tracker. The Tracker itself is again subdivided into Inner Barrel, Outer Barrel and two Endcaps, the next children are the 132 Cooling Loops and TEC sectors, which father the 356 Control Groups and the lowest units are the 1944 Power Groups representing a single power supply. Major sub detector routines are running on a supervisor PC, while Cooling Loop programs and their corresponding children are distributed on four PCs to the share load. The TSS system and TCS-DAQ communication reside on separate PCs.

The whole concept rests solely on precisely defined transitions from Finite

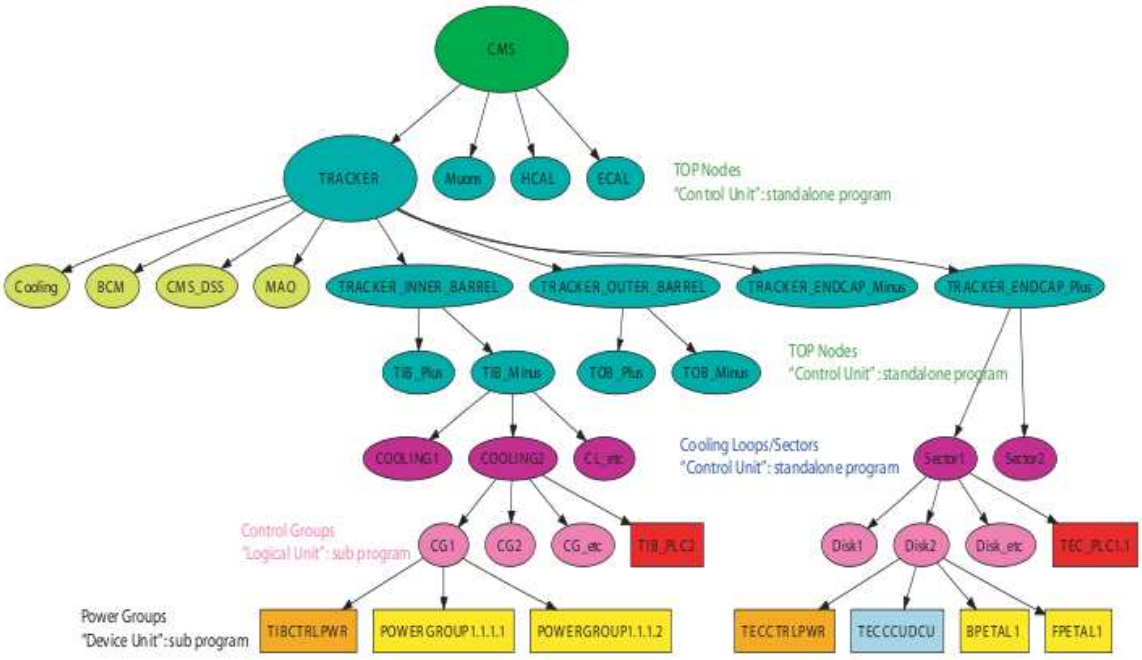

Figure 2.13: The CMS hierarchy with a simple excerpt of the Tracker hierarchy is shown. The main node CMS is followed by the CMS sub detectors, here for the Tracker. The TOP nodes TECplus, TECminus, TIB, TOB state are used to enable the corresponding detector. The further distinction in plus and minus represents connectivity schemes. The 132 nodes "cooling Loops" and "sectors" are the lowest level standalone programs, so called "control units" in the hierarchy. The 356 "Control Groups" are sub routines, named "logical units". The "device units" represent the power supply channels.

State to Finite State, true for all different elements of the hierarchy and running in a well concerted way. The Finite State Machine (FSM) is encoded in the SMI++ [28] language, in which a previous version was developed for DELPHI at LEP. The hierarchical approach facilitates summary information, especially error reporting of sub nodes, controlling large parts of the detector in groups. Also the inclusion and exclusion of detector parts are manageable in a defined FSM way.

Majority voting has to be established for a large dynamic DCS system, in order to avoid bringing top nodes into error or preventing them being on. Take SST DCS as an example. If only a single power supply is not responding, it's unreasonable to change the Tracker node status to OFF. We have to vote on majorities. The SST DCS chooses 95% of ON power supplies to have the Tracker in the ON state. If more than 5% of the power supplies are in failure, then we turn the Tracker into the ERROR state.

The basic software building block is the professional SCADA (Supervisory Control And Data Acquisition) software PVSS (Prozess- visualisierungs- und Steuerungssystem by ETM, a commercial Italian company) [29]. It has been greatly extended by CERN in a Joint Control and Operation Project (JCOP) framework [30] to adjust it for the projects' needs and to gain from overall developments. The software also extends functionalities like archiving of values, treatment of alarms, warnings and error messages.

The Tracker Detector Control and Safety System

The Tracker Control System (TCS) handles all interdependencies of control: low and high voltages, as well as fast ramp downs in case of higher than

allowed temperatures or currents in the detector, experimental cavern problems, etc. All this is ensured by evaluating 10^4 power supply parameters, 10^3 pieces of information from the Tracker Safety System and 10^5 pieces of information from the DCUs and Communication and Control Unit (CCUs), transmitted from the DAQ. The enormous dimension and complexity of the tracker needs special requirements of a control system to ensure safety and controllability [31].

The main task of the TCS is to switch on and off the whole tracker or parts of it, using the CAEN power supply system [32], a commercial power supply produced by an Italian company. Silicon strip modules of SST are conveniently grouped into 1944 "detector power groups" in order to share power, cooling and control services. Grouping criteria are governed by the mechanics and by the density of channels (a higher powering granularity is adopted close to the interaction point). The smallest power group consists of three modules (one mother cable) while the largest comprises up to 12 modules (four mother cables). Each power group is powered by a CAEN power supply unit (PSU). Each PSU provides one 1.25V (LV1) and one 2.5V (LV2) Low Voltage regulator (powering Front End Chips and controlling electronics), and two 0-600V (HV1 and HV2) High Voltage regulators to bias the silicon detector (TIB and TID have a bias voltage of 290V, and 250V for TEC, TOB HV is set at 300V [33]). The two low-voltage channels share the same return line and use the sensing wire technique to compensate, up to 4 V, the voltage drop along the cables. The two high-voltage regulators are fanned out at the PSU exit into eight lines; each silicon strip sensor is connected to one of these lines. There are also two temperature sensors for

each PSU which are located at the two hottest spots of the PSU.

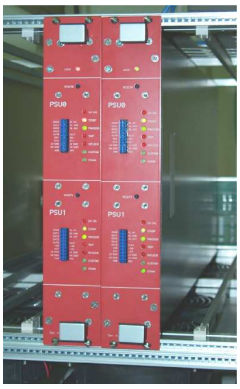

Figure 2.14: Two CAEN Power Supply Modules (PSM, CAEN A4601H model) in a crate.

In the CAEN system, a pair of PSUs is lodged inside one mechanical drawer to form one Power Supply Module (PSM, CAEN A4601H model), as shown in Fig. 2.14. All PSM need to pass the burn-in test before final installation to the power supply system [34]. Nine PSMs are hosted in one crate, and up to six crates are located inside one rack. One Array Controller (CAEN A1676 branch controller) controls all the PSMs inside one rack, through 6 CANBUS links, one per crate. Up to 16 racks can be supervised by one CAEN SY1527 power control module (CAEN Main Frame). The digital control of the detector modules is based on Communication and Control Unit (CCU) chips. Each CCU takes control of more than one module. Several CCUs are daisy-chained to form a so-called CCU-ring (or control rings, see Sec. 4.3.2 in Ref. [26]). All of the SST control services are grouped to form 352 control rings, each of them powered by one 2.5V power source from the CAEN system. To begin controlling/biasing the SST modules, the corresponding control rings have to be powered up first.

The control of the detector by the DCS is achieved using a finite state machine (FSM). In exactly defined states, depending on the hardware status, specific commands to the devices permit adequate transitions between the states. These commands are mainly switching commands for the voltage channels. For the essential communication between the DCS and the power supplies, the OLE for Process Control (OPC) standard is used, which is a set of standard interfaces based upon Microsoft's OLE/COM technology [35]. The tracker controls system will be embedded in the DCS of the whole CMS detector and will have to make sure that general CMS states are implemented while containing more tracker specific ones.

In the example of switching from OFF to ON by an ON command of the CMS DCS to be ready for taking physics data, different steps have to be done which cause state changes. The system first has to check environmental conditions and the state of the cooling plant before enabling the power supply of the control rings for the DAQ. When the DAQ informs the DCS that this part is working, the DCS can read out more environmental sensors of the control rings to have a higher granularity of information for completing the analysis of the conditions. After this, the low voltage channels can be activated to power the electronics of the detector modules which leads to a state change to the state ON LV. If again the DAQ reports that everything is alright, the DCS switches on the high voltage channels which provide the biasing voltage for the silicon sensors. During the ramp up of the voltage, the tracker is in the state HVRAMPINGUP. After reaching the final value the state changes to ON, and PVSS informs the DAQ system of a tracker "ready" state. The CMS DAQ system will decide when to begin physics data

taking, together with the other subsystems' status.

The entire SST will be kept at a temperature of -10^{o}C, in order to minimize the degradation of the sensor performance due to irradiation, the increase of the sensor dark current, and reverse annealing effects. This will also help maintain the full depletion voltage at a reasonable level, namely below 600 V after ten years of operation at nominal LHC luminosity [36]. A low humidity inside the SST also has to be ensured to prevent condensation.

All of this environmental information (sensor temperature and humidity) is closely monitored by the Tracker Safety System (TSS). The TSS is a self-contained system operating on the information provided by about one-thousand hardwired humidity/temperature probes. A Programmable Logical Controller (PLC) based system handles the process of monitoring those probes and its action depends on the monitored values. The TSS will interlock the tracker power (fast HV ramp down) in case of higher than allowed temperatures or currents in the detector, experimental cavern problems, or when the TCS fails to respond, etc.

Fig. 2.15 illustrates the overall idea of how the DAQ, DCS, and DSS systems communicate between each other.

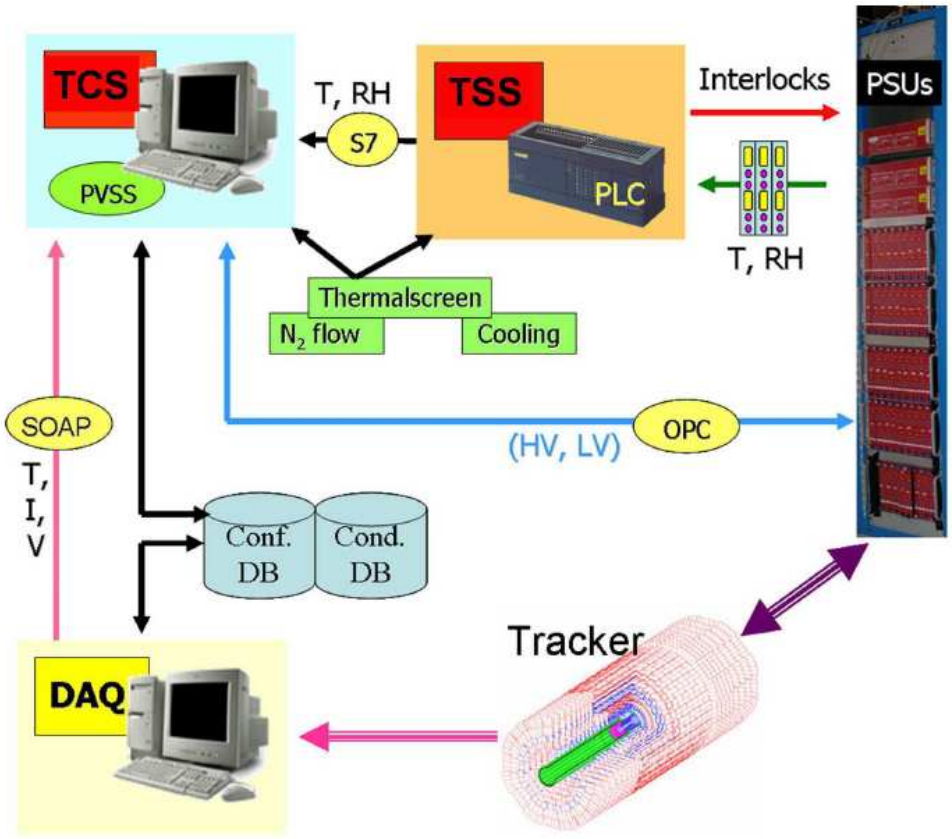

Figure 2.15: Data flow between tracker Detector, DCS, DSS and DAQ systems.

Chapter 3

Event Simulation and Reconstruction

3.1 Data Flow at CMS

Event information from each step in the simulation/DAQ and reconstruction chain is logically grouped into a so-called data tier at CMS. The data flow for Monte-Carlo (MC) is GEN (generater level Monte Carlo event), SIM (simulated energy depositions of MC particles in detector parts, resulting in simulated hits) and DIGI (simulated hits converted into detector response, basically the same as the RAW data output from the detector).

In the case of physics data, it's DAQ-RAW (detector data from front end electronics + L1 trigger result) and RAW (detector data after online formatting, including the L1 and HLT trigger result and potentially some of the higher level quantities calculated during HLT processing).

Both MC and data undergo the same RECO process. Reconstructed

objects include: tracks, vertices, jets, electrons, muons, etc. and possible small quantities of very localized hit information. To keep the event size smaller, only quantities useful for the final physics analysis are saved from the RECO tier to the so-called Analysis Object Data (AOD) tier.

Thousands of scientists around the world will want to access and analyze the LHC data, but the data volume is too huge to be fully handled by CERN only. So CERN is building a distributed computing and data storage infrastructure: the LHC Computing Grid (LCG). The data from the LHC experiments will be distributed around the globe, with a primary backup recorded on tape at CERN. CERN is named Tier-0 (T0) for LCG as it holds the primary data. After being processed by the L1+HL trigger algorithms and reconstructed, the CMS data are split in Primary Data Sets (PDS) defined through a logical OR of several HLT paths, each path being seeded by a unique L1 path. The combination of HLT paths defining a primary data set is chosen taking into account the similarities in terms of physics requirements, trying to avoid the overlap among the data sets as much as possible. The PDS, nominally shipped to Tier-1s (T1) in both RECO and AOD format, are the starting point for the skimming. Each CMS physics group is required to develop a set of skimming algorithms and define the skims they need to produce the available and accessible large secondary data sets. Tier-1s may also redo the reconstruction with better calibrations and run those defined skim jobs by physics groups, which further decreases the data volume. The skimmed data, nominally in AOD format, will be distributed to a series of large computer centers (Tier-2 (T2) centers) with sufficient storage capacity for a large fraction of the skim data, and with round-the-clock support for

the Grid. These Tier-2s will monitor/validate incoming skim data and make the data available to other facilities (Tier-3), each consisting of one or several collaborating computing centers for specific analysis tasks. Individual scientists will access these Tier-3 computers through resources such as local clusters in a university department or even individual PCs.

Before the physics data taking begins around Nov. 2008, CMS wants to make sure all the data tiers in the LCG work properly as expected. So in the CSA07 (Computing Software and Analysis 2007 challenge) effort, CMS practiced its data distribution ability with more than 150M MC events of various SM processes, roughly representing the first 1 fb^{-1} of integrated luminosity data. CSA07 divided all the data into 6+1 PDS's based on the HLT information (electron, muon, JetMET, BJet, tau, gamma and AllEvents). Each PDS was RECO'ed at the T0 and skimmed at T1's. Skimmed samples were transferred to T2's.

For this HSCP analysis, the signal MC was not generated at the Tier-0, as a CSA07 official procedure, due to the non-availability of the needed MC generators at the time when CSA07 started. Instead, the HSCP signals were generated and reconstructed locally by the University of Louvain and here at the University of Kansas. The background samples used in this analysis are from the standard CSA07 background, "Standard Model Soups", formed by combining samples as follows:

- Chowder: the data set obtained by combining all CSA07-Alpgen (a generator for hard multi-parton processes in hadronic collisions [37]) samples: $t\bar{t}$ Jets (up to 4 Jets) Z/γ^* + Jets (up to 5 Jets) W+Jets (up

to 5 Jets)

- Stew: the data set obtained by combining all CSA07-Pythia [38] samples generated with filters for b$\bar{b}$, charmonium, electron, and muon.

- Gumbo: the data set obtained by combining all CSA07-Pythia samples generated without filters, including "Hard" QCD di-jets (each jet has $p_T > 15$ GeV), MinBias and Gamma+Jets.

In the following section, we will discuss in detail how the HSCP signal MC events are generated and simulated.

3.2 Monte-carlo Simulation

3.2.1 Event Generation

KK Tau in MUED

The dominant mode for KK lepton production is by direct pair production. For the LHC it's $pp \to \tau_R^1, \bar{\tau}_R^1$ with a cross section of about 20 fb for the 300 GeV KK τ, where the τ_R^1 and $\bar{\tau}_R^1$ are right-handed KK τ, and right-handed anti-KK τ, respectively. In principle, the right-handed KK τ can also be produced from the cascade decay of KK Z bosons or level-2 KK τs. But the cross section for these processes is relatively small, ~ 5 fb, as calculated in Appendix A.2. So in this study, we only simulate the direct pair production of the right-handed KK τ.

We first generated the right-handed KK τ for the process $pp \to \tau_R^1, \bar{\tau}_R^1$ in CompHEP4.4p3 [39] with the MUED model [40] and output those events

in a text file format. Cpythia1.2.7 [41] was used to change the text file format to the Pythia Event (PEV) format known by the CompHEPInterface in CMSSW. Then we feed the result to the CompHEPInterface in CMSSW_1_4_6. As the CompHEPInterface doesn't recognize KK particles, we have to use a local version of the CompHEPInterface and change the particle code for the KK τ to the particle code used by CompHEP. After all the bugs were fixed, the hadronization was performed by Pythia [38] inside CMSSW and a ROOT [42] file in Event Data Model (EDM) [43] format (CMS GEN format) was generated.

As this analysis aims at 10 $pb^{-1} \rightarrow 1fb^{-1}$ of integrated luminosity, the expected number of KK τ events is small, so we only generated 1000 events for the study.

Stau in mGMSB

Production of the stau can proceed directly via a virtual photon or Z or via the cascade decays of heavier supersymmetric particles (mainly squarks and gluino pairs). In the latter case, which is in general dominant over direct production, one or more stau will appear in the final state as final products of the decay chain of the sparticles. The particle mass spectrum and the decay table have been produced with the program ISASUGRA [44] version 7.69. The model selected is the minimal GMSB (mGMSB) and two benchmark points on the Snowmass Points and Slopes (SPS) line 7 [45] were chosen. SPS are a set of 9 typical benchmark points for SUSY breaking mechanism, and SPS 7 is for the GMSB scenario with stau as NLSP. The corresponding parameter values are the following:

- stau(156) : $N = 3$, $\Lambda = 50000$ GeV, $M = 100000$ GeV, $\tan\beta = 10$, $sign(\mu) = 1$, $c_{grav} = 10000$

- stau(247) : $N = 3$, $\Lambda = 80000$ GeV, $M = 160000$ GeV, $\tan\beta = 10$, $sign(\mu) = 1$, $c_{grav} = 10000$

These parameter values result in a mass for the stau of 155.8 and 247 GeV respectively. The squarks and gluinos masses in these two points are about 1.1 TeV, and 1.7 TeV, respectively. In both cases their production cross section is between one and two orders of magnitude higher than the direct stau pair production. Event generation is performed with Pythia version 6.409 by enabling all sparticle production subprocesses.

Fig. 3.1 shows distributions of the β, η, p_T E_t^{miss}, E_T^{sum} and transverse energy of the two hardest jets in the event for the three lepton-like HSCP cases. The jet algorithm is the midpoint cone algorithm with radius of 0.5 implemented in the CMS offline software, CMSSW [27]. All quantities are computed from the list of particles produced by PYTHIA after hadronization. Neutrinos, muons and HSCPs are not used in either the jet clustering algorithm or in the vectorial and scalar energy sums. Therefore, they contribute to the E_t^{miss} (transverse part of vectorial missing energy) variable, but not to the E_T^{sum} (sum of transverse energy magnitude for jets) variable or to the jets. The large E_t^{miss} values are due to the products of the squarks and gluino decay chains and are clearly an additional feature that can be exploited at the event selection stage.

Despite the fact that KK tau and GMSB stau are both lepton like HSCPs, the kinematic properties are quite different for the two cases. The η distri-

bution is more "central" for stau, while E_t^{miss} is almost zero for the KK τ scenario and very high for the mGMSB stau.

stop in MSSM

Stop production in hadron collisions proceeds mainly via the coupling of the stop to the gluon. Stop were generated using the Madgraph [46] generator. The parton shower and matrix element matching technique implemented in this generator allows the generation of extra jets in the event to be simulated in a more faithful way than what can be normally done with Pythia. A generic MSSM spectrum was adopted for generation because only the stop mass affects the production cross section.

Gluino in Split SUSY

The main gluino production mechanism at the LHC is $g + g \rightarrow \tilde{g} + \tilde{g}$ with a cross section of about 2 nb for a 200 GeV $\tilde{g}$. For this mass value the contribution from $q + \bar{q} \rightarrow \tilde{g} + \tilde{g}$ is about 0.1 nb.

Events were generated with Pythia for six mass points, varying from 200 GeV to 1.5 TeV, using a general MSSM implementation with the user-defined process only. These events included contributions from both the gg and $q\bar{q}$ annihilation processes.

Figs. 3.2 and 3.3 show the generator-level distributions for the stop and gluino R-hadron HSCP cases. The two samples display similar kinematic properties, except for the E_T^{sum} and jet spectra, which are significantly harder in the gluino samples. This feature can be explained by the larger amount of final state radiation that characterizes the gluino production. R-hadrons

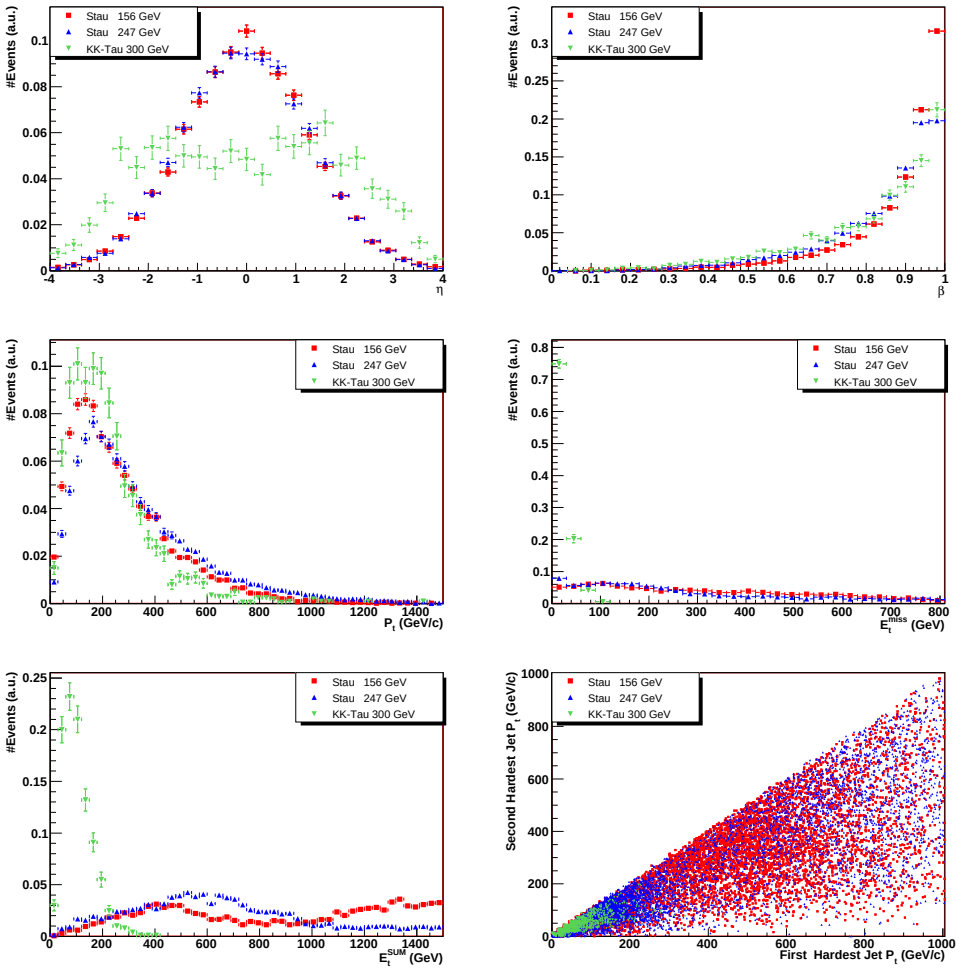

Figure 3.1: From left to right, top to bottom, the plots are distributions of the η, β, p_T, E_t^{miss}, E_T^{sum} and the plot of second hardest p_T vs the first hardest jets p_T in lepton-like HSCPs (stau/KK tau) events.

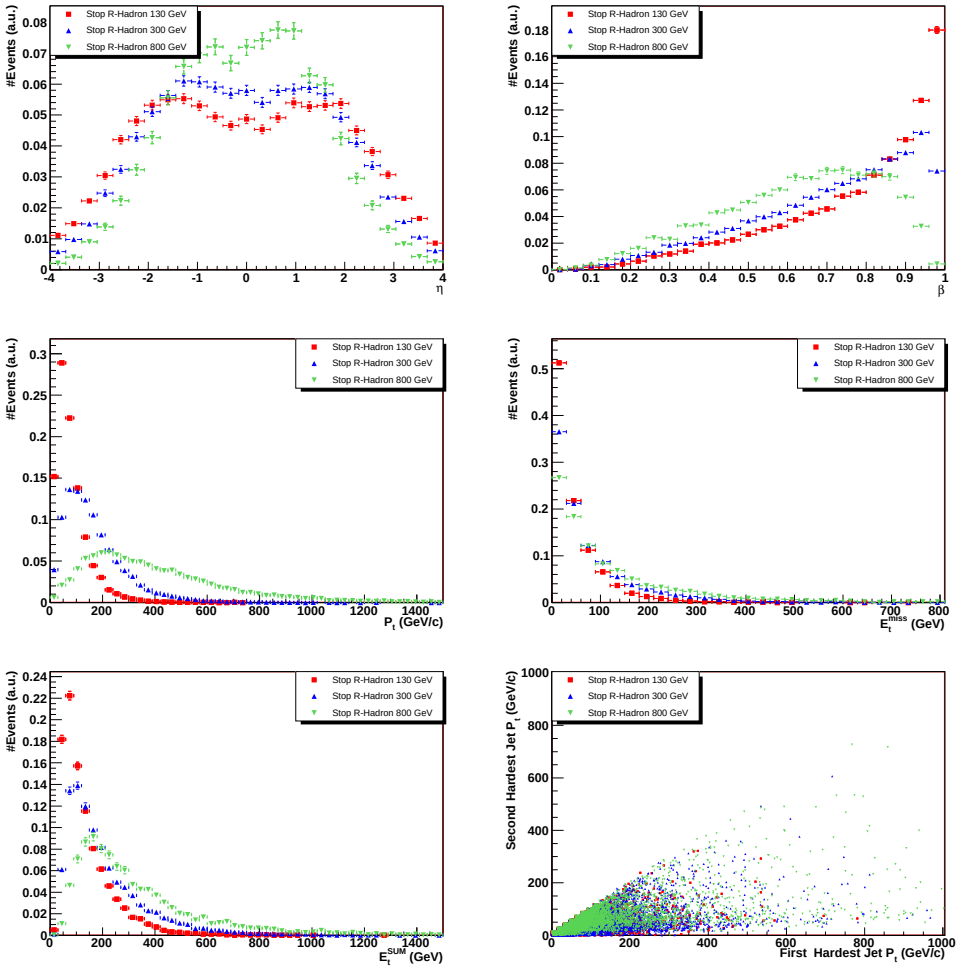

Figure 3.2: From left to right, top to bottom, the plots are distributions of the η, β, p_T, E_t^{miss}, E_T^{sum} and the plot of second hardest p_T vs the first hardest jets p_T in stop R-hadron events.

Table 3.1: Signal MC samples, cross sections, number of generated events and corresponding integrated luminosity are shown in the first four columns. The last two columns contain the percentage of events for each sample having at least an HSCP in $|\eta| < 2.4$ and $|\eta| < 0.9$ regions, respectively.

Model and Mass (GeV)	Cross section (pb)	Number of events	Integrated luminosity (fb^{-1})	HSCP in $\|\eta\| < 2.4$ (%)	HSCP in $\|\eta\| < 0.9$ (%)
stau (156)	1.19	6899	5.78	97.6	72.6
stau (247)	0.097	6899	71.1	97.5	70.9
KK tau (300)	0.020	1000	50	84.7	40.9
gluino (200)	2.2×10^3	10000	4.55×10^{-3}	89.7	47.4
gluino (300)	100	6000	6.00×10^{-2}	91.7	50.0
gluino (600)	5.00	10000	2.00	93.7	55.5
gluino (900)	0.46	1000	2.17	92.6	57.7
gluino (1200)	61×10^{-3}	1000	16.4	91.4	53.9
gluino (1500)	10×10^{-3}	1000	100	90.4	55.8
stop (130)	1.11×10^3	10642	9.59×10^{-3}	87.8	43.1
stop (200)	1.77×10^2	9957	5.63×10^{-2}	90.9	47.3
stop (300)	27.4	10346	0.378	92.8	50.4
stop (500)	1.27	5872	4.62	95.3	54.7
stop (800)	7.81×10^{-2}	5081	65.1	96.9	61.9

(gluino and stop scenarios) foresee higher masses, so they have lower velocity compared to lepton-like HSCPs.

In Table 3.1, we summarize all the MC samples we generated, their cross-sections and corresponding integrated luminosities. We also list the acceptance for the HSCP in the barrel ($|\eta| < 0.9$) and endcap regions ($|\eta| < 2.4$) for the muon system. This information is useful as the muon system participates in the trigger decision for CMS and the muon trigger is a natural candidate for lepton-like HSCPs.

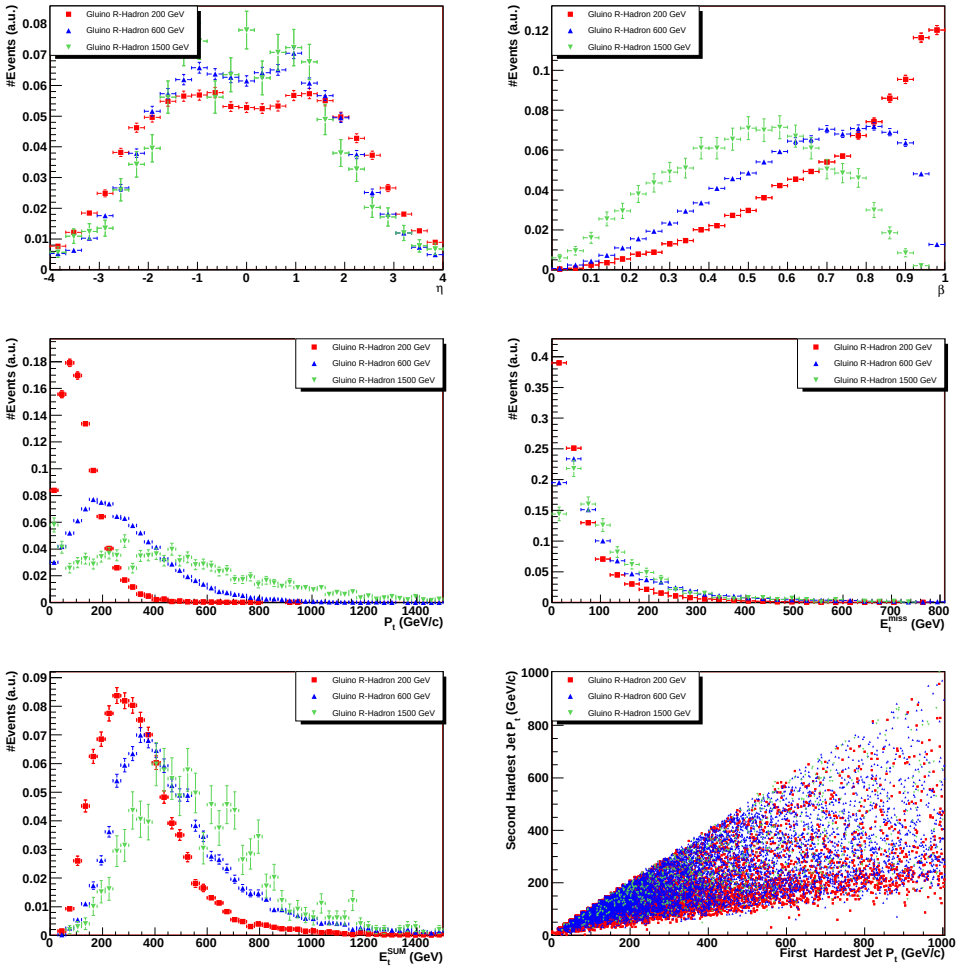

Figure 3.3: From left to right, top to bottom, the plots are distributions of the η, β, p_T, E_t^{miss}, E_T^{sum} and the plot of second hardest p_T vs the first hardest jets p_T in gluino R-hadron events.

3.2.2 Detector Simulation and Digitization

The Detector simulation is done using Geant4 [47] under the CMSSW (CMS Software) framework [27]. Geant4 simulates the electromagnetic and hadronic interactions for particles passing through a detector, resulting in simulated energy losses in different sensitive detector parts. The sensitive part could be a silicon module in the tracker or a piece of crystal in the calorimeter, depending on the sub-detector system. The simulated energy loss and the position of the sensitive detector part form a detector hit for the sensitive part.

After the Geant4 simulation, the simulation of the electronic readout by the detector and DAQ systems for the hit, i.e.,Digitization, is performed inside CMSSW, resulting in the same readout format as that from real physics RAW data acquired by the CMS DAQ system.

Taking the silicon strip tracker digitization as an example, the simulated energy loss of a charged particle crossing a single-sided layer SST is distributed along a path between the entry and exit points within the detector module. Landau fluctuations are taken into account. The simulated drift of the charges to the detector surface also takes into account the Lorentz drift and diffusion in the perpendicular plane. These are done by Geant. On the detector surface, the resulting charges corresponding to each strip are integrated, and Gaussian-distributed noise is added. The conversion to digital counts is applied using the gain of the detector and the time with respect to the signal bunch crossing.

Special Simulation for HSCP

One problem for the HSCP analysis here is that the standard Geant4 is not designed to handle the propagation in matter of exotic particles like HSCPs. While the interaction with matter of lepton-like HSCPs can be easily described in terms of the standard electromagnetic interactions, specific models are required for the description of the nuclear interactions of R-hadrons [48].

A dedicated package, called *CustomPhysics* [49], was developed to allow the CMS implementation of Geant4 to propagate the HSCP in the detector. The package allows new particles and new processes to be introduced into Geant4. For stau or KK τ particles, one just needs to register the particles (by providing their physical properties like mass, spin, etc.) and the existing Geant4 processes like ionization and multiple scattering that the particles are supposed to undergo. For stop or gluino R-hadrons an add-on for Geant4, implementing their hadronic interactions, has been developed and documented in [49]. As explained in Ref. [49] the hadronic interaction model implemented in this software assumes that the heavy parton (gluino or stop) acts only as a spectator, only behaving as a reservoir of kinetic energy. The kinetic energy available to each hadronic interaction is proportional to the mass fraction (co-moving hypothesis). Since the heavy parton mass is $m_{\tilde{g},\tilde{t}} >> m_{quarks}$ the available energy in the hadronic interaction is very low:

$$E_{kin} = (\gamma - 1)m_{quarks},$$

where m_{quarks} ranges between 0.3 and 0.9 GeV. With γ of order 1 the result is an available energy, and so a maximum energy loss, of a few GeV. For this

reason the hadronic HSCPs are typically not stopped, even after hadronic interaction in the calorimeters, and can reach the muon system. A schematic drawing for a R-hadron passing through the CMS detector is given in Fig. 3.4. More details on the penetration depth of different type of R-hadrons are given in Ref. [49].

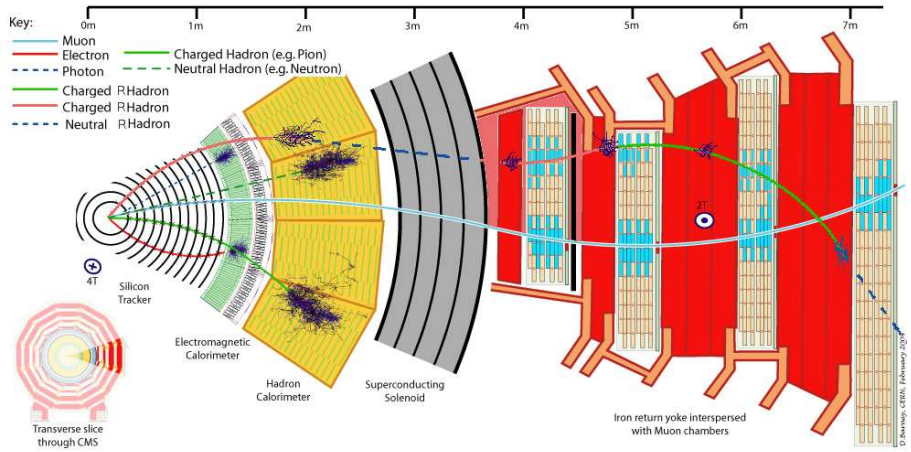

Figure 3.4: The passage of SM particles and R-hadrons through the CMS detector. Lepton-like HSCPs behave like heavy (slow) SM muons, while R-hadrons may convert to another kind of R-hadrons (charged or neutral) due to interactions inside the detector.

This Geant4 add-on module has been included in the CustomPhysics package to integrate smoothly with the CMS software. The hadronic interaction software requires that a list of the possible hadronic processes is specified. The list has been produced both for stop and gluino hadrons assuming only charge conservation. The possible flavor content (s, c or b quarks) of the incoming R-hadron is always neglected and only hadrons with u, d quarks are produced as final states. Nevertheless, the kinematics are properly taken into account and the higher masses corresponding to heavier

flavors are considered in the process.

3.3 Event Reconstruction

Within CMS event data model, data is categorized to event data and condition data. The event data holds all data that was taken during a triggered physics event as well as all data derived from the taken data. The condition data are gathered during the construction and operational phases for the experiment and are needed to fully understand the physics data collected from the detector. Calibration and alignment are good examples of offline conditions data usage.

3.3.1 Event data Reconstruction

Event data reconstruction is performed mainly in three steps: local reconstruction, global reconstruction and combined reconstruction.

Local Reconstruction

Local reconstruction in individual detector modules leads to Rechits, which contain information about the energy deposition and positions of the particles interacting in the detectors. For example, in the Tracker detectors (strips and pixels), local reconstruction algorithms search for strips/pixels with a signal exceeding a threshold, and use these as seeds for clusters. Clusters are built by adding neighboring strips/pixels. In the Muon Drift Chambers (DTs), local reconstruction provides the position of a muon hit in a drift cell, determined from the drift time measurement and the effective drift velocity.

Three-dimensional track segments within a superlayer are built from hits in each component layer.

Global Reconstruction

The global reconstruction algorithms use the objects created in the local reconstruction, combine them with the objects arising from other modules of the same subdetector to produce further objects which represent the best measurement from that subdetector. At this stage, no attempt is made to link the information from different subdetectors.

For the global reconstruction in the Tracker system, CMS has mainly implemented and tested two tracking algorithms: Road Search (RS) and Combinatorial Track Finding (CTF) [50]. Both algorithms perform track reconstruction in three steps:

- seed finding, which provides a selection of initial hits and a first estimate of parameters,
- pattern recognition, which associates hits to a track, and
- track fitting, which determines the best estimate of the track parameters.

The first two items are specific to each of the algorithms while the track fit is always performed by a Kalman filter and smoother(An iterative procedure for track and vertex fitting) [51]. The tracks are extrapolated as a helix in a magnetic field. In the absence of a magnetic field the tracks are extrapolated as straight lines. Material effects (energy loss and multiple Coulomb scattering) are estimated each time a track crosses a detector layer.

CTF builds a seed out of either a hit pair in the inner layers and a loose beam spot constraint or out of a hit triplet in the inner layers. The starting parameters of the trajectory are calculated from a helix passing through the three points. The selected hits must be pointing towards the interaction point and a minimum p_T cut is applied. In the pattern recognition step, each trajectory determined in the seeding step is propagated to the next surface. Hits are looked for in a window whose width is related to the precision of the track parameters. If a hit is found inside this window it is added to the candidate trajectory and the track parameters are updated. If several compatible hits are found a new candidate is created for each of them. Candidates are sorted according to quality (based on the χ^2 and the number of hits) and the five best are retained for further propagation. As hits are added to the candidate trajectory the knowledge of the track parameters improves and the size of the search window decreases. Propagation of a candidate ends if configurable cuts on the number of layers or the number of consecutive layers without a hit are exceeded. To allow cosmic track reconstruction, the beam spot requirement in seeding is not applied, and the seeds are created in the outer layers of the tracker. The pattern recognition also allows propagation between the upper and lower hemispheres of the tracker and missing hits due to non-hermetic coverage of the tracker for cosmic tracks.

The road search algorithm treats the CMS tracker in terms of rings, where a ring contains all tracker modules at a given r-z position, spanning 360^o in ϕ. A track will be a line in r-z, and the algorithm uses predefined sets of rings consistent with a line in r-z in which it will search for a track. These

predefined sets of rings are referred to as roads. For seed finding, the road search algorithm uses pairs of hits in seed rings. A cut is imposed on the maximal difference in the azimuthal angles of the seed hits. The set of rings that composes the road will be those consistent with the linear extrapolation between the seed rings in the r-z plane. In the first part of the pattern recognition step, an expected trajectory is determined using the two seed hits and the beamspot. The trajectory is extrapolated through the other rings of the road, and hits are collected inside a narrow window around the expected trajectory. This collection should contain all the hits of a track, along with other hits that happen to overlap and lie close to the track. In the second part of pattern recognition, the collection of hits is turned into a trajectory. A trajectory is first built in low occupancy layers, extrapolating inside-out. With the trajectory well-defined from the low occupancy layers, hits from the higher occupancy layers are added to the trajectory. The final track will contain at most one hit per detector module, though potentially more than one hit per layer due to detector overlaps. The standard road search algorithm is slightly modified in order to reconstruct cosmic muons. The constraint on the extrapolation of the roads was loosened to include any pair of seed rings within the acceptance of the read-out detector. In addition, hits are sorted in the global y direction, rather than inside-out.

Global reconstruction in the muon system is often called "Standalone muon" since it does not make use of tracker hits; The reconstruction makes use of the track hits and track segments from the local reconstruction step in the individual muon subdetector modules of the CSC, DT, and RPC detectors. The algorithm starts from the locally-reconstructed muon track seg-

ments. A segment in one of the innermost detector stations (those closest to the interaction point) is used as a seed for a Kalman filter, which builds trajectories in the radially-increasing direction. A χ^2 cut is applied to reject hits unlikely to be associated with the track, which can arise from showering, δ rays, and pair production. The trajectory is propagated using a detailed map of the magnetic field and taking account of energy loss in the detector material (mainly the steel of the magnet return yoke), until the outermost detector layer of the muon system is reached. A backward Kalman filter is then applied, working from outside in, and the track parameters are defined at the innermost muon station. Finally, the track is extrapolated to the nominal interaction point and a vertex-constrained fit to the track parameters is performed. In this fit, since the magnetic field is inhomogeneous and nonuniform in the endcap regions, the two-dimensional hits in CSC layers are used instead of the track segments that were used for seeding.

Combined Reconstruction

Combined reconstruction, the final stage of reconstruction, combines input objects created in the global reconstruction within each subdetector, creating objects based on the complete CMS detector. For example, a standalone muon candidate can be extrapolated into the Tracker detector, adding associated silicon tracker hits and performing a final fit to the track, thus improving the measured muon track parameters using the high precision of the Tracker measurements, as shown in Fig. 2.10. Another common example is the matching of ECAL and HCAL clusters and their combination into jet candidates.

However, in this HSCP analysis, we will just perform a simple match in η-ϕ space, i.e. a cut on $\delta R = \sqrt{\delta\eta^2 + \delta\phi^2}$. We prefer this way because muon and tracker systems are two independent systems, and give two independent β measurements, thus mass measurements. This enables us to cross-check the two systems and get a reasonable systematic error. Also R-hadron momentum measured in muon system is not reliable due to the possible charge flipping effect, so one prefers to use the tracker momentum instead. More detailed discussion will be provided later in the event selection part of this dissertation.

3.3.2 Condition data Processing

Condition data includes information from both online and offline. The online system conditions data are used for analysis of detector errors, while offline conditions data are needed for event reconstruction as well as data quality monitoring. In most cases, the conditions needed offline are a subset of the online conditions. Calibration and alignment are good examples of offline conditions data usage. Here, one needs to characterize the detector running conditions for particular periods of time.

Calibration is based on detector signal measurements taken under controlled conditions. This set of data is characterized by several parameters per electronic channel, e.g. pedestal, gain, time offset, drift velocity, dead and hot channels, and others. Data are often collected for sets of channels within a given sub-detector (a silicon strip in the SST for example) and an algorithm is used to produce a calibration set. For example, one has a silicon

strip quality, good or bad, determined by the distributions of the cluster position, cluster size, noise, etc. Calibrations are considered valid for a certain interval of time called Interval Of Validity (IOV). The calibration information for any given IOV can have one or more versions of the calculation of the calibration values made with different algorithms. This version information might consist of both an algorithm name and version to allow for different algorithms, and slight changes, to a particular algorithm. The procedure varies considerably from detector to detector.

The alignment uncertainties of the CMS tracker and muon detectors affect the performance of track pattern recognition, reconstruction, and therefore the track momentum and position resolutions. A set of alignment corrections for an active detector element used in the reconstruction, such as a silicon sensor or a muon chamber, is defined to be a vector containing six terms: δx, δy, δz, $\delta\alpha$, $\delta\beta$, and $\delta\gamma$, where the first three represent the displacements of the three translation degrees of freedom while the last three define Euler angle corrections for the three possible rotations. All corrections are calculated with respect to the ideal geometry as delivered by the geometry service [27]. Therefore, the ideal geometry together with a set of alignment corrections defines a new reconstruction geometry.

The detector alignment is expected to progressively improve with integrated luminosity. Different scenarios are usually considered. Here are the two scenarios concerned with data taking:

The First Data Scenario corresponds to the very early stage of data taking. It should be reached before accumulating 100 pb^{-1}, and is sometimes called 10 pb^{-1} conditions. This scenario assumes that the detector has been

realigned by using the first 10 pb^{-1} of integrated luminosity, which will probably be the best available information for processing the first 100 pb^{-1} of data from the pilot physics run. It assumes 1 mm and 0.2 mrad of relative positioning precision between the Tracker and Muon System. Muon Chambers are located within the Muon System to 1 mm and 0.25 mrad precision. The Tracker structure and modules relative misalignment ranges from 3 to 13 μm for the Pixel Detector and from 50 to 300 μm for the Silicon Strip Tracker.

The long term scenario corresponds to the situation of optimal alignment performance. It is expected after collecting about 1 fb^{-1} data. In this scenario the Tracker to Muon System relative misalignment will be about 200 μm and 50 mrad, while the SST precision is improved by a factor of 10 with respect to the previous scenario.

The online condition data are stored in the Online Master Data Storage (OMDS) database. The offline conditions subset is cached at the experiment site in a database referred to as ORCON (Offline ReConstruction ONline subset). The condition data needed by the HLT farm will be accessed from ORCON. Data will then be transferred to ORCOF (Offline ReConstruction OFfline subset) which is the main conditions database for the CERN Tier 0 and Tier 1 computing centers. From ORCOF, data will be distributed to the other tiered computing centers. Calibrated data will be written back to ORCOF and transferred to ORCON if required by the HLT. The underlying database technology for all online and offline databases is Oracle [52]. The offline conditions subset is extracted from the online non-event data and sent to the offline database. This process is called Online-to-Offline transfer (O2O).

One specific example of utilizing offline conditions data is the tracker offline reconstruction/calibration using the High Voltage (HV) information from the DCS system. If the HV for a certain module is OFF for a period of time during data taking, i.e., the silicon strip is not properly biased, the corresponding channels should be treated as dead channels. Then the reconstruction/calibration software should not take hits from this module into account. To make the HV status information available in the ORCOF offline database, the high voltage status O2O has to be developed (see Appendix B for details).

3.4 HSCP Triggers and Skim

At trigger level, a lepton-like HSCP has a high probability of being reconstructed as a muon. Reconstruction can fail, however, if the HSCP is too slow. In this case it will reach the muon system out of time with respect to typical relativistic muons and, therefore would either be reconstructed in the wrong bunch crossing or fail to be reconstructed at all because of quality cuts imposed by the Level-1 Trigger or High Level Trigger algorithms. In the case of R-hadrons, reconstruction in the muon system is expected to be even more problematic due to the charge-flipping effect, which might happen in the iron yoke or calorimeters. Matching between the individual measurements in the muon stations could fail due to the change in the bending of the R-hadron track, or because of the absence of measurements in the stations where the R-hadron is electrically neutral. It can also happen that a R-hadron appears neutral in the tracker, but charged in the muon system.

In this case there can be no match between tracks measured in the muon system and in the inner tracker. Finally, the R-hadron energy deposition in the calorimeters may be sufficient for the HSCP to fail the isolation criteria in the muon reconstruction .

HSCPs can also give rise to a sizeable missing energy, unless back-to-back pair production cancels out individual contributions. The missing energy trigger neither suffers from the timing issues described above, nor does it depend on whether HSCPs are reconstructed successfully as muons because muons are not expected to be considered in the missing energy estimate at trigger level.

As has been shown in Sec. 3.2.1, the missing energy trigger, as well as other calorimeter-based triggers (like E_T^{sum} or jets), could become very efficient for HSCP events due to model-specific features like the underlying production mechanism or the nature of the heavy particle itself. A comprehensive trigger study was performed on all generated samples in order to evaluate the expected trigger efficiencies and their dependence on the thresholds. The goal of the study was also to identify the most suitable data streams on which to perform the offline event selection and analysis. All signal samples were processed using the CMSSW_1_6_7 version of the CMS software. After simulation of the detector response, the Level-1 trigger emulator software and the official HLT reconstruction and selection appropriate for CMS first data-taking were run.

3.4.1 L1 and HL Triggers for HSCP

Before presenting results of the L1 trigger study, we have to mention two L1 regional trigger bugs in both the RPC and CSC emulations during the CSA07 effort. The problem in the RPCs is the absence of any bunch crossing assignment to the individual RPC hits, which are, by default, all considered to be in the correct bunch crossing. Bunch crossing assignment has since been introduced in a later CMSSW version. The problem in the CSCs is that the bunch crossing assignment is incorrect. It has been discovered that the CSC simulation (before the trigger emulation) misaligned bunch crossings earlier than bunch 0, offsetting them by 1 bunch later than they should be.

The lack of bunch crossing assignment is negligible for fast particles ($\beta \sim 1$), but not for slow HSCPs. HLT and offline muon reconstruction are also affected, because all RPC hits, irrespective of their timing properties, are again considered in the reconstruction performed at that level. It is similar for the CSC hits because the only timing constraints applied are at the trigger level, so that if the trigger fails to reject an event due to an incorrect bunch crossing assignment it can still be reconstructed.

In order to avoid overestimating the trigger efficiency, a special procedure was developed. For every output muon from the Level-1 Trigger, a topological match with the Monte Carlo truth tracks corresponding to HSCPs in the muon system is attempted. If the match is successful, the time of flight stored in each DT or CSC simulated hit of the track is used to compute a difference (ΔT) with respect to the time of flight of a $\beta = 1$ particle traveling along a straight line from the nominal interaction point to the

position of the simulated hit. Then, the minimum ΔT among all simulated hits is compared to a free parameter ΔT_{max} to decide whether the muon should be accepted or not. The L1 Trigger bits for the Single and Double Muon paths (L1_SingleMu7 and L1_DoubleMu3 respectively) are then recomputed using only the L1 muons accepted in this way.

ΔT_{max} value was chosen as being half the bunch crossing spacing (25 ns). The reason for this is very easy to understand. As a muon has to travel for 12.5 ns before reaching the first layer of the muon system, a delay larger than 12.5 ns with respect to a muon just means the track will be assigned to the next bunch crossing as the DAQ acts once per 25 ns. And due to the L1 track quality cut, the slow HSCP may not be triggered.

The efficiency results for the Level-1 Trigger and HLT selection on all simulated data samples are presented in Table 3.2 and Table 3.3. The custom selection criterion described above for the L1 muon objects is used with $\Delta T_{max} = 12.5$ ns. The trigger menu released in CMSSW_1_6_7, which includes L1 and HLT trigger definitions and thresholds, was adopted. Only events with at least one HSCP in the $|\eta| < 2.4$ region were considered.

Table 3.2 summarizes the L1 efficiency results and includes the details of some of the most relevant triggers. These triggers were identified as those giving the highest absolute efficiency. The incremental efficiency reported in each column is relative to the triggers in the columns on the left. The last column in the table reports the total L1 efficiency as well as the incremental efficiency of all the L1 triggers not listed in the table relative to those present in the table. The numbers show that a very small fraction of signal events are selected by the L1 triggers not listed in the table. The total L1 efficiency

is very high for the mGMSB stau and for the gluino thanks to the production mechanism and accompanying radiation, as noted in the previous Sec. 3.2.1. In the case of R-hadrons, the calorimeter-based triggers become, as expected, more efficient at high masses. The muon trigger has the opposite behavior, which could be explained by the lower average speed of the heavier HSCPs.

Events accepted by the HLT are regrouped in so-called Primary DataSets (PDS). A PDS contains the events that pass any of a set of HLT paths. The same event may be found in more than one PDS. The offline analysis has been performed on the following PDS's:

- Muon PDS, using the set of relaxed cuts for single- and double-muons with $p_T > 37$ GeV and $p_T > 10$ GeV, respectively.
- JETMET PDS, the E_T thresholds are 180 and 80 GeV for one jet and one MET respectively.

Table 3.3 summarizes the HLT efficiency results and includes the details of the most relevant HLT paths. The first three paths in the table were identified by first finding the path that gives the highest absolute efficiency and then by ordering the other paths according to decreasing incremental efficiency. The non-isolated single muon, E_t^{miss}, and E_T^{sum} are, in almost all cases, the first in the ranking. The single jet trigger, reported in the fourth column, becomes the best alternative to the E_T^{sum} trigger if that is not commissioned at the start-up of the experiment. The incremental efficiency reported in each column of the table is relative to the triggers in the columns on the left. The last column in the table reports the total efficiency of the OR of the four HLT paths as well as the incremental efficiency of all other HLT paths. The

Table 3.2: L1 trigger efficiency (in %) for all simulated data samples. Only events with at least one HSCP in the $|\eta| < 2.4$ region were considered. The incremental efficiency reported in each column is relative to the triggers in the columns on the left. The last column in the table reports the total L1 efficiency as well as the incremental efficiency of all the L1 triggers not listed in the table relative to those present in the table. The notation SMu7 means single muon trigger with a 7 GeV p_T cut, DMu3 means double muon tigger with 3 GeV p_T cuts on both muons, ETM40 means a missing E_T greater than 40 GeV, HTT250 is the trigger in which the sum of jet E_T for all the jets is greater than 250 GeV, and SJet100 means single jet with more than 100 GeV.

L1 Trigger	SMu7		DMu3		ETM40		HTT250		SJet100		**L1_Total**	
Eff. (%)	Abs	Inc	Abs	Inc	Abs	Inc	Abs	Inc	Abs	Inc	Abs	Inc
stau 156	97.4	**97.4**	90.1	**0.7**	90.6	**1.4**	88.6	**0.0**	89.7	**0.0**	**99.6**	**0.1**
stau 247	97.3	**97.3**	88.8	**0.4**	87.8	**1.8**	84.4	**0.1**	87.0	**0.0**	**99.7**	**0.0**
KKtau 300	75.3	**75.3**	55.4	**2.0**	14.5	**4.7**	3.7	**0.1**	10.0	**0.1**	**84.9**	**2.6**
stop 130	35.6	**35.6**	11.9	**2.2**	31.5	**16.8**	11.4	**0.6**	20.8	**0.0**	**62.3**	**7.2**
stop 200	36.2	**36.2**	13.7	**1.4**	40.1	**22.9**	18.1	**0.6**	28.7	**0.4**	**69.8**	**8.2**
stop 300	36.0	**36.0**	13.1	**1.3**	46.6	**28.2**	26.9	**0.8**	36.8	**0.2**	**74.7**	**8.2**
stop 500	35.8	**35.8**	13.5	**1.5**	51.3	**30.8**	38.4	**1.4**	45.2	**0.6**	**81.6**	**11.6**
stop 800	33.1	**33.1**	11.4	**1.0**	57.3	**36.8**	52.4	**3.5**	55.9	**1.0**	**88.8**	**13.5**
gluino 200	45.9	**45.9**	22.1	**2.3**	43.5	**21.1**	36.6	**2.9**	33.1	**0.2**	**80.0**	**7.6**
gluino 300	44.5	**44.5**	21.2	**2.2**	50.4	**25.1**	49.1	**4.2**	41.3	**0.2**	**85.6**	**9.4**
gluino 600	39.5	**39.5**	17.7	**1.4**	64.0	**35.8**	75.7	**8.9**	63.2	**0.5**	**94.3**	**8.3**
gluino 900	34.7	**34.7**	14.6	**1.2**	70.0	**43.5**	88.4	**13.5**	80.9	**0.4**	**97.3**	**4.0**
gluino 1200	26.6	**26.6**	11.3	**1.1**	76.1	**53.1**	91.4	**13.1**	86.7	**1.2**	**98.0**	**3.0**
gluino 1500	23.9	**23.9**	9.3	**0.7**	76.8	**57.0**	93.8	**14.4**	92.1	**1.0**	**98.7**	**1.8**

numbers show that these four paths account for basically all of the possible efficiency that can be obtained with the HLT. It can be concluded that the final online efficiency is in principle over 70% for lepton-like HSCPs, and in the range 40% - 95% for the R-hadron samples.

3.4.2 Data Skimming

In the CMS analysis scheme, a significant data reduction, both in event size and number of events, is first found by dedicated offline "skim" jobs, which result in the production of the so-called Analysis Object Data (AOD) sets. The skim jobs reduce the size of the single events by dropping some of the event information contained in the PDS. For the purpose of this analysis a dedicated skim job implementing a simple loose event selection was developed and is described here. The detailed muon hit information and the energy depositions in the tracker are key elements of the HSCP analysis, which will be explained more later. These data are not included in the standard AODs. In order to retain this information and at the same time keep the event data size in the AOD within acceptable limits these data are added to the standard AOD and some jet collections uninteresting for this analysis are instead dropped. The charge depositions in the inner tracker detectors are also computed and stored in the AOD in a more compact format than the inner tracker raw data, from which this information can be extracted. Events in the JetMET PDS are selected if one or more of the following conditions are satisfied:

- 1 track with $p > 10$ GeV and $dE/dx > 5$ MeV/cm

Table 3.3: HLT efficiency for all simulated data samples, only events with at least an HSCP in $|\eta| < 2.4$ are considered. The incremental efficiency reported in each column is relative to the paths in the columns on the left. The last column in the table reports the total efficiency obtained with the four paths listed in the table as well as the incremental efficiency of all the HLT paths not listed in the table relative to those present in the table.

HLT Path	1MuonNonIso		1MET		1SumET		1Jet		**Listed**	**Others**
Eff. (%)	Abs	Inc	Abs	Inc	Abs	Inc	Abs	Inc	Abs	Inc
stau 156	96.8	**96.8**	84.1	**1.9**	91.3	**0.5**	74.9	**0.0**	**99.2**	**0.2**
stau 247	96.8	**96.8**	81.5	**2.1**	87.4	**0.6**	63.5	**0.0**	**99.5**	**0.1**
KK tau 300	75.2	**75.2**	7.8	**2.2**	7.9	**1.2**	2.1	**0.0**	**78.6**	**4.4**
stop 130	21.9	**21.9**	18.1	**12.5**	17.3	**3.2**	3.9	**0.0**	**37.6**	**2.1**
stop 200	23.7	**23.7**	26.0	**18.1**	25.1	**4.1**	7.0	**0.0**	**45.9**	**3.4**
stop 300	23.5	**23.5**	33.4	**24.4**	35.7	**5.8**	10.8	**0.0**	**53.7**	**4.0**
stop 500	23.4	**23.4**	39.3	**29.6**	48.3	**8.4**	17.3	**0.0**	**61.4**	**5.6**
stop 800	22.0	**22.0**	44.8	**34.5**	62.9	**14.0**	21.7	**0.0**	**70.5**	**6.6**
gluino 200	22.4	**22.4**	28.5	**21.3**	44.6	**13.6**	9.8	**0.0**	**57.3**	**1.8**
gluino 300	22.6	**22.6**	35.3	**26.7**	58.0	**17.8**	14.0	**0.0**	**67.0**	**2.1**
gluino 600	21.3	**21.3**	47.1	**36.1**	83.2	**27.9**	23.1	**0.0**	**85.4**	**1.3**
gluino 900	16.6	**16.6**	49.5	**40.0**	92.4	**36.3**	29.2	**0.0**	**92.9**	**1.0**
gluino 1200	11.7	**11.7**	55.6	**47.6**	95.0	**36.0**	34.0	**0.0**	**95.3**	**0.8**
gluino 1500	11.3	**11.3**	56.2	**49.1**	96.0	**35.7**	45.2	**0.0**	**96.1**	**0.2**

- 1 track with $p > 50$ GeV and $dE/dx > 3.5$ MeV/cm
- 1 track with $p > 200$ GeV
- 1 muon with $p_T > 20$ GeV
- 2 muons with $p_T > 10$ GeV

where the dE/dx is the track dE/dx estimated by a truncated mean estimator, to be defined later.

An event from the Muon PDS is selected in the skimming phase if a muon with $p_T > 45$ GeV is reconstructed.

Fig. 3.5, Fig. 3.6, and Fig. 3.7 show the η, β and p_T distributions after trigger and skimming selections for lepton-like, stop, and gluino HSCPs, respectively. The η edges around 2.4 are due to the SST geometric coverage limits.

In Table 3.4, the fraction of signal events found in each PDS, in either of the two PDS's, and the event overlap between the two PDS's are presented.

The number of events for the various background samples remaining after the skim selection are reported in Table 3.5.

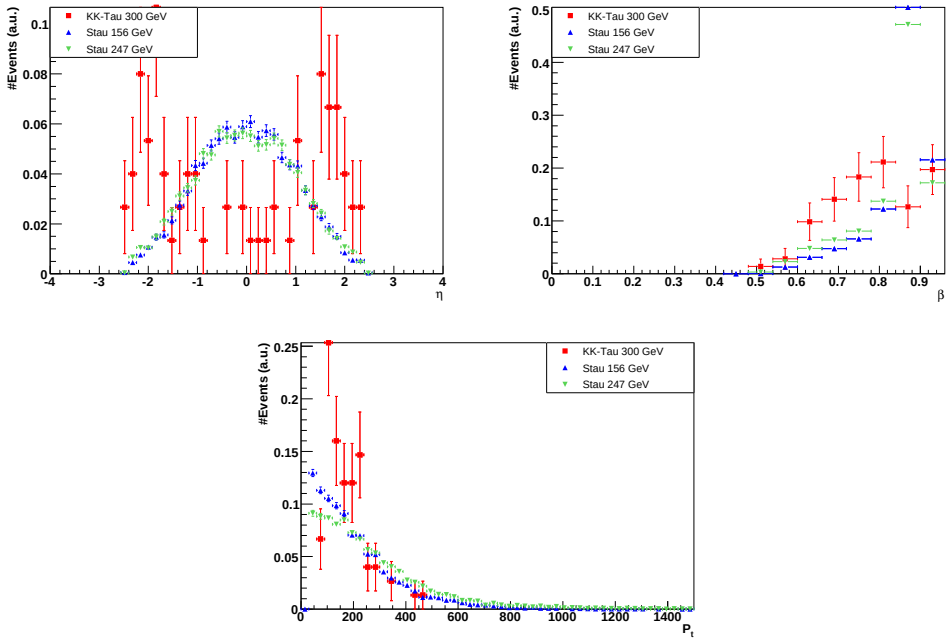

Figure 3.5: From left to right and up to down, the plots are distributions of the η, β, and p_T in lepton-like HSCPs (stau/KK tau) events, after data skimming.

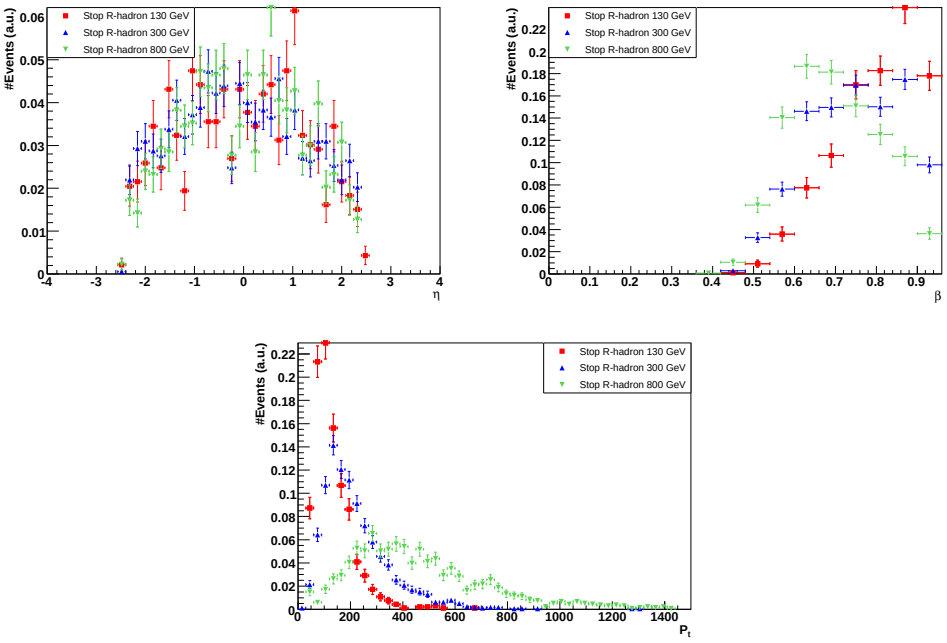

Figure 3.6: From left to right and up to down, the plots are distributions of the η, β, and p_T in stop R-hadron events, after data skimming.

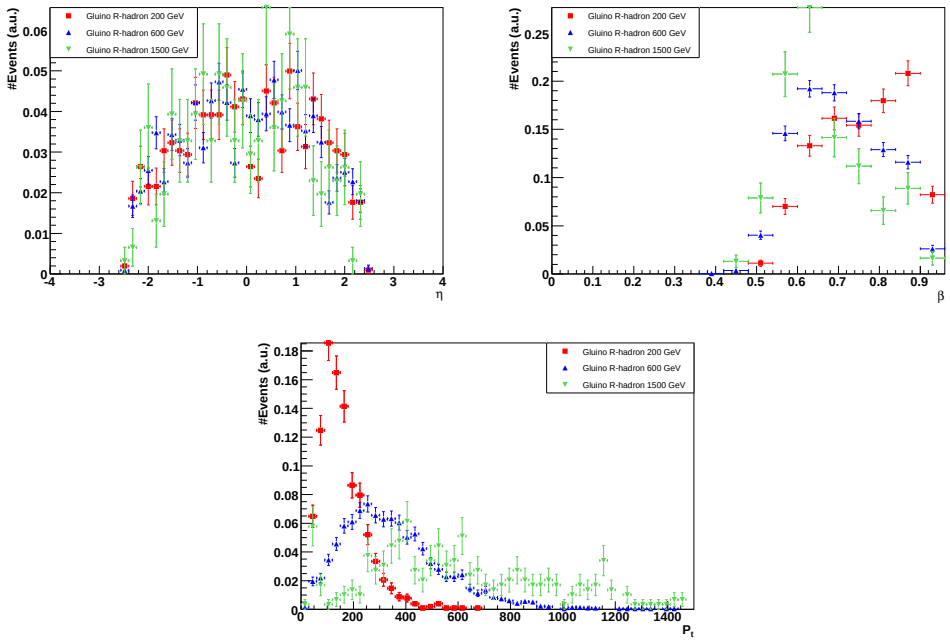

Figure 3.7: From left to right and up to down, the plots are distributions of the η, β, p_T in gluino R-hadron events, after data skimming.

Table 3.4: Fraction of signal events selected with the skim job running on the Muon PDS (second column), JetMET PDS (third column), in the combination of the two skims (fourth column), and overlap of events between the two skims (fifth column).

Sample	Mass	Muon	JetMET	Muon OR JetMET	Muon AND JetMET
stau	156	96.20%	85.45%	98.51%	83.14%
stau	247	95.30%	83.04%	98.57%	79.78%
KK tau	300	65.40%	11.80%	72.40%	4.80%
stop	130	21.07%	17.49%	33.42%	5.13%
stop	200	21.97%	25.30%	39.35%	7.32%
stop	300	22.21%	32.98%	46.71%	8.48%
stop	500	22.67%	39.19%	52.40%	9.45%
stop	800	21.71%	45.17%	56.47%	10.41%
gluino	200	20.53%	27.65%	41.52%	6.66%
gluino	300	21.15%	34.82%	47.87%	8.10%
gluino	600	20.41%	46.71%	56.30%	10.82%
gluino	900	15.60%	49.70%	56.20%	9.10%
gluino	1200	11.00%	55.70%	58.70%	8.00%
gluino	1500	10.30%	58.40%	61.10%	7.60%

Table 3.5: Number of background events in the various soups and for the two primary datasets. The total number of events is shown in the third column and the efficiency (without weights) is shown in fourth column. The last column shows for a given sample, the fraction of events (with weights) that are also selected in the corresponding sample of the other primary dataset (i.e. dataset overlap after skimming).

Primary Dataset	Soup	total #events	Skim efficiency	Overlap(%)
Muon	Stew	2.1M	0.016	0.15
	Gumbo	160K	0.21	0.24
	Chowder	5.1M	0.24	0.11
JetMET	Stew	3.8M	0.05	0.07
	Gumbo	6.5M	0.13	0.15
	Chowder	2.2M	0.20	0.50

Chapter 4

Particle Identification

It's straight forward to identify HSCPs at CMS. As a particle's momentum is

$$p = \beta\gamma mc \tag{4.1}$$

The momentum can be measured with the tracker and/or with the muon system accurately enough on the TeV scale (1% resolution at 100 GeV and around 15% resolution for 1-2 TeV), so measuring β makes it possible to find a mass hypothesis for a particle. If the mass is not compatible with any standard model stable particle, a heavy stable charged particle candidate has been found.

There are currently two methods to measure β in the CMS experiment. One is using the dE/dx information from the CMS silicon tracker, and the other is using the time-of-flight (TOF) information from the drift tube (DT) of the muon system.

4.1 Tracker dE/dx measurement

Moderately relativistic charged particles other than electrons lose energy in matter primarily by ionization and atomic excitation. The mean rate of energy loss (or dE/dx, energy loss per path length) is given by the Bethe-Bloch equation,

$$\frac{dE}{dx} = k\frac{Zz^2}{A\beta^2}[\frac{1}{2}ln\frac{2m_e\beta^2c^2T_{max}}{I(1-\beta^2)} - \beta^2 - \frac{\delta(\beta\gamma)}{2}], \tag{4.2}$$

where T_{max} is the maximum kinetic energy which can be imparted to a free electron in a single collision, Z and A are the atomic number and mass number of the absorber respectively, z is the charge of the incident particle, k is a constant 0.307075A MeV g^{-1} cm^2, $\delta(\beta\gamma)$ is the density effect correction to ionization energy loss, and I is the average excitation potential of the atoms.

Thus, given a certain detector, the energy loss depends mainly upon the charge and speed of the particle. Fig. 4.1 shows the energy loss for positive muons in copper as a function of $\beta\gamma$ [7]. We notice that for a large $\beta\gamma$ region (1–1000), the muon always has an energy loss about the same as the value at the minimum ionization point. Particles having the minimum energy loss are called Minimum Ionizating Particles (MIPs).

For particles with charge e in the $0.1 < \beta < 1$ region, Eq. 4.2 can be simplified as

$$\frac{dE}{dx} = K^{-1}\frac{1}{\beta^2}, \tag{4.3}$$

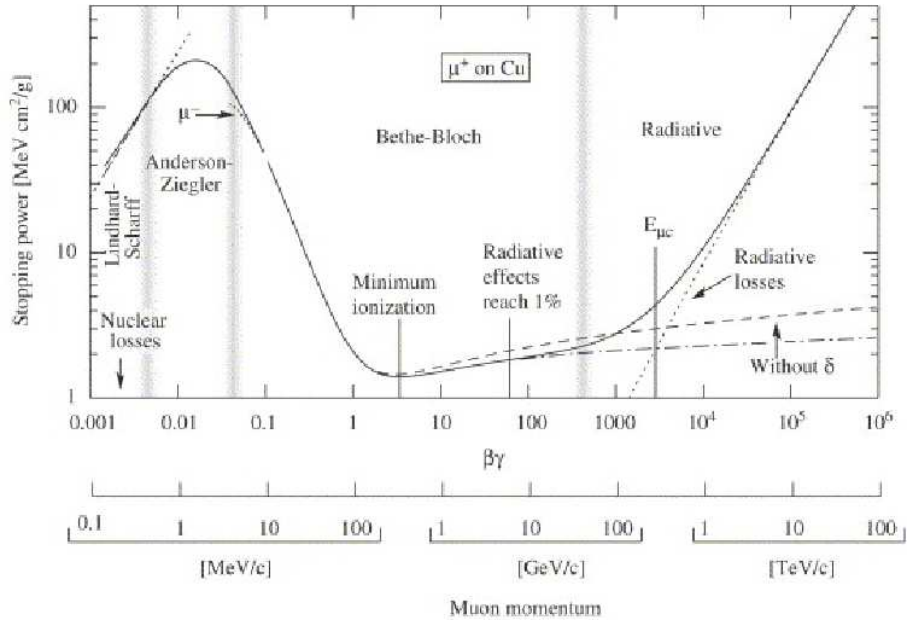

Figure 4.1: Muon energy loss in copper versus $\beta\gamma$.

so the β can be obtained from

$$\beta^{-1} = \sqrt{K\frac{dE}{dx}}, \tag{4.4}$$

with a measurement of dE/dx from the detector.

4.1.1 Tracker dE/dx measurement

Silicon detectors are p-n junction diodes operated with reverse bias, which forms a sensitive conductive region depleted of mobile charge. When a particle passes through the conductive region, the charges produced through ionization and radiation are swept to the electrode of the silicon detector, thus forming a electrical signal, and the pulse size is proportional to the energy loss of the particle. Therefore, it's possible to get a dE/dx measurement

given the thickness of the silicon.

The CMS Silicon Strip Tracker (SST) consists of a tracker inner barrel (TIB) (with four layers of silicon, two of which are double-sided layers), a tracker outer barrel (TOB) (with four single-sided layers and two double-sided ones), a tracker inner disk (TID) (with 3 disks per side: one single-sided and two double-sided) and two tracker end-caps (TEC) (with seven wheels per side: four single-sided and three double-sided). The double-sided layers have pairs of modules glued back to back, so that each of them gives two independent dE/dx measurements (hits).

The dE/dx measurement for a hit is approximated by

$$dE/dx = \frac{\Delta E}{L \cdot sec\theta}, \tag{4.5}$$

where L is the thickness of the silicon module,

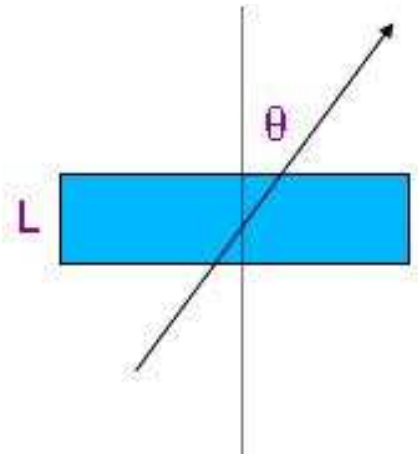

Figure 4.2: A track passes through a silicon module.

and θ is the angle between the track and the axis normal to the module, as

shown in Fig. 4.2. ΔE is the energy deposited by the charged particle. This energy is measured in ADC counts, N_{ADC}, which has a calibration factor N_{cal}, which is the number of electron-hole pairs per ADC count. The most probable charge deposition for a MIP in a 300 μm thick silicon layer is about 22,000 electron-hole pairs, and 250 electron-hole pairs per 10 bit ADC count. In silicon, 3.61 eV is the energy needed to create an electron-hole pair. The CMS counting room is 65 m away from the detector and the analog signal is transferred by optical fiber, which has a gain factor g, so the final ΔE goes as

$$\Delta E = \frac{N_{ADC}}{g} \times N_{cal} \times 3.61\ eV. \tag{4.6}$$

Two issues have to be mentioned here concerning the dE/dx hits measurement. It is found [53] that the maximum charge that can be transferred without any loss of information by tracker electronics is 80,000 electrons per strip, corresponding to 3.2 MIPs in the 320 μm modules and 2 MIPs in the 500 μm modules. Saturation occurs above this limit. So, the saturation of the tracker electronics might have serious effects on the search for HSCPs, which produce more ionization energy loss in silicon. However, the cluster is always shared between more than one strip (3.5–4 on average). For a HSCP with β=0.6, we expect its dE/dx is 2.78 times of a MIP, according to Eq. 4.3. So the saturation effect won't be a problem if we mainly care about HSCPs in the β range >0.6, which is required by the trigger system. Nevertheless, this saturation effect is simulated in the software. Another thing is the dE/dx hits from the pixel detector are not included in this study, due to the lack of

pixel dE/dx calibration software.

Once the dE/dx for a hit is measured, we have to know which track this certain hit belongs to. If we know the dE/dx value for the track, then together with the momentum measurement for the track, we can get a mass value for the track, using Eq. 4.1 and Eq. 4.4. As e, K, π, and p masses are quite different, we thus identify the particle type of the track. If we find n dE/dx hits belonging (associated) to the same track, then we can get the dE/dx for the track by estimating the most probable dE/dx value from the n associated dE/dx hit measurements. The hits association is done by tracking software. For CMS, it can be obtained from either the RS or CTF tracking algorithm.

Ideally, dE/dx for a track (the most probable dE/dx value for the track) can be obtained by a fit with the Landau distribution for all the associated dE/dx hits for the track. But at CMS, the limited number of dE/dx hits per track (14 on average) rules out the possibility of extracting this value from a fit. Alternatively, CMS adopts the generalized mean and the truncated mean methods [54]. For a good estimation of the most probable dE/dx value for a track, one expects the distribution to be as Gaussian as possible so that reliable particle identification can be made.

The generalized (or harmonic) mean is defined as

$$M_k(x_1, ..., x_n) = (\frac{1}{n}\sum_{i=1}^{n} x_i^{-k})^{-\frac{1}{k}}, \tag{4.7}$$

where k is the order of harmonic. The harmonic mean serves as a non-linear moving average which is shifted towards small signal values for big k and

emphasizes big signal values for small k. The truncated mean is simpler and widely used. First, x% of dE/dx hits with high measured values are discarded (truncated), and the rest are used to calculate the arithmetical mean.

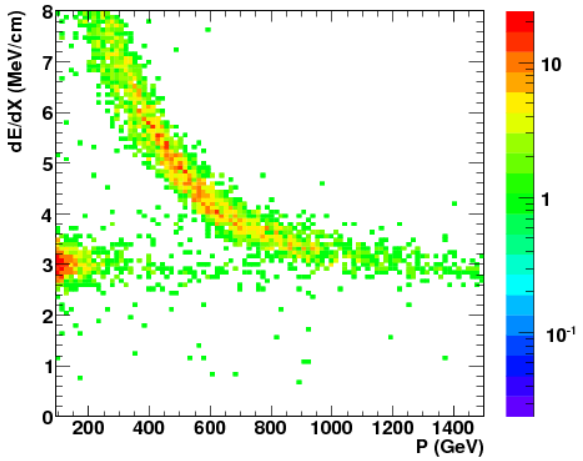

Figure 4.3: dE/dx versus momentum for a 500 GeV stop R-hadrons signal sample.

Fig. 4.3 shows the truncated40 (40% of higher hits are truncated) dE/dx estimation as a function of momentum. We see R-hadrons are clearly separated from SM tracks, and there is a clear band visible.

Fig. 4.4 from Ref. [55] shows Eq. 4.3 is a good approximation of dE/dx for the CMS SST in the β range we're mostly interested in, based on Monte-Carlo study. The value of β can be obtained from Eq. 4.4, and K can be calibrated from pure data samples like p from Λ decay, π from K_s decay, and e, μ from Z decay. In this analysis, we use a reconstructed proton MC sample to calibrate the constant K, and the resulting K, p mass distributions are plotted in Fig. 4.5. We see two Gaussian-like peaks at expected mass values,

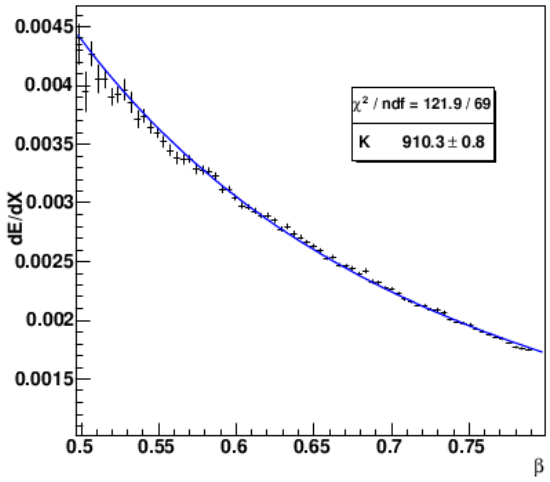

Figure 4.4: The dE/dx for a proton sample in the selected β region fitted to Eq. 4.3 with indicated value of K.

showing the dE/dx software works fine for SM particles.

The response of the tracker and the stability of estimators on MIPs can be tested by an inclusive selection of tracks with momentum $p > 5$ GeV from the CSA07 background samples. The result is shown in Fig. 4.6.

The tails of the track dE/dx distribution can be estimated directly on data as well as the probability of having a MIP with a measured β lower than a given value. With the available Monte Carlo sample, we can estimate (as shown in the right plot of Fig. 4.6) that the probability for a MIP to give a signal corresponding to $\beta < 0.8$ is less than 10^{-3}. The standard track reconstruction is limited to tracks with $p_T > 0.9$ GeV, but recent software improvements are expected to extend this limit to $p \sim 0.3 \div 0.5$ GeV. By using lower momentum tracks, the linearity of the tracker response and the behavior of dE/dx as a function of β can be further studied with proton or

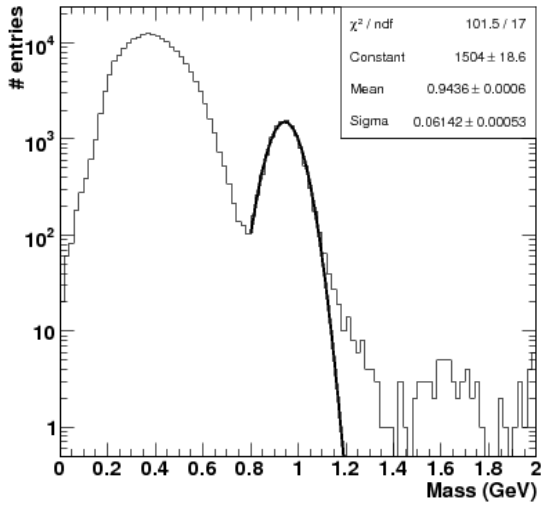

Figure 4.5: The reconstructed particle mass for particles with $P < 1.2$ GeV is shown and the proton mass is fitted with a Gaussian.

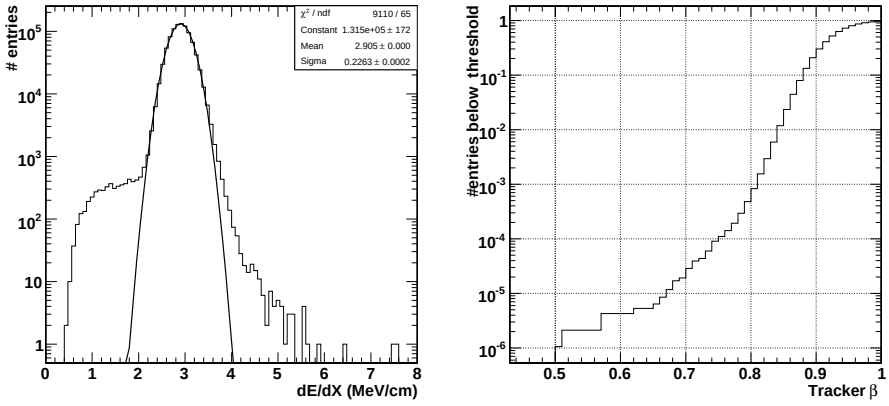

Figure 4.6: The plot on the left shows the dE/dx response to Minimum Ionizing Particles (MIP). The right plot shows the number of MIPs that satisfy a $\beta < cut$ selection.

kaon tracks.

Cosmic muons can be used to study the dE/dx distribution for muons when the tracker readout chip is operated in peak mode (pulse shape width of 75 ns). This motivates us to study dE/dx using the Tracker Integration Facility Data.

4.1.2 dE/dx Study Using Tracker Integration Facility Data

Tracker Integration Facility Setup

From November 2006 to July 2007, the four subsystems (TIB, TOB, TID and TEC) of the CMS silicon strip tracker were fully integrated and commissioned at the Tracker Integration Facility (TIF) at CERN. Due to the limited availability of read-out electronics and constraints from the data acquisition and cooling systems, only a partial read-out of the detector was allowed. The final TIF tracker setup consisted of 2161 modules that were read out, representing all four silicon strip sub-detectors. The majority of the read-out modules were located in a sector defined by $z > 0$ and $r > 0$. With about 1.3 million electronic channels, the tracker setup consisted of 15% of the final silicon strip setup.

The cosmic muon triggering was provided by scintillation counters mounted on the top and the bottom of the tracker. A trigger signal was generated based on the coincidence of any top with any bottom scintillation counter. Data were recorded in various trigger layouts, which are shown in Fig. 4.7. The trigger position A was expected to mainly result in TIB+TOB tracks,

hence the layout was modified to enhance the fraction of tracks crossing the TEC (trigger position B). Additional availability of scintillation counters extended the coverage of the trigger system and allowed the combination of trigger positions A and B into C. A lead plate with a thickness of 5 cm was located on top of the lower scintillation counter in all three trigger configurations to avoid triggering on very low momentum tracks. This translates into a minimal cosmic muon energy of 200 MeV for the trigger system.

During TIF running, no magnetic field is applied.

TIF Data Samples

Over 4.7 million events of cosmic ray data were recorded under different running conditions. Fig. 4.8 shows a cosmic muon passing through the TIB and TOB, leaving a nice track in the tracker.

Table 4.1 shows the available data sets for all the TIF running. In our dE/dx analysis, we only use the TIB+TOB+TEC configuration with trigger position C for its larger coverage and bigger data samples. We also ignore all data taken at -15 ^{o}C, because in order to reach this temperature, a large part of the tracker slice had to be turned off. Hence, the tracking results are rather unreliable.

The SST readout electronics can, depending on its configuration, output the raw silicon strip detector data in three formats:

1. Zero Suppression: standard operation used for proton-on-proton collisions, where signals are reordered to physical channel order. The subtraction of strip pedestals and common mode noise is also performed.

2. Processed Raw Data: used for heavy ion collisions, where signal re-

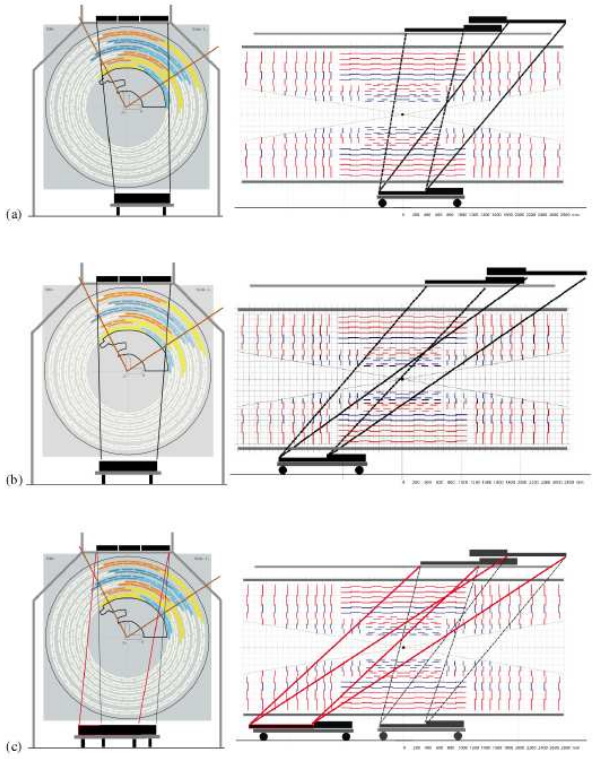

Figure 4.7: Layout of the various trigger scintillator positions used during the cosmic data taking at the TIF (in chronological order): (a) trigger position A; (b) trigger position B; (c) trigger position C. The xy view is shown on the left side, the rz view is shown on the right. The straight lines connecting the active areas of the top and bottom scintillation counters indicate the acceptance region.

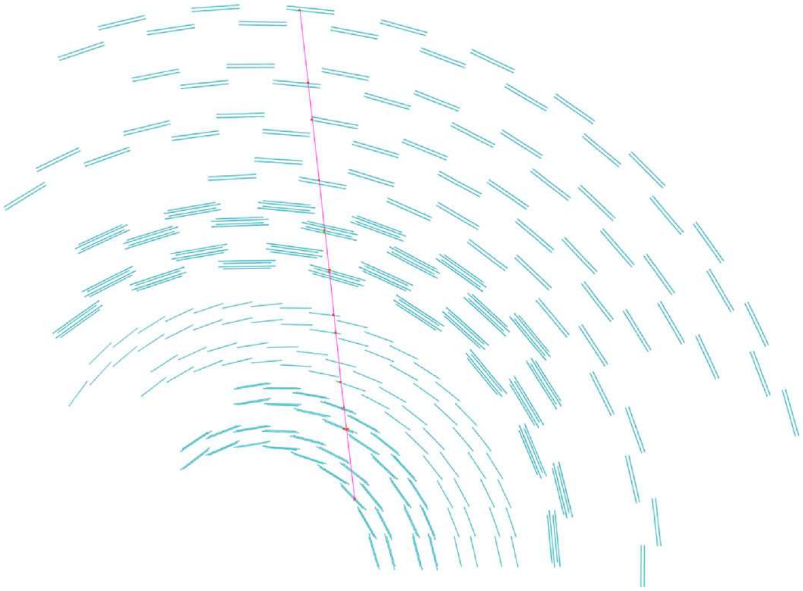

Figure 4.8: A cosmic muon passes through TIB and TOB at TIF.

Table 4.1: Available TIF data samples

Run Number	Active Detector	Trigger Position	T [^{o}C]	Total Events
6203 - 6930	TIB+TOB	A	15	703,996
7277 - 7296	TIB+TOB+TEC	A	15	191,154
7635 - 8055	TIB+TOB+TEC	B	15	193,337
7635 - 8055	TIB+TOB+TEC	B	15	193,337
9255 - 9341	TIB+TOB+TEC	C	15	132,311
10145 - 10684	TIB+TOB+TEC	C	10	992,997
10848 - 11274	TIB+TOB+TEC	C	-1	893,474
11316 - 11915	TIB+TOB+TEC	C	-10	923,571
12045 - 12585	TIB+TOB+TEC	C	-15	656,923

ordering and pedestal subtraction are performed, but there's no common mode subtraction.

3. Virgin Raw Data: used for testing, commissioning and calibration, where neither reordering nor pedestal/common mode subtraction is performed.

During TIF running, the main mode used is the Virgin Raw to enable offline debugging and calibration.

TIF dE/dx Results

We calculate dE/dx for tracks, using the virgin raw data from the TIB+TOB +TEC configuration and trigger position C, with events containing only one track. We use -10 ^{o}C data for most studies as it's the nominal temperature for the tracker in real data taking. A track is deemed as good if it has a number of dedxhits>4 (associated hits from tracks with added dE/dx information for the hits) and the track fitting χ^2/DOF < 10.

In principle, the track dE/dx should not depend on the tracking algorithms used to find a certain track. The track dE/dx estimation is based on the dE/dx hits (cluster charge size, hit angle etc.) associated to the track, which are calculated in the TrackRefitter (a CMSSW EDM event class). Here, a reconstructed track information from either the RS or CTF algorithm just provides the associated hits for the track and is used as an input source for the TrackRefitter. Therefore, as long as RS and CTF find the same track with same number of hits for the track, the dE/dx for the track will be the same for both tracking algorithms. We tested this idea by looking at tracks recognized as good by both the RS and CTF tracking algorithms, and

the resulting dE/dx means and resolutions for tracks are exactly the same from both algorithms. To get rid of tracking algorithm dependence for this dE/dx study, we only use those events whose single track is recognized as good by both algorithms for the following discussion.

As studied by Ref. [54], the truncated mean and harmonic mean are the two main dE/dx estimators for CMS. So in this study, we mainly compare the truncated40, truncated20, harmonic4, and harmonic2 track dE/dx estimators. Fig. 4.9 shows the dE/dx estimations by four different estimators. All the estimators show good Gaussian distributions, indicating that we have a very pure cosmic muon sample here.

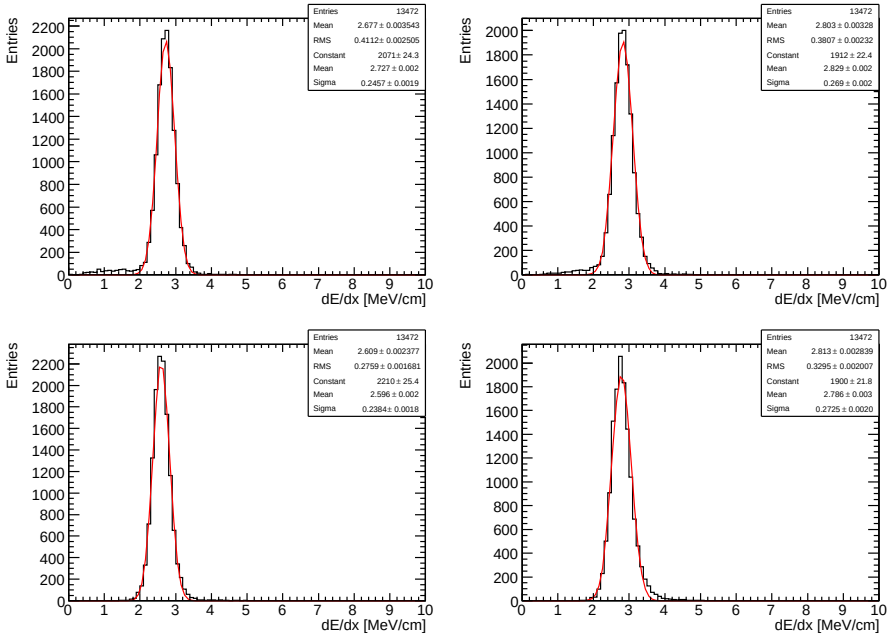

Figure 4.9: Different track dE/dx estimators for TIF data at -10 ^{o}C. Upper-left: Harmonic4, Upper-right: Harmonic2, Lower-left: Truncated40, Lower-right: Truncated20.

The calculated dE/dx resolutions are shown in Table 4.2, and we see that

Table 4.2: dE/dx resolutions for different estimators using TIF data

dE/dx Estimator	Resolution (%)
harmonic4	9.01±0.07
harmonic2	9.51±0.07
truncated40	9.18±0.07
truncated20	9.78±0.07

harmonic4 does give the best dE/dx resolution (determined from the fitted sigma value divided by fitted mean value), and truncated40 is better than truncated20. This is consistent with Ref. [54]'s MC study. But the harmonic estimation gives a small left tail. This tail will give higher signal efficiency loss if we simply make a 3σ cut around the gaussian peak for the particle identification, and the systematic on the distribution will be hard to evaluate.

To understand what causes this left tail for the harmonic estimator, we use a toy MC sample to simulate the dedxhit measurements, then use those hits to calculate the harmonic4 and truncated40 estimators. Fig. 4.10 shows the dedxhits measurements with a perfect Landau distribution, and the resulting harmonic4 and truncated40 estimations. Both estimators show good Gaussian distributions as expected, confirming the toyMC code works fine. When we add a tiny gaussian around 1.5 in the dedxhits distribution, as shown in Fig. 4.11, the harmonic4 estimator shows a clear left tail, while truncated40 keeps a good behavior in the left tail region.

So as long as the dE/dx hits distribution is not a perfect Landau, i.e., it has a tiny left tail, a left tail will show up in the harmonic estimation. This can be explained from the definition of harmonic estimator in Eq. 4.7,

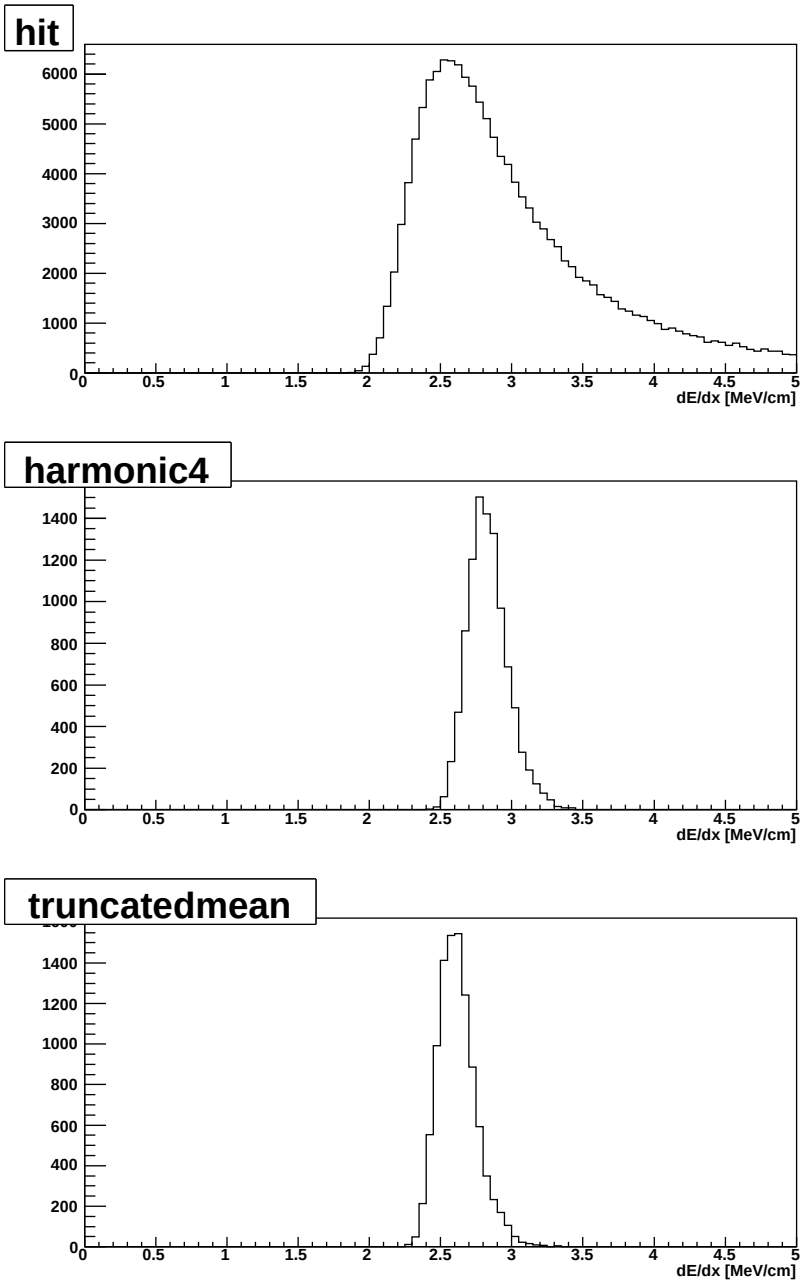

Figure 4.10: Truncated40 (bottom) and harmonic4 (middle) estimations for perfect Landau distributed dE/dx hit (top) measurements, using toy MC events.

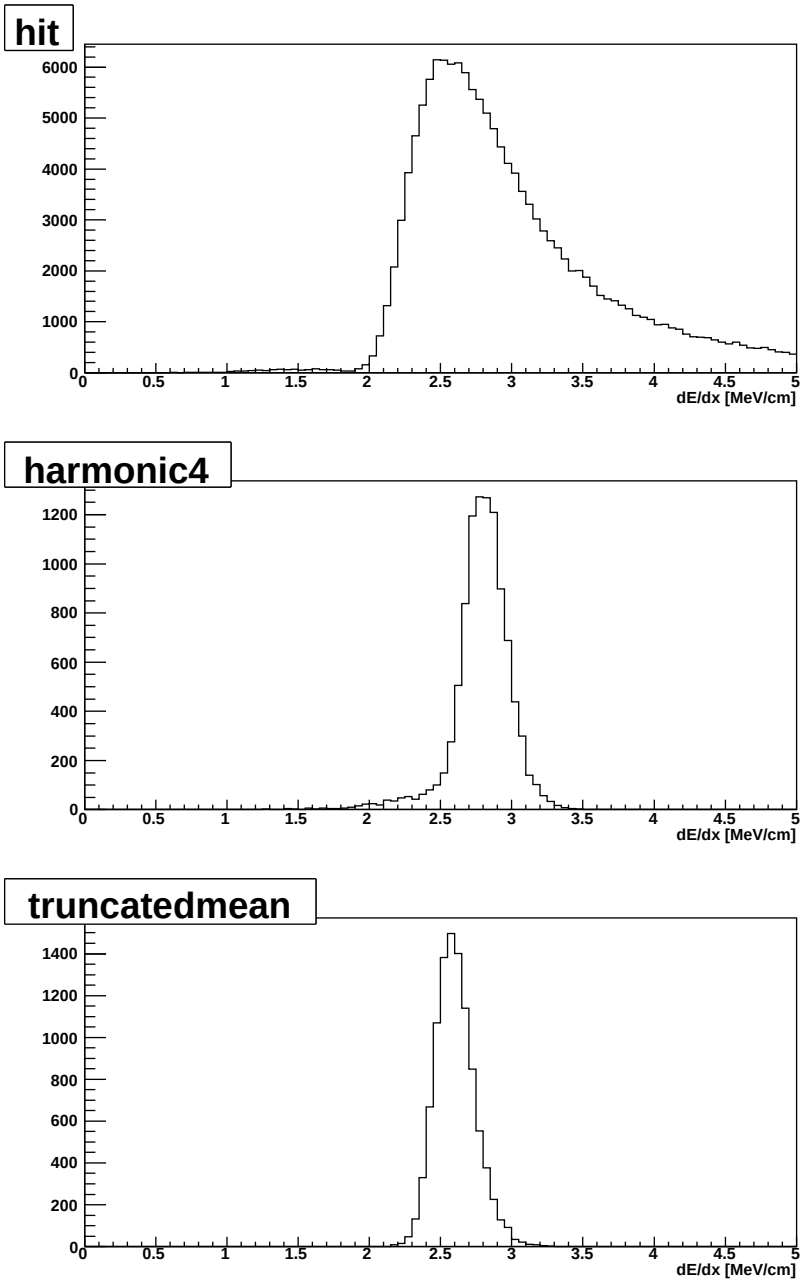

Figure 4.11: Truncated40 (bottom) and harmonic4 (middle) estimations for non-perfect Landau (with a small gaussian tail in left tail) distributed dE/dx hit (top) measurements, using toy MC events.

in which hits with low measurements weigh in heavier in the harmonic calculation, especially when a hit has a dE/dx value <1. The truncated mean estimation also gets rid of some of high valued measurements, but due to the fact that it's still an arithmetical average of the rest of the measurements, the truncated mean is not as sensitive to a few relatively lower measurements.

As the dE/dx resolution improves with increased numbers of dedxhits, the dE/dx resolution from TIF data is expected to be poorer than the real full tracker configuration data. The full tracker configuration results in an average number of 16 dedxhits for a track, compared to on average 5 dedxhits for TIF data. To check the resolution variation versus the number of dedxhits used, in Fig. 4.12, we plot truncated40 with three different dedxhits cuts:

1. number of dedxhits is 5 or 6
2. number of dedxhits is between 8 and 10
3. number of dedxhits >15 (to mimic standard LHC physics data taking, where the full tracker is commissioned.)

The resolutions obtained are (11.57±0.21)%, (9.29±0.10)% and (6.35±0.17)% respectively. As a reminder, Ref. [54]'s MC study shows truncated40 has a resolution of 5.18% for muons. This rough consistency between MC and TIF data assures us that we can achieve the expected dE/dx resolution for the real LHC data with the full tracker configuration, provided there are good tracks found.

We also study the possible temperature dependence [53] for track dE/dx, using the truncated40 estimator, with data taken at temperatures -10 ^{o}C, -1 ^{o}C, and 10 ^{o}C.

The result is shown in Fig. 4.13, and the dE/dx means and resolutions are

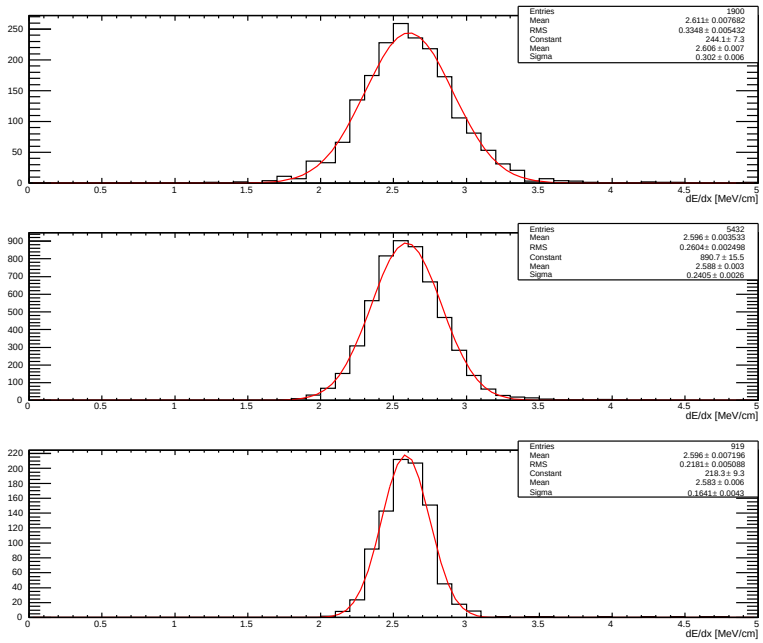

Figure 4.12: dE/dx resolution variation with respect to number of dedxhits used: number of hits used are 5 or 6 (top), between 8 and 10 (middle), and >15 (bottom). A clear trend can be seen that the dE/dx resolution gets better with increasing numbers of dedxhits.

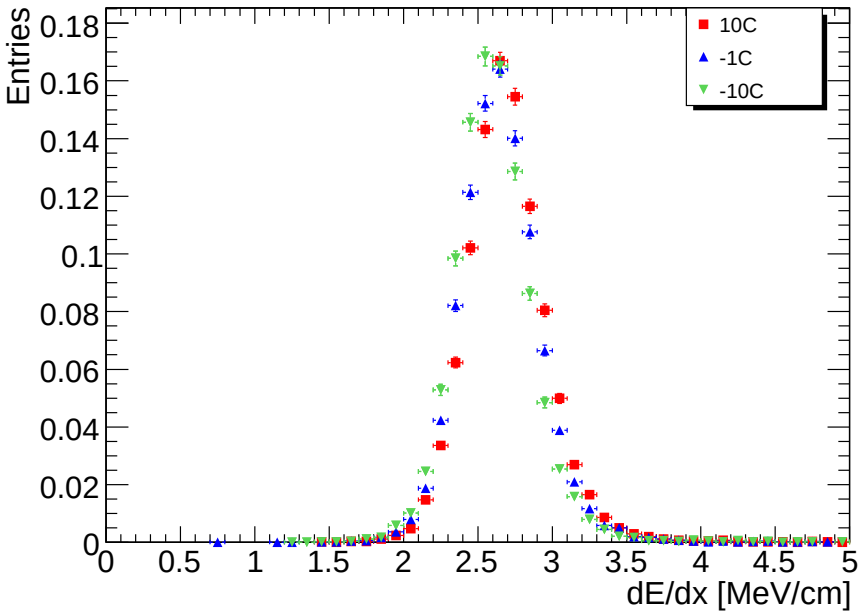

Figure 4.13: The track dE/dx truncated40 variation with respect to different temperatures.

Table 4.3: dE/dx means and resolutions for TIF data taken at different temperatures

Temperature(^{o}C)	Mean (MeV/cm)	Resolution (%)
-10	2.596±0.002	9.18±0.07
-1	2.643±0.002	9.45±0.06
10	2.684±0.002	9.35±0.06

listed in Table 4.3. A slow increase of 0.0044±0.0001 MeV/cm/^{o}C ((2.684-2.596)/20) for the dE/dx mean value is observed as the temperature increases. This is only a 0.17% effect. The resolution changes are also small. So the temperature effect in dE/dx is negligible for this study. The effect can be due to the non-perfect hardware tickmark calibration [56], as the tickmark is a rough 3-setting hardware gain calibration.

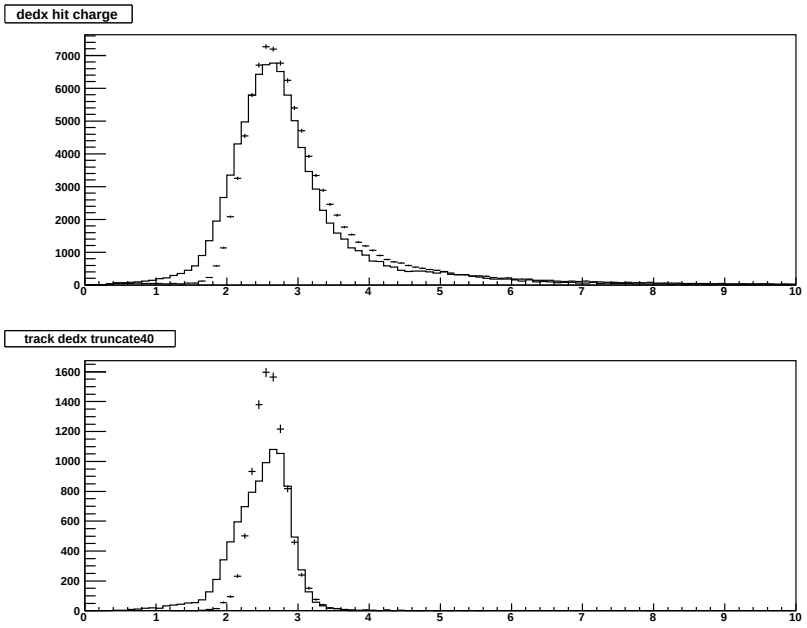

Figure 4.14: Preliminary: data/MC comparison for dE/dx hits charge (top) and track dE/dx (bottom) estimated by truncated40. Data are shown as points while the histograms are MC.

The TIF MC sample is still being tuned. Here, we show preliminary results using a subset of the TIFCosmicMuon data set, and compare it to the dE/dx hits measurement (the angle and thickness normalized, calibrated energy release for dE/dx hits) and the track dE/dx found by the truncated40 estimator using data and MC. We see the data for dE/dx hits (upper panel in Fig. 4.14) follow a good Landau distribution, while MC (histogram) is wider than data in the left tail region. That's why the track dE/dx by truncated40 from MC is wider than data (lower panel). Initial investigation shows the problem might be due to the cluster charge integration calculation for MC. Further work is ongoing.

From the upper panel in Fig. 4.14, we also can see a very tiny left tail for the dE/dx hits measurement from data. This confirms our previous explanation of the source of the left tail found using the harmonic estimator.

The TIF data dE/dx study here may not be so important in this HSCP analysis, but it does assure us that we can achieve the expected dE/dx resolution with physics data, which is the basis for the HSCP mass measurement. Also we see from Fig. 4.14, the data and MC are consistent in the right tail region for the track dE/dx distribution, giving us some confidence in the muon background estimation from MC.

4.2 Drift Tube Time of Flight measurement

A charged particle traversing the drift tube will produce electron-ion pairs along its path. The ionization electrons are eventually collected by a thin anode wire in the center of each tube, where a strong electric field, increasing

as $\frac{1}{r}$, accelerates the electrons enough to produce secondary ionization and hence an avalanche. The electrons produced in the avalanche are collected by the wire in a few nanoseconds and generate a signal (voltage pulse) that can be detected with an amplifier. The radius from which the electrons drift to the wire (DT hit position) is measured by obtaining the time of the voltage pulse t_w on the wire relative to a global time t_c. Normally t_c is chosen as the time when a collision happens. This way, we obtain a hit position with Eq. 4.8

$$x = x_w + v_d \times (t_w - t_c), \tag{4.8}$$

where v_d is the drift velocity of the released electrons in the gas mixture.

4.2.1 β^{-1} Estimation Using TOF at CMS

The CMS barrel muon detector is made of four stations forming concentric cylinders around the beam line. Each station except the outermost contains three super-layers (SL), each composed of four DT layers. Two of the SLs measure the $r-\phi$ coordinate and third one measures the z coordinate. There are only two SLs in the outermost station, with no z SL. Drift Tubes are 2$\sim$3 m long, 12 mm high and 42 mm wide. The maximal drift distance to the sensitive wire is 20 mm. Because tubes in consecutive layers are staggered by half a tube, a typical track passes alternatively to the left and to the right of the sensitive wires in consecutive layers, viewed in a two dimensions: r and z (see the left sides of Figs. 4.15 and 4.16).

At CMS, the global time t_c (time of flight from the interaction point to the Rechit for a SM muon) and drift velocity are treated as constants during

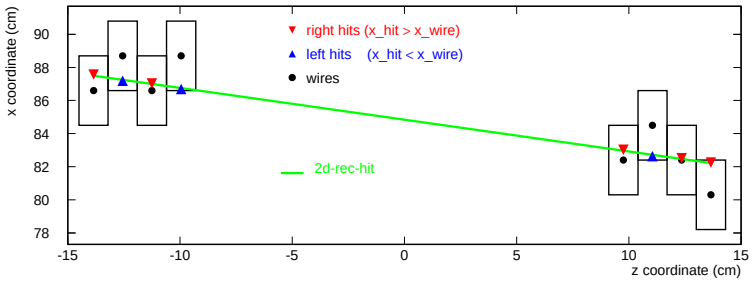

Figure 4.15: DT display of twin $r - \phi$ super-layers

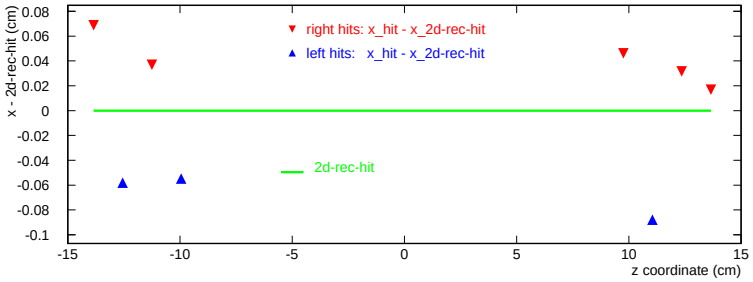

Figure 4.16: Zig-zag pattern of hits

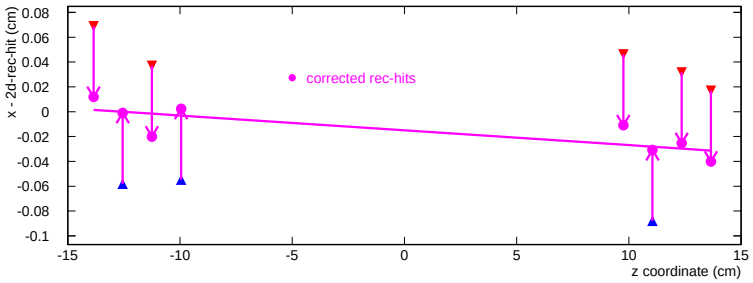

Figure 4.17: $\langle \delta_x \rangle_{SL}$ correction

a run, measured by fitting calibration data before each beam injection in the LHC. A particle that travels with β significantly less than 1 will arrive much later in the muon system. So the t_c in Eq. 4.8 needs some correction. As the distance a muon travels before hitting the first muon DT is,

$$\begin{aligned} d &= ct_c \quad \text{for muon;} \\ &= \beta c t'_c \quad \text{for slow moving particles.} \end{aligned} \tag{4.9}$$

Eq. 4.8 now becomes

$$x' = x_w + v_d \times (t_w - \frac{d}{\beta c}). \tag{4.10}$$

Taking $x - x'$ from Eq. 4.8 and Eq. 4.10 as δx, we obtain

$$\begin{aligned} \beta^{-1} &= 1 + \frac{c \cdot \delta x}{d \cdot v_d}, \\ &= 1 + \frac{c}{d}\delta_t, \end{aligned} \tag{4.11}$$

here we define $\frac{\delta x}{v_d}$ as δ_t, the off-time correction.

The 1D Rechit (z) associated with a local track element (x, 2D Rechit with $r - \phi$ information) form a zig-zag pattern which can be aligned by an appropriate t_c correction for HSCPs (off-time correction δ_t). The expected value $\langle \delta_t \rangle$ for muons originating at the primary vertex of the correct bunch crossing (BX) should be equal to zero by construction, but it will differ from zero for off-time particles. In particular, for HSCP particles which travel with velocity $\beta < 1$, the average value $\langle \delta_t \rangle > 0$.

A group of 1D Rechits with a local track element (2D Rechit) in a given super layer (SL) allows the determination of $\langle \delta_t \rangle_{SL}$ if the coarse position along the drift tubes is known sufficiently well. The correction $\langle \delta_t \rangle_{SL}$ should already be made at the local pattern recognition stage if reconstruction is to be effective for off-time particles or during the start-up period when timing of the system is not yet optimal. Such a local pattern recognition algorithm has been developed and tested [57]. The only change with respect to the standard algorithm is the way in which 1D Rechits are associated with the 2D Rechit.

The estimate of the correction is made at the level of 2D Rechit reconstruction and then again independently after muon candidate reconstruction. This can be done for a SL containing at least 3 1D Rechits and at least one left and one right Rechit.

In the first step, for each super layer j which has at least three associated Rechits, a corrected local track segment (2D Rechit) is analytically calculated, taking into account the possibility that the particle causing it was off-time. For this purpose, regression lines for left and right hits are separately determined.

$$x_{ij}^L = a_j^L + b_j^L \cdot z_{ij}, x_{ij}^R = a_j^R + b_j^R \cdot z_{ij} \tag{4.12}$$

where x_{ij}^L and x_{ij}^R are left and right Rechit local coordinates along the drift direction, z_{ij} is the local layer position, and a,b are regression parameters. A Rec-hit is called "left" or "right" depending on which ambiguous position is associated to the track. For the left (right) Rechit, the difference $x_{ij} - x_w$

is negative (positive). If there is only one left or one right hit then a pseudo-regression line is drawn parallel to that calculated for the opposite hits ($b_j^L = b_j^R$). Determination of β^{-1} is not possible if there are only left or only right hits in the superlayer.

Finally, the corrected 2D Rechit is determined taking average values

$$a_j = \frac{a_j^L + a_j^R}{2}, b_j = \frac{b_j^L + b_j^R}{2} \tag{4.13}$$

The approach is shown schematically in Figs. 4.16 and 4.17. Both figures show hits generated by a delayed particle after δ_t adjustments (for a muon, all hits should be aligned to a line). Figure 4.16 shows the difference between the 1D Rechit position along the drift direction and the regression line drawn without taking into account the possibility that hits could be generated by an off-time particle. In the right half of the figure there are more right than left hits which causes these hits to be closer to the line (the line is drawn horizontally due to the definition of the vertical axis of the figure, but in reality the line is tilted towards the right-hand side points). To avoid such bias it is necessary to introduce the δ_t parameter in the regression line calculation, with which all hits can be moved closer to or further from the sensitive wire. Such a solution is shown schematically in Fig. 4.17. The hit positions are the same as in the preceding figure. The corrected hits are shown with full circles, arrows represent the correction and a regression line is drawn through the corrected hits.

The implementation of this approach used in the present analysis is as follows. For each 2D segment with at least 7 1D Rechits and an associated

segment in the other projection (the outermost SL is not used), the regression line is calculated by a least-square analytical fit with three parameters: regression coefficient, regression offset, and off-time correction $\delta_x = v_{\rm d} \cdot \delta_t$. For genuine muons a distribution of the correction described above should have an average equal to zero. However, for tracks which are due to HSCP particles, the correction should be positive because of the time delay.

For each super layer j with n_j Rechits, there are n_j -2 independent β^{-1} measurements, because the two parameters a_j, b_j are determined at the same time. The final β^{-1} estimate is obtained by a proper weighted average, which takes all of the available information from the N super layers into account. For each Rechit $i = 1, n_j$ in each SL $j = 1, N_{SL}$,

$$\left(\frac{1}{\beta}\right)_{ij} = 1 + \frac{c}{v_{\rm d}}\frac{(\delta_x)_{ij}}{d_{ij}}, \tag{4.14}$$

where $(\delta_x)_{ij} = |x_{ij} - x_w| = |a_j + b_j z_{ij} - x_w|$ and d_{ij} is the flight distance between the interaction point and the Rechit. The drift velocity is taken to be equal to that used for simulation $v_d = 53.4$ μm/ns.

The analytic solution for the average β^{-1} and its error (estimated as the dispersion of the β^{-1} measurements) is

$$\left\langle \frac{1}{\beta} \right\rangle = \frac{\sum_{j=1}^{N_{SL}} \frac{n_j-2}{n_j} \cdot \sum_{i=1}^{n_j} \left(\frac{1}{\beta}\right)_{ij}}{\sum_{j=1}^{N_{SL}} (n_j - 2)} \tag{4.15}$$

$$\Delta\left(\frac{1}{\beta}\right) = \frac{\sqrt{\sum_{j=1}^{N_{SL}} \frac{n_j-2}{n_j} \cdot \sum_{i=1}^{n_j} \left\{ \left(\frac{1}{\beta}\right)_{ij} - \left\langle \frac{1}{\beta} \right\rangle \right\}^2}}{\sum_{j=1}^{N_{SL}} (n_j - 2)} \tag{4.16}$$

The response of the method described above on muons from a background

sample is shown in Figures 4.18 and 4.19, where β^{-1} and its error distributions are shown, respectively. In Figure 4.18, one could spot tails in the β^{-1} distribution. The tail for large values of β^{-1} is especially dangerous for the present analysis, since large β^{-1} is the signature of the signal that we're looking for. However, after a cut at $\Delta(\beta^{-1}) < .07$ this tail is eliminated as shown in Figure 4.20. In Figure 4.21, the pull distribution $(\beta^{-1} - 1)/\Delta(\beta^{-1})$ is shown for completeness.

As shown in Figure 4.20, the tails corresponding to a $\beta < 0.85$ ($\beta < 0.80$) are of the order of 10^{-3} (10^{-4}).

4.3 Possible Identification Methods Using Other Detectors

4.3.1 ECAL dE/dx Measurement

The CMS Electromagnetic Calorimeter (ECAL) can be used to measure the dE/dx of an HSCP candidate. An HSCP will travel more slowly than a muon or a pion, due to its large mass, and will therefore deposit more energy in the ECAL.

For muon-like HSCPs, the dE/dx measurement will be used to reject background events due to muons. For a candidate HSCP traveling through one ECAL crystal, the dE/dx measurement will be dominated by the 40 MeV electronic noise, which is ≈16% of the energy deposit expected for a typical muon track. Therefore, if an HSCP candidate is expected to have $\beta \approx 0.8$, the dE/dx measurement of a muon must fluctuate upward by about

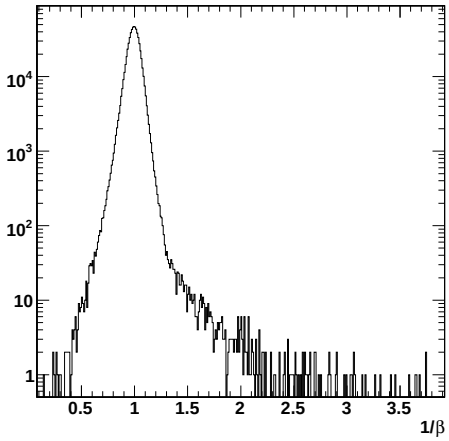

Figure 4.18: β^{-1} distribution for genuine muons

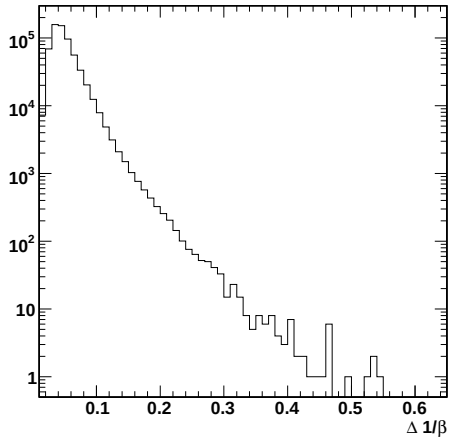

Figure 4.19: $\Delta(\beta^{-1})$ distribution for genuine muons

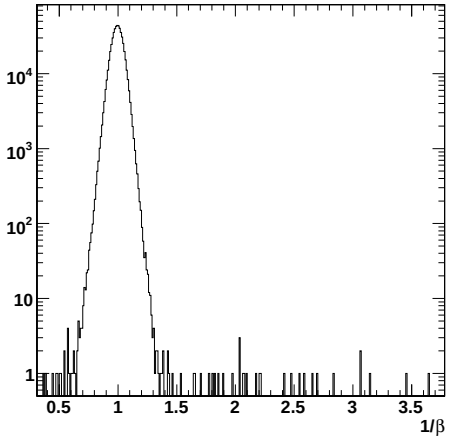

Figure 4.20: β^{-1} distribution for genuine muons after $\Delta(\beta^{-1}) < .07$ cut

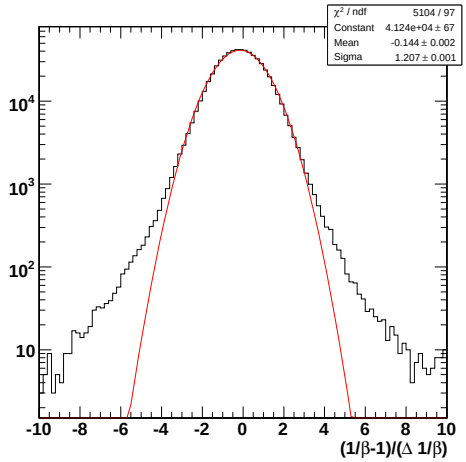

Figure 4.21: $(\beta^{-1} - 1)/\Delta(\beta^{-1})$ pull distribution for genuine muons

4σ to look like an HSCP. If the expected β of the HSCP is 0.6 instead, the fluctuation required would be over 10σ.

The discrimination power of the ECAL dE/dx measurement above is most likely determined by the non-Gaussian high-end tail of the muon dE/dx distribution. Therefore, this distribution can be studied using Monte Carlo models in the near future and checked with muon data from, for example, a W+jet sample. As the ECAL discrimination power is statistically independent of the tracker dE/dx measurement, our HSCP discovery potential will improve significantly.

R-hadrons can interact either in the tracker or ECAL and produce higher energy deposition than expected for a muon-like particle with the same velocity. For the detection of such a particle, the most likely source of background would be isolated pions. Therefore, one needs to study the expected dE/dx distribution of pions in Monte Carlo models and in data. Because pions deposit more energy in the ECAL than muons, the discrimination power of the ECAL dE/dx will be reduced.

Another possible study can focus on the possibility of correlated dE/dx fluctuations in the tracker and ECAL. If a photon is radiated by a muon candidate, and then travels along the muon track and converts to an electron-positron pair, it could cause dE/dx measurements to increase in both the tracker and ECAL. This could cause a background for both R-hadrons and muon-like HSCPs. If this becomes a significant source of background, the ECAL dE/dx measurement will become less important. Therefore, detailed studies of the probability of this type of event are essential.

4.3.2 CSC Time-of-Flight Measurement

It is expected that the time-of-flight can be extracted from the cathode strip chambers (CSCs) with modest resolution, mainly due to a large number of independent time measurements. The per-plane drift time distribution is fairly Gaussian between 0 and 50 ns with a small tail extending to 75 ns, and has an RMS of about 10 ns. A penetrating track can supply of order 20 such measurements, leading to an expected intrinsic time resolution for the track as a whole of around 2-3 ns. This resolution will be slightly degraded by the time digitization on the front end electronics, which samples the discriminated wire signals at 25 ns (bunch crossing) intervals. This effect corresponds to an additional smearing of the 10 ns per-plane RMS of the drift time distribution by roughly an additional 7 ns, i.e. 25 ns divided by the square root of 12. Therefore, one expects a per-track resolution of about 3 ns. All of these rough estimates are now being investigated through the use of the CSC simulation by the HSCP physics analysis group.

4.4 Backgrounds

As we'll mainly use muon trigger events for the analysis, the primary sources of backgrounds will be reduced to events containing muons. The first muon background source is from a low p_T muon with overlapping muon tracks. It should not be a major issue as the occupancy of the tracker and muon detectors is low (we expect 100 tracks per event or 2500 tracks per bunch crossing with pileup included, but we have 10 million tracker channels). Another source of muons comes from the weak decays of the W and Z. These muons

would have a p_T around $m_Z/2$, so it is also not a background for HSCP signals. But weak decays of high p_T b-quarks and t-quarks will produce high p_T muons, and thus present a serious background. With the isolation requirements applied, the QCD background would be further reduced. If HSCPs are pair produced in an event, as suggested by most theoretical models, Drell-Yan production of muon pairs would become the dominant backgrounds.

Therefore, the main backgrounds we will encounter are Standard Model muons, whose SST dE/dx measurement fluctuates to high values. The tracker dE/dx background is hard to simulate in MC. The best estimation can be obtained using a control sample from data with low momentum (all tracks with < 50 GeV momentum for example), where the HSCP signal would not contribute, and calculating the fraction of tracks with dE/dx high enough to correspond to a small β.

4.5 Strategies for HSCP Identification

Several strategies can be followed to select events according to the expected signal signature. We expect three slightly different heavy stable charged particle signatures:

- A lepton-like massive charged particle (stau, KK-tau)
- A charge-flipping massive particle (stop, gluino)
- A charge-flipping massive particle always produced as neutral (a gluino produced as gluon-gluino ball)

In the second and third scenarios, the momentum measurement obtained from the muon system is not reliable because of the charge flipping between muon stations. For the second scenario this problem can be simply solved by using the tracker-measured momentum. The third scenario is clearly more difficult, and requires a separate study. The lack of tracker tracks in that case also makes it more difficult to reject cosmic muon background.

Thus, we can have three different particle identification strategies: Tracker-standalone, DT-standalone, and Combined identification. The stand alone measurements will help if there is an unexpected problem in one of the two detectors during early data taking. The DT standalone candidate selection is also appropriate when the hadron is neutral at production.

4.5.1 Combined Selections

In order to maximize the background rejection, we use the combined selection as our main method of identification, based on the two measurements of β in the DT and Tracker.

General selection

To maximize the signal to background ratio, we can combine the two β measurements and reduce the background to a negligible level without significant loss of the signal. The first step of the selection process is to associate the candidate HSCP measured in the muon system with that measured in the tracker. All the muon tracks reconstructed in the muon system with $p_T > 30$ GeV are considered as HSCP candidates. For the tracker candidate,

a pre-selection is applied requiring:

- $p_T > 30$ GeV
- $\beta_{tk} < 0.9$
- $\#dE/dxhits >= 9$
- $\chi^2/DOF < 5$

The two collections are associated by geometric and momentum compatibility. In order to associate two candidates, the following requirements should be met:

- $\Delta(1/p_T) < 0.005$ GeV^{-1}
- $\Delta R < 0.1$.

If more than one match satisfies the above criteria, the closest in ΔR is selected.

Fig. 4.22 shows the distribution of β_{DT}^{-1} vs β_{Tk}^{-1} for background and signal events after matching. For signal events, the two measurements are clearly correlated. There is no correlation between the measurements at high β^{-1} in the background case. Therefore for the combined DT and tracker analysis it is possible to require that the two measurements are compatible, with or without a threshold requirement on each.

The following cuts are hence used to define a background-free region:

- $\beta_{DT} < 0.80$ and $\sigma_{\beta^{-1}} < 0.1$
- $\beta_{Tk} < 0.80$

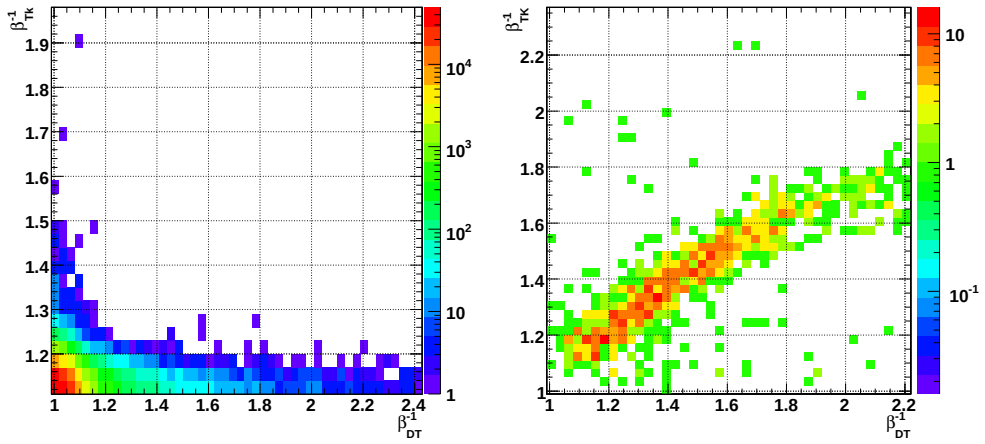

Figure 4.22: Distribution of β_{Dt}^{-1} as a function of β_{Tk}^{-1} for muon background from CSA07 soup (left) and for a 500 GeV stop signal sample (right).

- $m_{avg} > 100$ GeV

The efficiency of the first two cuts can be measured independently, and it can be assumed that there is no correlation between the two measurements for the background. Therefore these two cuts alone provide a rejection of $\sim 10^{-7}$, i.e. $\sim 10^{-1}$ events expected in 1M events (~ 1 fb^{-1} for the muon primary data set after skimming. No events from the CSA07 soup samples pass the above selection. The efficiency of the above selection for signal samples is reported in Table 4.4. The η, β and p_T distributions after above selections are shown in Fig. 4.23, Fig. 4.24, and Fig. 4.25 for lepton-like, stop, and gluino HSCPs, respectively.

To give reader an easier comparison on η, β and p_T distributions between generation level, skim level, and final selection level, and thus have a better idea how the efficiency goes with different cuts, Fig. 4.26 shows the three level distributions for 600 GeV gluino HSCPs in η, β, and p_T respectively.

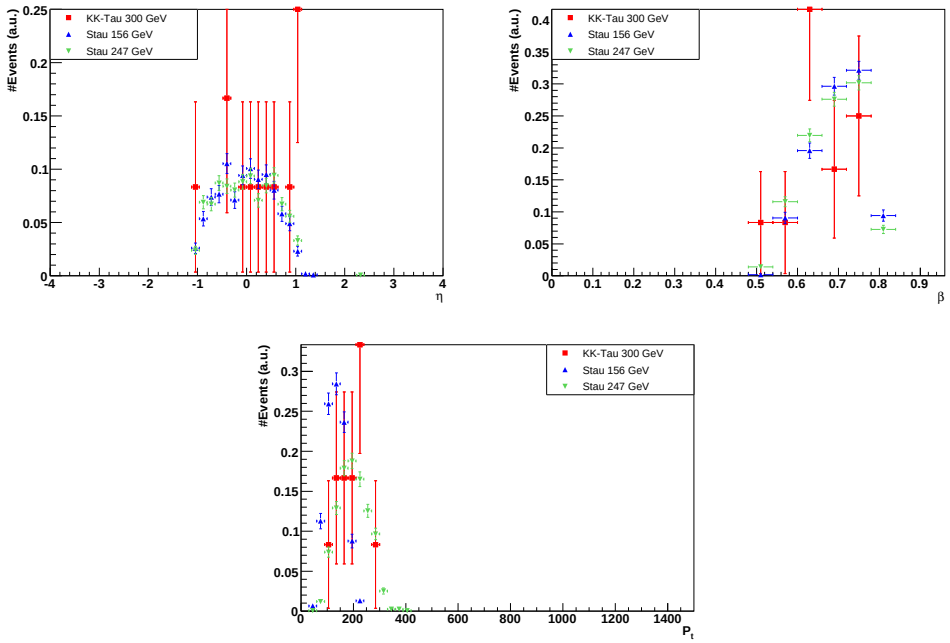

Figure 4.23: From left to right and up to down, the plots are distributions of the η, β, and p_T in lepton-like HSCPs (stau/KK tau) events, after final selection in combined analysis.

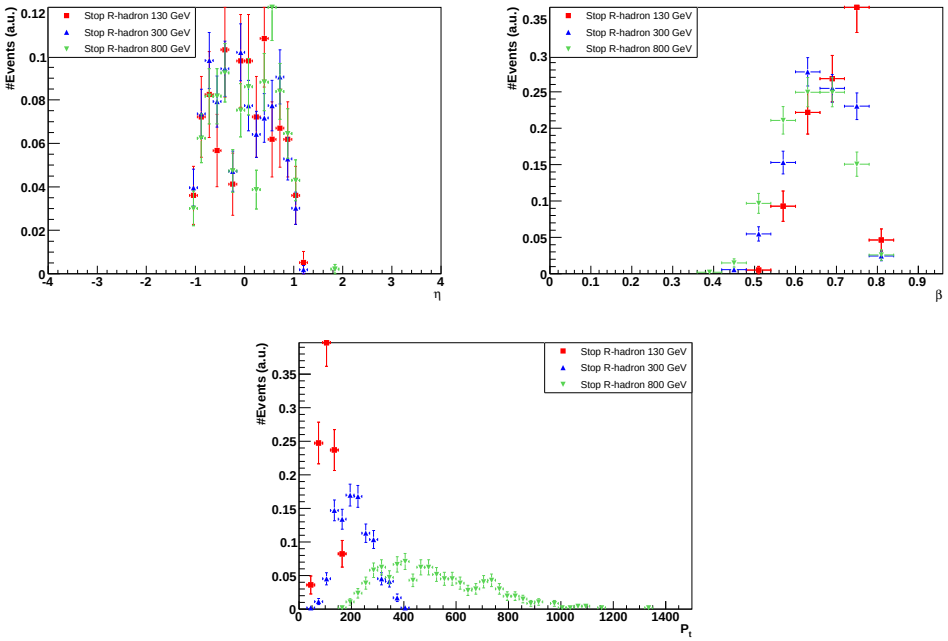

Figure 4.24: From left to right and up to down, the plots are distributions of the η, β, and p_T in stop R-hadron events, after final data selection in combined analysis.

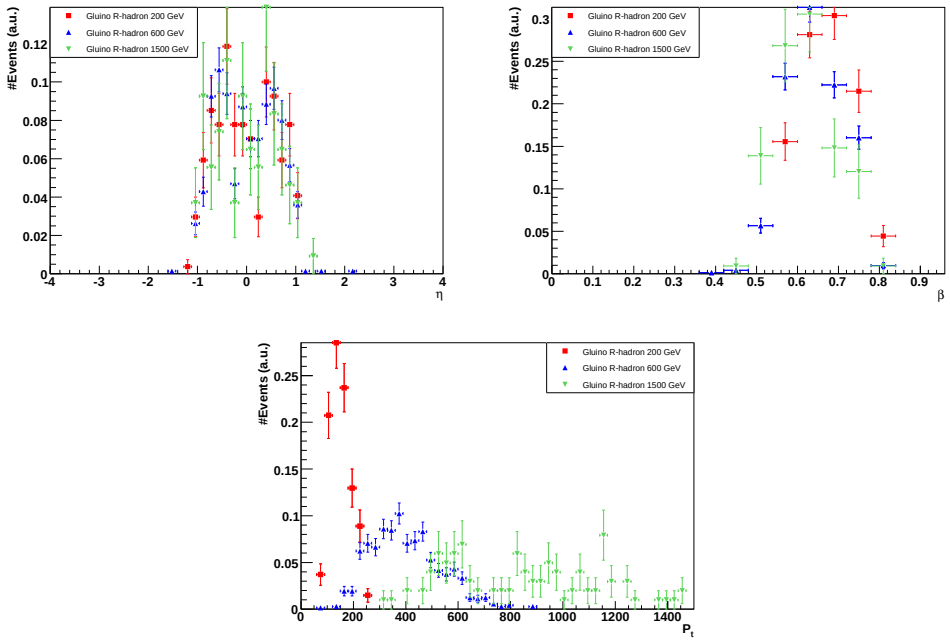

Figure 4.25: From left to right and up to down, the plots are distributions of the η, β, p_T in gluino R-hadron events, after final data selection in combined analysis.

Table 4.4: HSCP selection efficiencies for reconstructed masses $m > 100$ GeV. The standard cut $\sigma_{\beta^{-1}} < 0.1$ is also applied in the second, third and fifth columns. The last column shows the efficiency with a tighter cut on the β_{DT} error (as a reference). The selection efficiency used in the next section is the one quoted in bold in the fifth column.

Sample	$\beta_{DT} < 0.85$	$\beta_{DT} < 0.80$	$\beta_{Tk} < 0.80$	$\beta_{DT} < 0.80$ and $\beta_{Tk} < 0.80$	$\sigma_{\beta^{-1}} < 0.07$
g200	0.079	0.069	0.130	**0.062**	0.053
g300	0.097	0.088	0.172	**0.081**	0.069
g600	0.117	0.109	0.235	**0.103**	0.088
g900	0.141	0.136	0.255	**0.126**	0.110
g1200	0.128	0.126	0.240	**0.111**	0.090
g1500	0.137	0.136	0.285	**0.117**	0.102
kk300	0.342	0.287	0.465	**0.264**	0.239
stop130	0.079	0.067	0.116	**0.060**	0.053
stop200	0.098	0.083	0.159	**0.078**	0.067
stop300	0.122	0.108	0.205	**0.101**	0.088
stop500	0.145	0.130	0.258	**0.119**	0.105
stop800	0.170	0.156	0.305	**0.148**	0.129
stau156	0.332	0.236	0.331	**0.199**	0.182
stau247	0.452	0.347	0.491	**0.298**	0.269

We see the clear η cutoffs around 2.4 for skim level and 1.0 for final selection, which correspond to SST and DT geometric coverage limits. One can also see the clear β cutoffs after skim ($\beta >$0.5) and final selection($\beta < 0.8$), which result in the efficiency loss in the lower end of p_T distributions.

In the case where the tails of the two β distributions are higher when measured on data than expected from simulation, a tighter selection can be used. The goal is to have less than one background event expected for 1 fb^{-1}. Several additional cuts can be used which drastically reduce the background but have only small effects on the signal. Their effects on the background cannot be properly investigated with the available statistics because the proposed simple selection leaves no events. The cut on $\sigma_{\beta^{-1}} < 0.1$ can be made

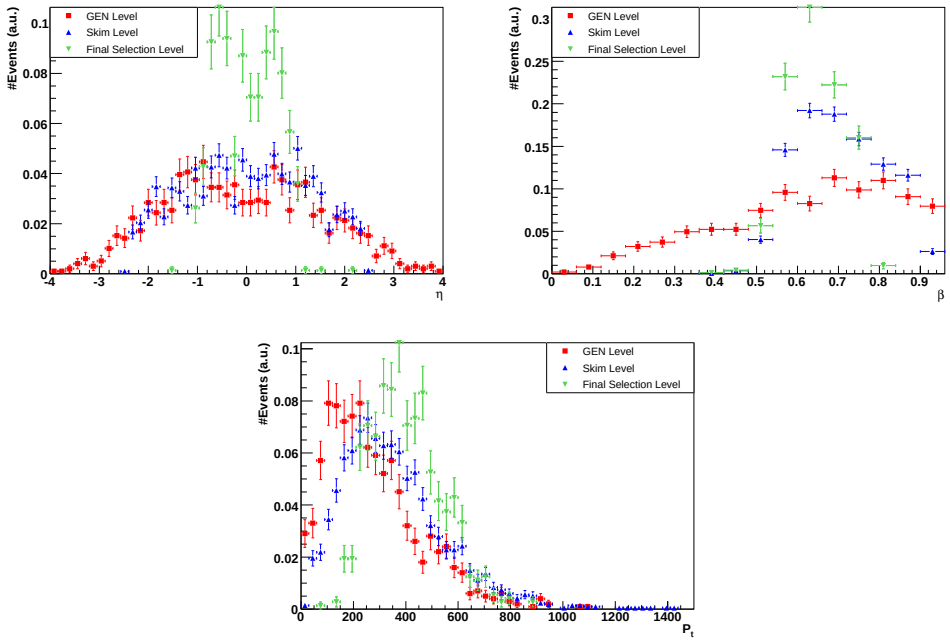

Figure 4.26: From left to right and up to down, the plots are distributions of the η, β, p_T in 600 GeV gluino R-hadron events, in generation level, in skim level, and after final selection in combined analysis.

tighter, e.g. $\sigma_{\beta^{-1}} < 0.07$, to further reduce the DT tails. This cut reduces the signal efficiency by about 10% as reported in Table 4.4. The tails of the β measurement obtained with the tracker ionization can be reduced with a tighter cut on the number of hits available to compute the track dE/dx. As shown in Fig.4.22 a cut of $|\beta_{DT} - \beta_{Tk}| < 0.1 \div 0.2$ can also be applied, with a reduction of the signal of only a few percent. Finally, a tighter cut on the reconstructed mass value, according to the mass range being searched, can be applied, such as requiring $m > 200$ GeV or $m > 400$ GeV instead of $m > 100$ GeV.

The selection used for this dissertation is not to be considered final and must be optimized once tails of the velocity measurement are determined using real data.

4.5.2 Standalone tracker

A standalone tracker dE/dx analysis can be performed as a cross check if no signal is observed in the combined analysis or in case of a problem with the DT during early data taking.

The analysis is based on simple cuts on the energy deposition and particle momentum. An additional requirement of compatible muon hits (even if no TOF is extracted from the muon detectors) is used to improve the rejection. Tracker tracks and muon tracks are associated as explained in the previous section, then the following selection is applied:

- A muon with $p_T > 100$ GeV
- $\beta_{tk} < 0.8$

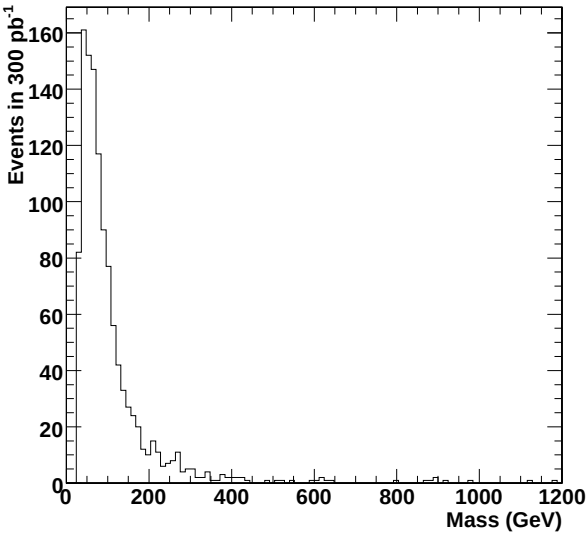

Figure 4.27: The reconstructed mass spectrum using the tracker standalone selection for background events.

For the tracker analysis, only the events selected from the muon primary dataset are used. While the combined selection is limited to the barrel region in which the drift tube measurements are available, the tracker standalone selection can recover some efficiency in the forward region. The geometrical acceptance of the tracker extends to $\eta = 2.4$.

The spectrum of reconstructed masses for background is shown in Fig.4.5.2. Table 4.5 gives the efficiency of the above selection for the signals and the number of background events above a given mass threshold.

4.5.3 Standalone DT

A standalone selection using only the DT detector can be made which is similar to that presented above for the Tracker. The rejection of muons from

Table 4.5: Number of selected background events in 1fb^{-1} (upper part of the table) and efficiency of selecting signal events with the tracker standalone selection (lower part). The numbers in bold are the operating points considered for the results in the next chapter.

Background				
Sample	soup	$m > 100$ GeV	$m > 200$ GeV	$m > 400$ GeV
PDMuon	chowder	132	30	0
	gumbo	525	279	84
	stew	24	9	0
total	all soups	681	318	84

Signal				
Sample	mass(GeV)	$m > 100$ GeV	$m > 200$ GeV	$m > 400$ GeV
gluino	200	**0.078**	0.032	-
	300	0.108	**0.107**	0.001
	600	0.142	0.142	**0.138**
	900	0.121	0.121	**0.121**
	1200	0.097	0.097	**0.097**
	1500	0.105	0.105	**0.105**
KK	300	0.416	**0.412**	0.002
stop	130	**0.045**	0.001	-
	200	**0.095**	0.038	0.001
	300	0.138	**0.137**	0.001
	500	0.167	0.167	**0.154**
	800	0.187	0.187	**0.186**
stau	156	**0.213**	0.003	-
	147	0.413	**0.379**	-

the LHC is expected to be better here than for the tracker-only selection if the same cut $\beta < 0.8$ is applied. Nevertheless, a standalone DT analysis suffers additional background due to cosmic muons. Indeed, while this background is negligible if we require an highly ionizing track associated with the muon, it can be a problem if such information is not available. A DT standalone analysis is especially useful to study the possibility of recovering R-hadrons which are produced as neutrals (so they will not have any signal in the tracker) and later flip to charged particles after interacting in the calorimeters.

To get rid of cosmic background, one can make use of impact parameter distributions, as the cosmic background should not peak in r (the $r - \phi$ plane perpendicular to the beam direction) and z (beam) directions. One can follow the sideband method used in anti-deuteron measurements by CLEO in Ref. [58] to remove the cosmic background, and even the possible beam gas and physics gas backgrounds mentioned in the same Ref. [58].

Chapter 5

Results and Conclusions

5.1 Discoveries or Exclusions for HSCPs at CMS

From previous discussions, the CMS detector can measure momentum up to the TeV scale (2 TeV conservatively), and the sensitive region for β measurements for this analysis is about 0.6 – 0.8.

To detect those slow particles with $\beta < 0.5$ (normally corresponding to high mass $\gtrsim$ TeV HSCPs), we might want to use a dE/dx trigger. For such a slow particle, it can't reach the muon system in the 25 ns bunch crossing time window. So if we use the muon trigger only, chances are the HSCP will not be triggered due to the quality cuts introduced during the L1 and HLT processes. Even if the muon trigger condition is met when the slow particle arrives at the muon system, and the data taking is started, the HSCP will be assigned to a later event. Thus, the relevant information on the slow particle from the

tracker detector and calorimeters is probably already lost. The dE/dx trigger won't have the above problem, as the tracker is very near to the interaction point. Even a very slow particle can still reach several layers of the tracker in time. For example, a $\beta = 0.1$ particle can travel 0.95 m in 25 ns, and the CMS tracker is located within a radius of 1.2 m. The dE/dx trigger is also better than the JETMET trigger, as the latter depends on particular models. So the dE/dx can be a model-independent and very efficient trigger without loss of the full event information. Nevertheless, there's also a problem for the dE/dx trigger. A slow particle with $\beta \leq 0.3$ may possibly saturate the electronics even when the cluster sharing is considered, because it can produce an energy deposition equivalent to ≥ 10 MIP, according to Eq. 4.3. The CMS SST can only endure 3.2 MIPs in the 320 μm modules and 2 MIPs in the 500 μm modules and a cluster is normally shared between 3 – 4 strips. Unfortunately, there's no dE/dx trigger utilized at CMS currently.

Based on the current β sensitivity, the mass range CMS can reach can be up to 2.5 TeV, as shown in the left plot of Fig. 5.1, solving mass with the mathematical relation in Eq. 4.1, i.e., $m = \frac{p}{c}\sqrt{\frac{1}{\beta^2} - 1}$. Unfortunately, we don't simulate any events with mass greater than 1.5 TeV. We do not provide any conclusion on the discovery potential for the mass region between 1.5 TeV and 2.5 TeV, although it may be reachable. Instead, we present results from both the combined selection and the tracker standalone selection. We don't show any results from the DT standalone analysis, as it is still a work in progress.

For the combined analysis, all backgrounds are removed after the nominal cuts, as studied in Sec. 4.5.1. Currently, no clear guidelines are available

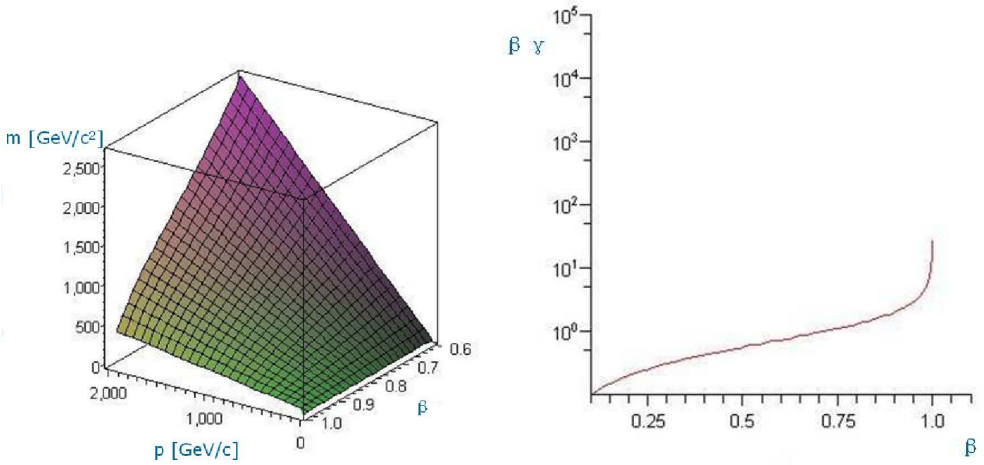

Figure 5.1: The left plot is the mathematical relation between a particle's mass, β and momentum: $m = \frac{p}{c}\sqrt{\frac{1}{\beta^2} - 1}$. The right plot shows the relation between $\beta\gamma$ and β: $\beta\gamma = \frac{\beta}{\sqrt{1-\beta^2}}$.

in CMS for the definition of a discovery when zero background events are expected. In the following discussion, we will compute the luminosity needed to observe 3 events in the signal region for different models. The Poisson probability to observe no events when 3 are expected is 5%. Therefore, we can claim a 95% C.L. exclusion, if no events are observed when the luminosity for 3 events has been accumulated. If an excess is observed it is also possible to perform several cross checks. First, one can check the distribution of the reconstructed mass, as in the right plot in Fig. 5.2, and see if it peaks reasonably. Second, one can check the sidebands of other variables (p_T, impact parameters, β, etc.) and make sure the signal is not faked by some unknown source.

The left plot in Fig. 5.2 shows the required luminosity to detect three heavy stable charged particles for different signal samples. The error bars

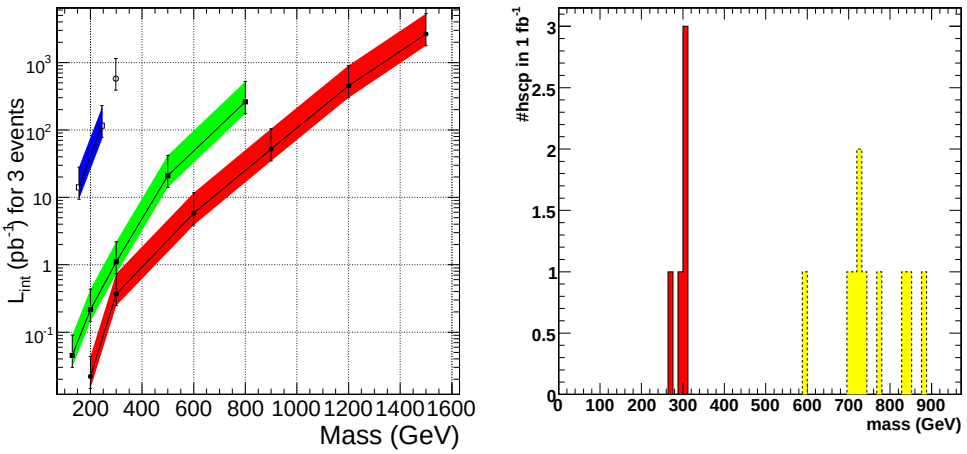

Figure 5.2: The left plot shows the integrated luminosity (pb^{-1}) needed to observe 3 events, for the four signal models (red color is for gluino, green is for stop, blue is for stau, and black is for the KK tau) as a function of HSCP mass. The right plot shows the mass distributions with 1 fb^{-1} for two of the lowest cross section samples (300 GeV KK tau and 800 GeV stop).

correspond to a systematic uncertainty on the trigger efficiency of 50%. The right plot in the same figure shows the mass distributions with 1 fb^{-1} data for two of the lowest cross section samples (300 GeV KK tau and 800 GeV stop).

For the tracker standalone analysis, the luminosity needed for a 95% C.L. exclusion has been computed with a likelihood ratio method [59]. To claim a discovery, we require at least 3 events and $\frac{S}{\sqrt{B}} \geq 5$, once we observe a peak above the long SM muon tail. These results are shown in Fig. 5.3.

To ease the comparison with previous L3 and CDF results in Fig. 1.6, we also show the 95% CL cross section limits that CMS can achieve for the four models we considered, under the scenarios of an integrated luminosity of 100 pb^{-1} or 1 fb^{-1}. The limits are shown in Fig. 5.4. We see, that CMS is

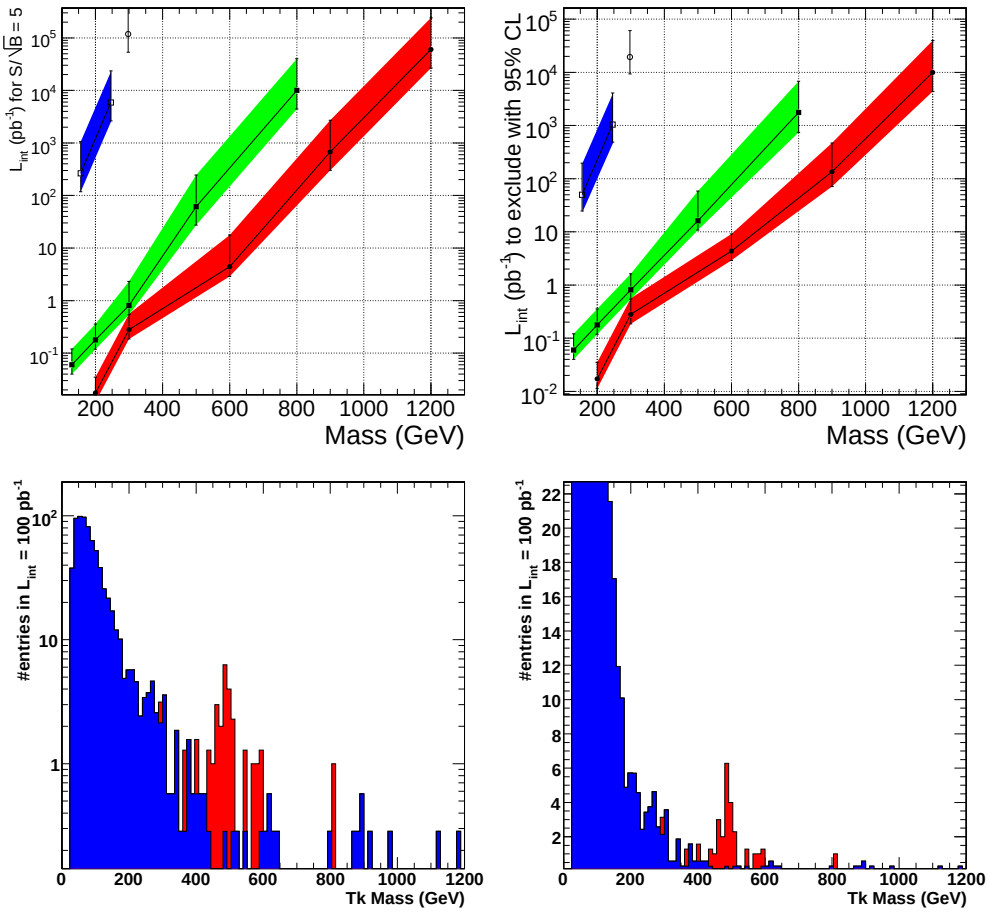

Figure 5.3: Luminosity required for discovery (upper-left) or exclusion (upper-right) using the standalone tracker analysis, and reconstructed mass (signal plus background) in 100 pb^{-1} for a 500 GeV stop (lower-left plot is in log scale, lower-right plot is in linear scale).

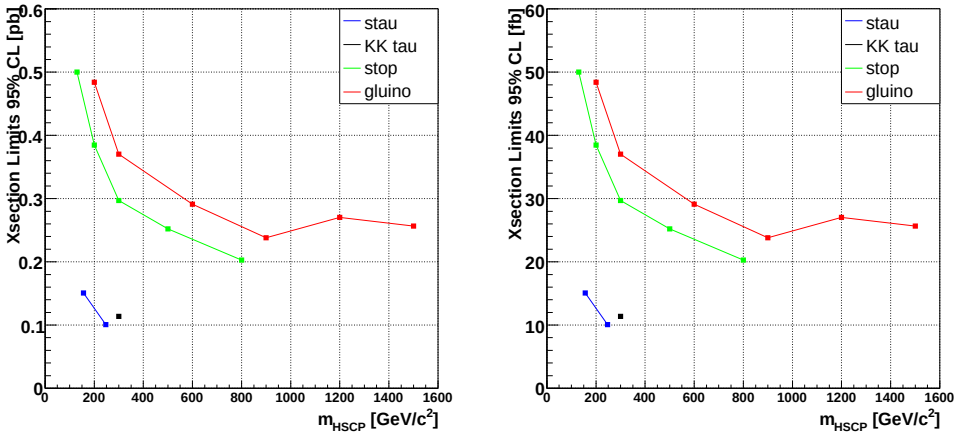

Figure 5.4: The left plot shows cross section upper limits at the 95% CL with 100 pb^{-1} data for the four signal models. The right plot shows same limits but with 1 fb^{-1} data.

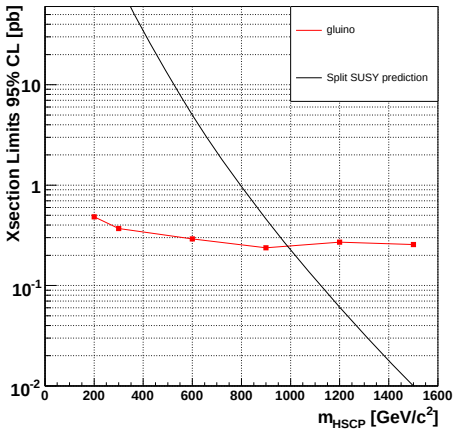

Figure 5.5: Data points are cross section limits CMS can achieve with 100 pb^{-1} data and the curve corresponds to Split SUSY prediction.

capable of giving better cross section limits than CDF with only 100 pb^{-1} of data. And with 1 fb^{-1} of data, we expect to exclude most of the parameter space for the four models we considered, giving mass limits up to 1.5 TeV.

To get a more direct comparison between our cross section upper limit and theoretical model prediction, in Fig. 5.5, we show the cross section upper limit we can get with 100 pb^{-1} data and the corresponding theoretical prediction from Split SUSY model. We see clearly that with 100 pb^{-1} data, the gluino mass can be exluded to 1 TeV if we don't find any signal events.

5.2 Systematic Error Discussion

The first source of systematic uncertainty, probably the biggest, is the trigger efficiency for late particles. The specific muon trigger settings for time gates and synchronization may change the efficiency for triggering on a late particle in the correct bunch crossing. This can easily change the trigger efficiency by 50% and can shift the spectrum of the detectable HSCPs towards higher values of β, further reducing the final efficiency. It should be noted that the MET trigger does not suffer from this problem and can in principle recover some of the lost events. This loss of efficiency from the muon trigger has the same effect as an uncertainty on the signal cross section, assuming that some slow particles have caused a trigger. For R-hadrons, the charge flipping effect may also result in big systematics on the efficiency. As mentioned in Sec. 3.2.2, the *CustomPhysics* we use in detector simulation only considers R-hadrons with u, d quarks, and the possible heavier flavor content (s, c or b quarks) is always neglected. Therefore, this efficiency depends on the s

quark suppression which is taken to be 30% by Ref. [60]. So we may have another efficiency loss due to the omission of s, c or b favored R-hadron interactions. Nevertheless, even if the efficiency loss affects the integrated luminosity needed for discovery/exclusion, it does not change the background behavior.

Another source of systematic uncertainty comes from the evaluation of the tails of the β distributions as measured with the tracker and with the DT. The DT drift time and tracker dE/dx calibrations during physics data taking can surely change the β resolutions, and thus the final mass resolution. As we are to look for a possible small peak above a huge near-exponentially decreasing tail in the mass distribution, even a slightly poorer β resolution can make the tail in the mass distribution much bigger. In this dissertation, we assume that the number of background events populating those tails is predicted by the simulation. And we also showed that the MC simulates the right tail of SM muons pretty well, using TIF data. Nevertheless, those tails will be directly measured on data at the start of data taking. One can use a control sample which is identical to the search sample but at lower momentum ($p < 35$ GeV for example) where signals would not contribute, and measure the fraction of tracks in the control sample which fluctuate to low β values. One might also want to vary the momentum and η cuts and check the possible momentum and angular dependence on the fake rate fraction. Another way to estimate the background contribution is to use the triangular background method used in the anti-deuteron measurement by the CLEO collaboration in Ref. [58], after we find a signal peak in the physics data.

The misalignment is expected to affect the momentum measurement and thus our final mass measurement for HSCPs. To study this effect, in both the CSA07 background and HSCP signal samples, we perform reconstructions with the so called 10 pb^{-1} conditions, which assume that the detector has been realigned by using the first 10 pb^{-1} of integrated luminosity. This assumption is pessimistic for luminosity of the order of 1 fb^{-1}. We found no difference for our final results after taking the 10 pb^{-1} condition into account. So the systematic error from misalignment is negligible for this analysis.

Additional uncertainties related to the generation and simulation of events, such as parton distribution functions, higher order corrections and background rate uncertainties have not been studied. Furthermore, tracking systematics and luminosity uncertainties are not taken into account in calculating the cross section limits. No attempt has been made to quantify these kinds of uncertainties. But given the many and very distinctive signatures of HSCPs, these systematics are expected not to have a dramatic impact on the abilities for discovering HSCPs.

5.3 Results from ATLAS

The ATLAS collaboration has also studied the possibility of HSCP detection at LHC. The most recent public result can be obtained from Ref. [61]. A detailed discussion of R-hadron detection at ATLAS is in Ref. [62].

As shown in Fig. 5.6, the ATLAS detector consists of four major components: inner detector, calorimeter, magnet system, and muon spectrometer. The inner detector contains silicon pixel detectors (three barrels at average

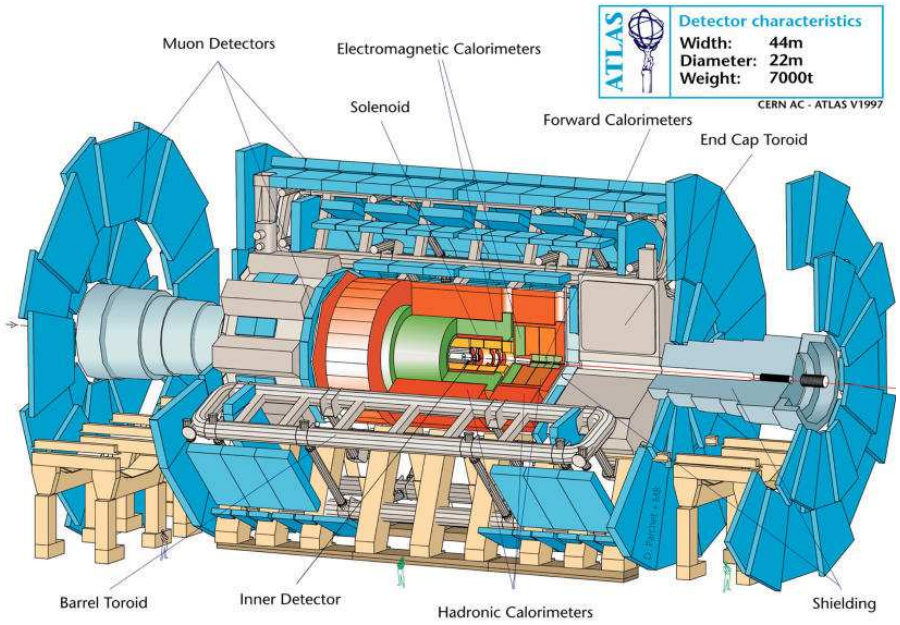

Figure 5.6: Anotated picture of the ATLAS detector.

radii of 5 cm, 9 cm, 12 cm), silicon microstrip detector (four layers of stereo silicon microstrip detectors mounted at radii of 30.0, 37.3, 44.7, and 52.0 cm), and a Transition Radiation Tracker (TRT) (which has two independent thresholds: the tracking hits will pass the lower threshold, and transition radiation hits pass the higher one, used to identify electrons). Altogether, the inner detector provides seven precision space points per track (three from the pixels and four from the SCT) to be combined with the other 36 hits in the TRT, ensuring a coverage up to $|\eta| < 2.5$ [63]. The ATLAS calorimeter has two sections, the inner section uses liquid argon as the sensing element, and the outer section sensors are tiles of scintillating plastic. So the two sections serve as ECAL and HCAL respectively. The ATLAS muon spectrometer is composed of Monitored Drift Tubes (MDT) and RPCs for the

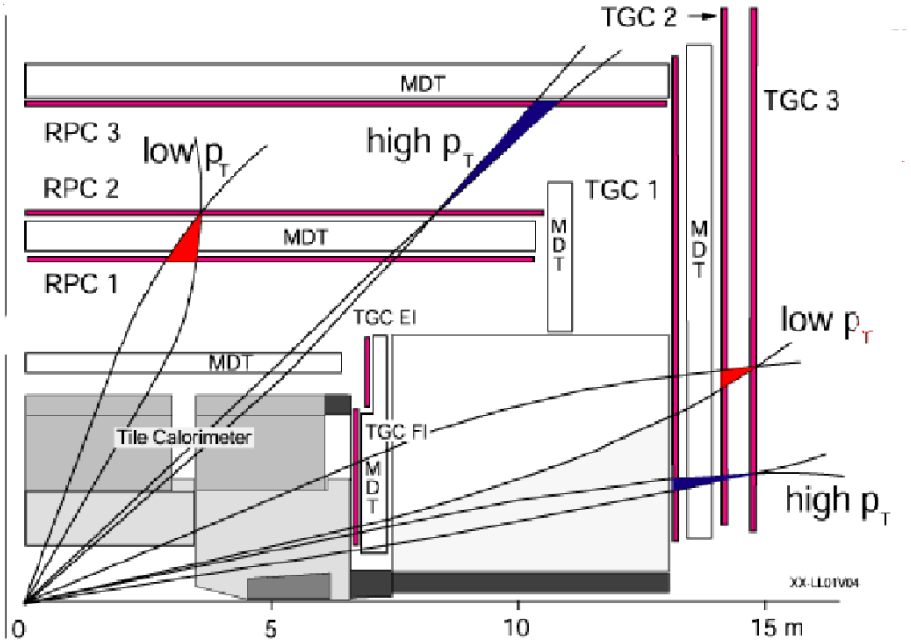

Figure 5.7: ATLAS muon system.

barrel part, and MDTs and Thin Gap Chambers (TGC, endcap trigger) for the endcap [64], as shown in Fig. 5.7. The CMS muon system uses DTs and RPCs for the barrel and CSCs and RPCs for the endcap. Therefore, for the muon standalone search, ATLAS can measure the β in its full fiducial coverage, $|\eta| < 2.7$, using the TOF information from the MDT, while CMS can only measure β in the barrel DT region with $|\eta| < 0.9$.

The ATLAS detector is 22 m in diameter. So for a $\beta = 1$ particle, it needs more than 50 ns to pass through the whole detector. And considering the LHC bunch spacing time of 25 ns, three events will coexist in the detector at the same time. Therefore, corrected bunch crossing identification is crucial to HSCP study at ATLAS.

The most recent HSCP study by ATLAS [61] included two models: a

GMSB5 model in which the stau and selectron are co-NLSPs (mass point: $M_{\tilde{\tau}} = 102.2$ GeV, $M_{\tilde{e}} = 100.3$ GeV) and a Split SUSY gluino model (mass range: 100 GeV – 2 TeV). The stau result is not mature, the only public results are the reconstructed mass and velocity of the stau, using the muon trigger with TOF information (similar techniques used as the CMS DT TOF one), as shown in Fig. 5.8.

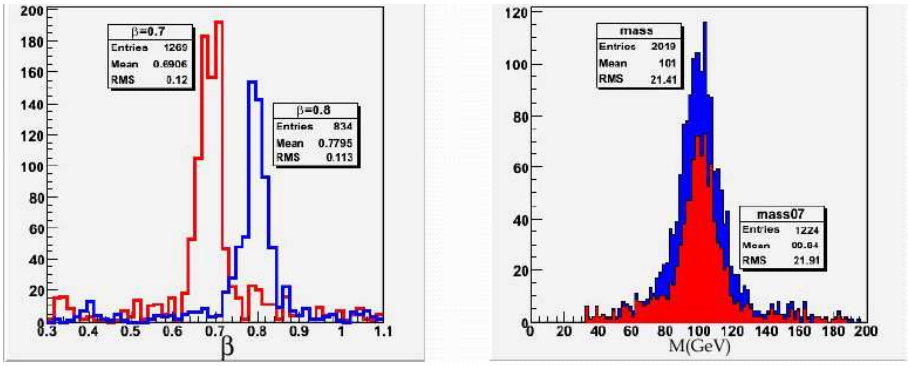

Figure 5.8: ATLAS stau results: the left plot is the reconstructed β and the right one is the reconstructed mass.

For R-hadrons, ATLAS has a more detailed study in Ref. [62]. The method for R-hadron detection at ATLAS uses the muon system only, requiring the TOF with respect to a particle with $\beta = 1$ to be larger than 3 ns (the time resolution is 1 ns for ATLAS MDTs). The R-hadrons can be discovered by observing an excess over the SM events in missing E_T and scalar E_T sum distributions. Under this scenario, R-hadrons can be discovered for masses up to 1400 GeV for an integrated luminosity of 30 fb^{-1} assuming low luminosity running. The results are shown in Fig. 5.9.

The same Ref. [62] also mentions some possible identification methods of HSCP using other subdetector information. Fig. 5.10 shows the ratio E/p

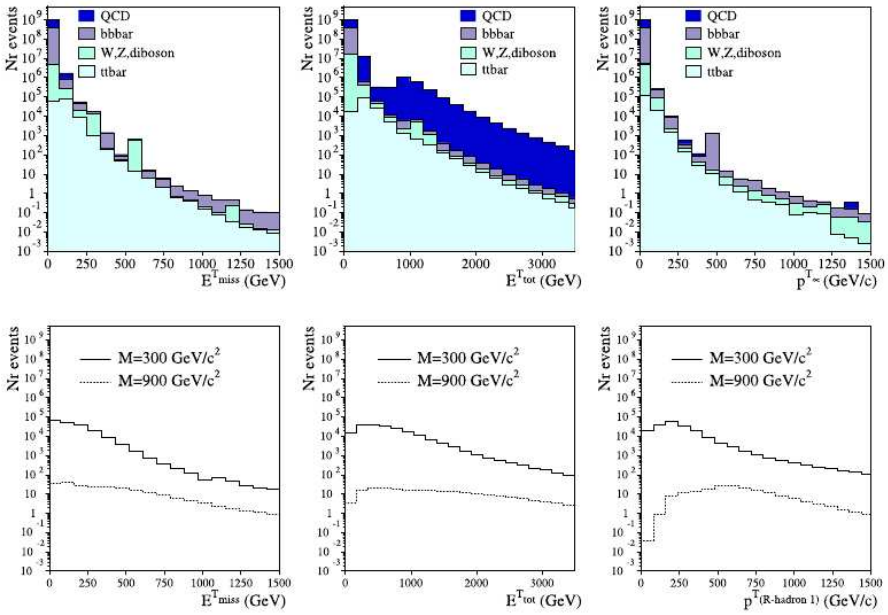

Figure 5.9: ATLAS R-hadron results: the missing transverse energy (left), the total visible energy distributions (middle) and the p_T (right) distributions after high level trigger requirements for background (top) and R-hadron signals with masses of 300 and 900 GeV (bottom). The number of events corresponds to an integrated luminosity of 1 fb^{-1}.

measured from the ATLAS ECAL for R-hadrons, muons, pions, and electrons in the ATLAS barrel at $|\eta|$ =0.1. The two extreme cases (around 0 or 1) are represented by the muons (solid line) and the electrons (dotted line).

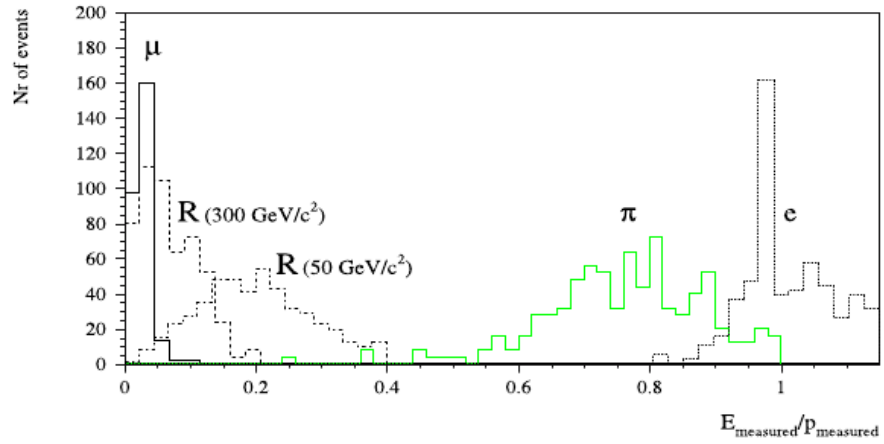

Figure 5.10: The ratio E/p for R-hadrons, muons, pions and electrons in ATLAS barrel at $|\eta|$ =0.1.

Ref. [62] also mentions possible HSCP detection using the hits information from the TRT detector. They don't measure dE/dx directly from the SCT and pixel detectors due to the limited number of hits (three from the pixels and four from the SCT, compared with normally 36 hits in the TRT). Hits in the ATLAS TRT detector are registered using two discriminator levels: a low threshold level, corresponding approximately to 200 eV, and a high threshold (HT) level, corresponding to a transition radiation photon of about 5 KeV. The left plot in Fig. 5.11 shows the average number of hits as a function of $\beta\gamma$ for a particle in the ATLAS central pseudo-rapidity region. We see HT hits can play a role for R-hadron identification only for $\beta\gamma < 1$, or $\beta < 0.7$ (can be obtained from right plot of Fig. 5.1). On the other hand, the number

of HT hits can be used to separate fast R-hadrons with $\beta > 0.7$, when they are minimum ionizing, from very high p_T muons ($p_T > 200$ GeV/c) which start to emit transition radiation photons. The behavior of HT hits as a function of $\beta\gamma$ in the left plot of Fig. 5.11 is very similar to the $\beta\gamma$ curve for muon dE/dx in Cu, in Fig. 4.1. To be more fair in the comparison, the right plot of Fig. 5.11 shows the most probable energy loss in silicon as a function of $\beta\gamma$ [7], scaled by the mean loss of a minimum ionizing particle. We see, the dE/dx in silicon can help in particle identification for $\beta\gamma < 3$, or $\beta < 0.85$. This shows the CMS SST dE/dx measurement has larger sensitive range than the ATLAS HT hits measurement.

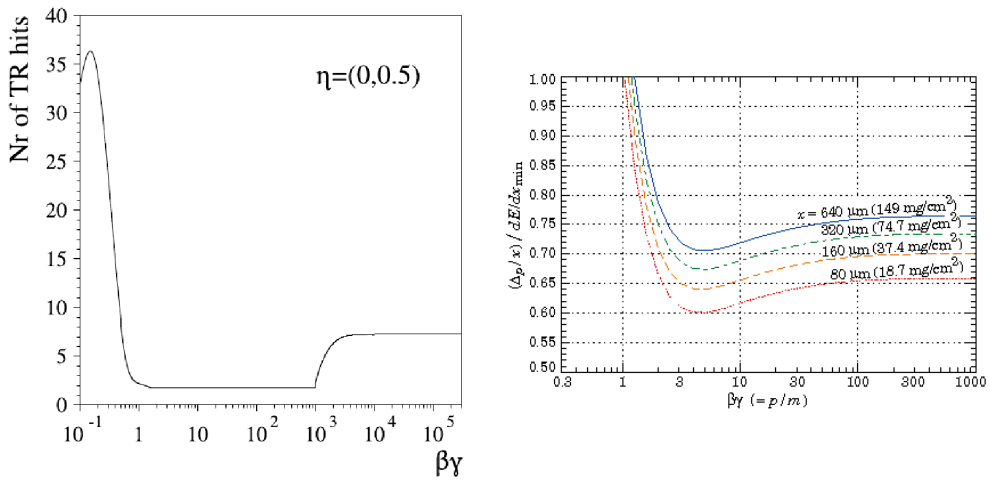

Figure 5.11: The left plot shows the average number of HT hits as function of a particle's $\beta\gamma$ in the central pseudo-rapidity region of the ATLAS detector. We see HT hits can play a role for HSCP identification only for $\beta\gamma < 1$ or $\beta < 0.7$. The right plot shows the most probable energy loss (dE/dx) in silicon with different thickness x as function of $\beta\gamma$, scaled by the mean loss of a minimum ionizing particle. We see dE/dx can play a role for HSCP identification for $\beta\gamma < 3$ or $\beta < 0.85$.

Therefore, both CMS and ATLAS can detect HSCPs but with different

strengths. CMS has developed mature techniques for SST dE/dx and DT TOF. By combining the two, the background rejection is optimal. CMS is capable of discovering the mGMSB stau and low mass gluino/stop with just a few hundred pb^{-1} data. With about 1 fb^{-1} of data, CMS is sensitive to gluino masses above 1 TeV and KK taus. ATLAS currently only uses the TOF information from MDTs in the muon system, and the only public result is on gluino R-hadrons, which can be discovered for masses up to 1400 GeV for an integrated luminosity of 30 fb^{-1}, assuming low luminosity running.

Due to the different methods used in the ATLAS (MDT only analysis) and CMS (DT and Tracker Combined analysis) collaborations, it's not possbile to make a direct comparision between the two experiments. The ATLAS MDT analysis can be compared to the CMS muon standalone analysis. As the MDT time resolution is 1 ns, which is same as the CMS DT time resolution, the ATLAS MDT can, in principle, obtain similar β sensitivity as the CMS DT analysis. And ATLAS η coverage is much larger, compared to the fact that the CMS DT only covers the barrel part. So ATLAS can obtain higher efficiency than CMS in measuring the neutrally produced R-hadrons when they flip to charged in the muon system, with better η coverage. But still, the ATLAS HSCP analysis has to deal with more backgrounds than the CMS combined DT and Tracker analysis.

Finally, both CMS and ATLAS are working on possible identification methods using other parts of the detectors. The inclusion of new identification methods in the analysis could result in higher efficiency and better S/N ratios.

5.4 Conclusion

In this dissertation, we report on a detailed study of the discovery potential for heavy stable charged particles of the CMS detector at the LHC Four benchmark theoretical models are used: gluino R-hadron in split SUSY, stop in MSSM, KK tau in MUED and stau in mGMSB. Searches for HSCPs could be among the very first analyses that CMS can perform. HSCPs have distinctive detector signatures (large ionization energy loss in the silicon strip tracker and time delay in the drift tubes of the muon system), expected high cross sections (in the order of pb), and relatively simple experimental challenges (essentially a single track based analysis).

We showed in detail that the CMS detector is capable of discovering the mGMSB stau and low mass gluino/stop with just a few hundred pb^{-1} of data, which can be accumulated within 2 months running during the pilot physics run at LHC, scheduled to start in the Winter of 2008. With about 1 fb^{-1} of data, CMS is sensitive to gluino masses above 1 TeV and KK taus. We also discussed that by incorporating the possible ECAL and CSC subdetector information in the analysis, we can improve the efficiency and gain more power on background rejection.

In conclusion, we expect to either discover HSCPs or exclude them up to the 1 TeV mass region at LHC soon after pilot physics running.

Appendix A

KK Lepton as HSCP in MUED

A.1 Parameter Space for Long-lived KK Leptons

The Minimum Universal Extra Dimension (MUED) theory is defined in 4+1 dimensions, with only three free parameters: R (radius of extra dimension), Λ (cut off energy scale) and m_{higgs} (SM Higgs mass). The MUED predicts that for all SM particles there exist corresponding Kaluza Klein (KK) states in the extra one dimension. They have the same quantum numbers and spins as their SM partners. The masses of KK states follow approximately

$$m_n^2 \sim m_0^2 + n^2/R^2 + \text{boundary terms}, \tag{A.1}$$

where n is the KK excitation level, R is the radius of extra dimensions, and m_0 is the SM partner mass. KK masses are degenerate at tree level, and mass splitting is introduced from radiative corrections. Here the KK lepton

l^1 decouples by $l^1 \rightarrow l^0 + \gamma^1$, where γ^1 is the lightest KK photon (LKP in UED) and l^0 is the SM lepton.

For a certain (Λ, R) parameter space, the mass splitting can become less than the SM lepton mass. The KK leptons thus can only decay via a virtual SM W, such as $\mu^1 \rightarrow \gamma^1 + \nu_\mu^0 + \nu_e^0 + e^0$. Thus, the μ^1's life time becomes longer than the life time of the SM μ [3], and becomes one kind of lepton-like HSCP. From experimental limits (direct search and EW precision measurement constraints), $R^{-1} >\sim 300$ GeV [22] or 250 GeV [23] assuming a heavy Higgs.

To study the parameter space where KK leptons become charged stable particles in MUED, we just need to calculate the total width of the KK lepton. If the width becomes small enough, $< 10^{-17}$ GeV ($\Gamma \times \tau = \hbar = 6.58 \times 10^{-25}$ GeV, if $\tau >\sim 100$ ns then $\Gamma <\sim 10^{-17}$ GeV), then its lifetime is long enough to escape the CMS detector, and it becomes a long-lived particle.

We use the CompHEP [39] and MUED model file [40] provided by KC Kong. We only calculate the 2 body decay (dominant) width of KK leptons with the process $e_L^1(e_R^1/\mu_L^1/\mu_R^1/\tau_L^1/\tau_R^1) \rightarrow 2 \times x$ in CompHEP. Here, the superscript 1 means they're first level KK leptons and subscript L/R is left handed or right handed. The $2 \times x$ enables us to select any two-body decays of the KK lepton. We vary the MUED parameter ΛR (product of parameters Λ and R) and see what maximum R^{-1} is required to make the KK lepton long-lived. Here we fix the Higgs mass to 120 GeV. Fig. A.1 shows the width variation of μ_R^1 with respect to R^{-1}. We can see at R^{-1} around 120 GeV, the μ_R^1 width goes to 0 and thus becomes long-lived.

Similarly, we can get the R^{-1} condition for other KK leptons. The re-

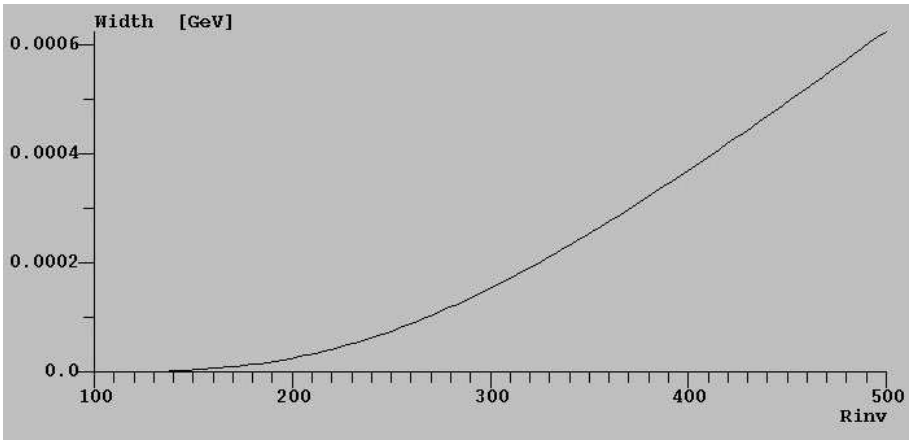

Figure A.1: Width of μ_R^1 vs. R^{-1}.

quired R^{-1} values for different KK leptons to become long lived ($\Gamma <\sim 10^{-17}$ GeV) are shown in Table A.1, where e_L^1 is not listed because the R^{-1} required is even smaller.

Together with the experimental limits on $R^{-1} >\sim 300$ GeV [22], we conclude that no lefthanded KK leptons can be HSCP candidates, and only right-handed τ_R^1 with $R^{-1} \sim 300$ GeV can become an HSCP candidate.

A.2 Cross section and Event Topology for KK τ

The dominant mode for KK lepton production is direct pair production. At the LHC, it's $pp \to \tau_R^1 \bar{\tau}_R^1$, where $\bar{\tau}_R^1$ is the antiparticle of τ_R^1.

In principle, the KK Z (Z^1) boson can also decay into τ_R^1 and a SM τ through mixing with a KK hypercharge gauge boson (B^1), as shown in Fig. A.2 from Ref. [65]. But at $R^{-1} =\sim 300$ GeV, the mixing angle is

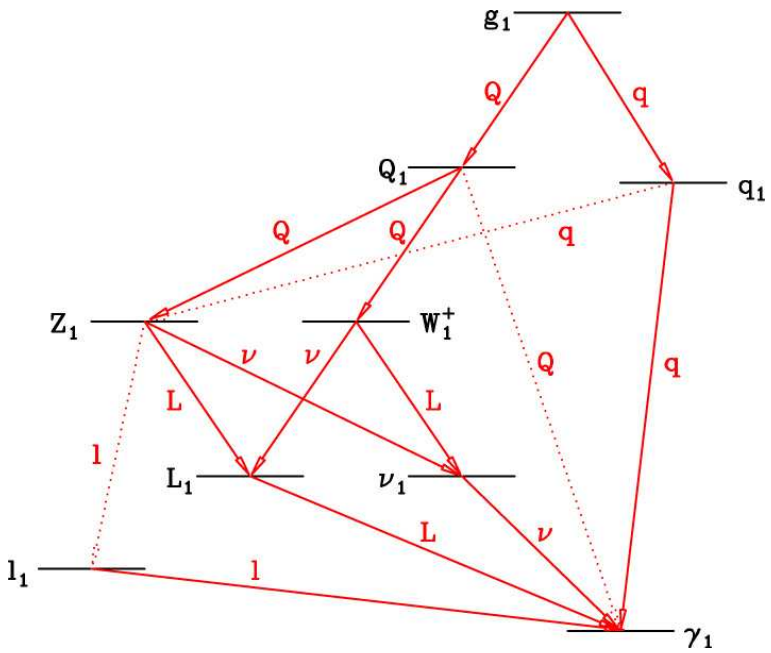

Figure A.2: The decay cascades of the level 1 KK modes in the MUED model, depicting the dominant (solid) and rare (dotted) transitions and the resulting decay products. Note the notation used here is different from the text. The upper case letter is for left-handed, and lower case letter is for right-handed. The subscript 1 indicates a level 1 KK particle. Letters without subscript are SM particles. See reference in text.

Table A.1: R^{-1} requirement for KK lepton to become long lived

KK lepton	ΛR	required $R^{-1} <$ GeV
τ_L^1	60	70
τ_L^1	20	95
τ_L^1	10	120
μ_L^1	60	4.5
μ_L^1	20	6.2
μ_L^1	10	7.8
τ_R^1	60	245
τ_R^1	20	304
τ_R^1	10	350
μ_R^1	60	120
μ_R^1	20	138
μ_R^1	10	152
e_R^1	60	103
e_R^1	20	109
e_R^1	10	113

relatively small, so the cascade decay contribution is small compared to direct pair production.

Consider a specific case: the dominant $pp \to g^1 g^1$ (KK gluon pair) process with cross section 800 pb at $R^{-1} = 300$ GeV. The $BR(g^1 \to q_L^1)$ is 0.5 and $BR(q_L^1 \to Z^1)$ is 0.33. If we want to get two Z^1s from the decay of a KK gluon pair, then $\sigma \times$ BR = 800 pb $\times (0.5)^2 \times (0.33)^2$ is 22 pb. Now we want each Z^1 to decay into a right-handed KK tau through mixing. The $Br(Z^1 \to \tau_L^1) = 1/6$ without mixing. So $BR(Z^1 \to \tau_R^1) = 1/6 \times 0.05 = 0.008$ (because $sin^2\theta_1 = 0.05$ in Ref. [66]). Then $\sigma \times$ BRs = 22 pb $\times$ $(0.008)^2$ is 1.5 fb, which is much less than the τ_R^1 pair production cross sections, 20 fb.

There are also KK quarks (q^1) production ($pp \to q^1 q^1$) and KK gluon (g^1) production associated with KK quarks ($pp \to q^1 g^1$). They roughly have a similar order of magnitude in cross section in comparison to KK gluon

production, but it is still smaller than KK gluon process. Therefore, we expect the indirect production, $\sigma(pp \rightarrow \tau_R^1 + \bar{\tau}_R^1 + X)$ to be around ~ 4 fb. So the cascade decay may not be negligible (about 20% from naive calculation), but we don't think it is the dominant production mechanism.

Another way to get the KK tau is from the decay of level 2 KK taus. However, this cross section is about 2.4 fb for $R^{-1} = 300$ GeV. As the BR($\tau^2 \rightarrow \tau^1$) is 0.5, the $\sigma \times$BRs = 2.4 fb $\times 0.5^2 = 0.6$ fb. It is another minor addition.

Therefore, we only study the direct pair production mode. This results in a pair of back-to-back charged tracks, without missing energy and lots of jets. For the τ_R^1 from Z^1 decay, depending on where the Z^1 comes from, this kind of event can result in several extra high energy jets (g^1g^1 gives 4 jets, g^1q^1 gives 3 jets, q^1q^1 gives 2 jets). Unfortunately, the current MUED model doesn't include the rare process $Z^1 \rightarrow \tau_R^1,\ \tau^1$ which is suppressed by the Weinberg angle $sin\theta_1$ in extra dimensions. So we have no way to generate cascade τ_R^1 HSCP events, unless we ask theorists to modify their MUED model file and add in those processes.

Appendix B

Tracker DCS HV Status Online to Offline

The SiStripDCS software package inside CMSSW is used to sort out the High Voltage (HV) information from millions of conditions in the Online database (DB) and save them in a C++ class format to the offline DB, so that the reconstruction software can access it easily. CMS has developed a specific PopCon+Coral [67] service package inside CMSSW to provide a common frame for all the subdetector systems in the Online-to-Offline (O2O) processing. The Coral interface provides basic methods for accessing the online DB and performing a DB query, the query result format is coded by the user. PopCon provides two classes: PopConSourceHandler and PopConAnalyzer. All the sub-detectors will develop their specific codes by inheriting from these two classes. The PopConSourceHandler class provides a method getNewObjects(), which is called in every EDM event. Therefore, the sub-detector code is implemented inside this method.

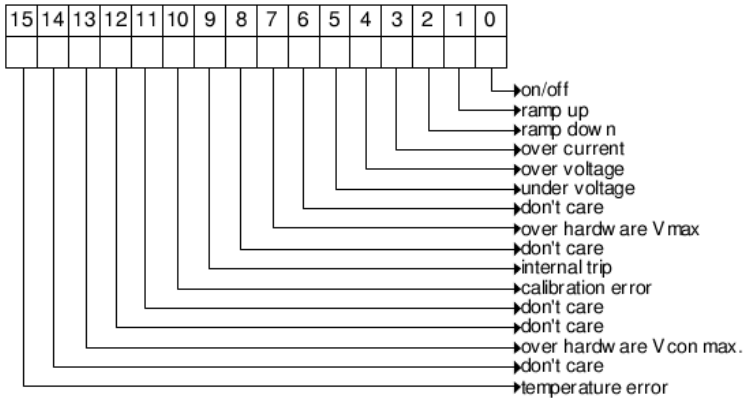

Figure B.1: Status word for CAEN power supply channels, a read access to the status item returns back a 16-bit pattern indicating channel status. The "don't care" indicates an unused bit.

For the tracker HV information, at the beginning of this getNewObjects() method, one needs first check whether the Offline DB record exists. If not, one adds a full OFF vector. Then, one gets the last Interval of Validity (IOV) append time for the corresponding HV status vector. If the current event is the last event of the current run, then one initializes the Coral interface and gets a query from last append time until this event time. The query will return the HV status information for specified detector parts, which are identified by the Detector ID (DetID) and the time when the change happens. The HV status, shown in Fig. B.1, is a 16-bit integer, indicating channel status, such as ON, OFF, Over Current etc. If the query result is empty, that means there was no HV status change during the specified time range. If the query result is not empty, the O2O code analyzes what change has been made and produces a C++ vector which contains a list of only OFF DetIDs (The reason for saving only OFF DetIDs is that we expect most of

HV to be ON during a run, thus saving only OFF DetIDs save quite a lot DB space) and puts it into the Offline DB.

Bibliography

[1] G. Giudice and R. Rattazzi. *Phys. Rept.*, 332:419, 1999.

[2] G. Giudice and A. Romanino. *Nucl. Phys. B*, 65:699, 2004.

[3] M. Byrne. *Phys. Lett.*, 583:309, 2004.

[4] M. Carena *et al. Phys. Rev. D*, 66:115010, 2002.

[5] T. P. Cheng and L. F. Li. *Gauge theory of elementary particle physics.* Clarendon Press, Oxford, 1984.

[6] L. Susskind. *Phys. Report.*, 104:81, 1984.

[7] Particle Data Group. *J. Phys. G.*, 33:1, 2006.

[8] S. Dimopoulos and D. Sutter. *Nucl. Phys. B*, 452:496, 1995.

[9] R. Barbieri *et al. Phys. Rev. D*, 66:095003, 2002.

[10] S. Dawson, E. Eichten, and C. Quigg. *Phys. Rev. D*, 31:1581, 1985.

[11] W. Beenakker *et al. Nucl. Phys. B*, 515:3, 1998.

[12] M. Fairbairna *et al. Phys. Rept.*, 438:1, 2007.

[13] S. Raby. *Phys. Rev. D*, 56:2852, 1997.

[14] K. Cheung and W. Y. Keung. *Phys. Rev. D*, 71:015015, 2005.

[15] G. Nordstrom. *Phys. Zeitschr.*, 15:504, 1914.

[16] T. Kaluza. *Sitzungsber. Preuss. Akad. Wiss. Phys. Match. Klasse.*, 1:966, 1921.

[17] O. Klein. *Nature*, 188:516, 1926.

[18] L. Randall and R. Sundrum. *Phys. Rev. Lett.*, 83:3370, 1999.

[19] I. Antoniadis. *Phys. Lett. B*, 246:337, 1990.

[20] T. Appelquist, H. C. Cheng, and B. A. Dobrescu. *Phys. Rev. D*, 64:035002, 2001.

[21] J. L. Feng, A. Rajaraman, and F. Takayama. *Phys. Rev. D*, 68:085018, 2003.

[22] T. Appelquist, H. C. Cheng, and B. A. Dobrescu. *Phys. Rev. D*, 64:035002, 2001.

[23] T. Appelquist and H. Yee. *Phys. Rev. D*, 67:055002, 2003.

[24] P. Achard *et al. Phys. Lett. B*, 517:75, 2001.

[25] D. Acosta *et al. Phys. Rev. Lett.*, 90:131801, 2005.

[26] CMS Collabration. *The CMS experiment at the CERN LHC, submitted to Journal of Instrumentation.*

[27] CMS Collaboration. *CMS Physics Technical Design Report, CERN /LHCC 2006-1.*

[28] B. J. Franek and C. Gaspar. *IEEE Trans. Nucl. Sci.*, 45:1946, 1998.

[29] PVSS II System from ETM. *http://itcobe.web.cern.ch/itcobe/Services/Pvss/.*

[30] JCOP Framework. *http://itcobe.web.cern.ch/itcobe/Projects/Framework/.*

[31] F. Hartmann. *Vienna Conference on Instrumentation 2007, http:// indico.cern.ch/getFile.py/access?contribId=160&resId=0& materialId =paper&confId=3062.*

[32] CAEN Corp. *http://www.caen.it/.*

[33] CMS Collabration. *CMS Note 2008/XXX (in preparation).*

[34] P. Baringer *et al. CMS IN 2006/042.*

[35] OLE for Process Control (OPC). *http://www.opcfoundation.org/.*

[36] The CMS Tracker Collaboration. *The Tracker Project: Technical Design Report CERN/LHCC 1998-006; The Tracker Project: TDR Addendum CERN/LHCC 2000-016.*

[37] M. L. Mangano *et al. JHEP*, 0307:001, 2003.

[38] T. Sjostrand. *Comput. Phys. Commun.*, 82:74, 1994.

[39] E. Boos *et al.* (CompHEP Collaboration). *Nucl. Instrum. Meth. A*, 534:250, 2004.

[40] K. Kong. *MUED Model, http://home.fnal.gov/ kckong/mued/.*

[41] A. Belyaev *et al. arXiv:hep-ph/0101232v1.*

[42] ROOT Analaysis Package. *http://root.cern.ch/.*

[43] CMS Collaboration. *https://twiki.cern.ch/twiki/bin/view/CMS/SWGuideFrameWork.*

[44] H. Baer *et al. arXiv:hep-ph/0312045v1.*

[45] B. C. Allanach *et al. CERN-TH/2002-020; arXiv:hep-ph/0202233.*

[46] J. Alwall *et al. JHEP*, 09:028, 2007.

[47] S. Agostinelli *et al. Nucl. Instrum. Meth. A*, 506:205, 2003.

[48] A. Mafi and S. Raby. *Phys. Rev. D*, 62:035003, 2000.

[49] R. Mackeprang and A. Rizzi. *Eur. Phys. J. C*, 50:353, 2007.

[50] C. Noeding. *CMS CR-2008/006.*

[51] R. Fruhwirth. *Nucl. Instrum. Meth. A*, 262:444, 1987.

[52] ORACLE Corp. *Oracle Relational Database Management System, http://www.oracle.com.*

[53] S. Dris, K. Gill, J. Troska, and F. Vasey. *CMS NOTE 2006/145.*

[54] A. Giammanco. *CMS NOTE 2008/005.*

[55] A. Rizzi. *CMS AN 2006/112.*

[56] W. Adam *et al. CMS NOTE-2008/XXX (in preparation).*

[57] P. Traczyk and P. Zalewski. *CMS IN 2008/XXX (in preparation).*

[58] D. M. Asner *et al.* (CLEO Collabration). *Phys. Rev. D*, 75:012009, 2007.

[59] A. L. Read. *CERN Yellow Report 2000-005-81.*

[60] T. Affolder *et al. Phys. Rev. Lett.*, 84:1663, 2000.

[61] S. Bressler. *15th International Conference on Supersymmetry and the Unification of Fundamental Interactions, http://cdsweb.cern.ch/record/1065183.*

[62] A. C. Kraan, J. B. Hansen, and P. Nevski. *Eur. Phys. J. C*, 49:623, 2007.

[63] A Tricomi. *Eur. Phys. J. C*, 33:1023, 2004.

[64] ATLAS Collabration. *ATLAS Muon Technical Design Report, http://atlas.web.cern.ch/Atlas/GROUPS/MUON/TDR/Web/TDR_chapters.html.*

[65] H. C. Cheng, K. T. Matchev, and M. Schmaltz. *Phys. Rev. D*, 66:056006, 2002.

[66] H. C. Cheng, K. T. Matchev, and M. Schmaltz. *Phys. Rev. D*, 66:036005, 2002.

[67] CMS Collabration. *Software Guide for Condition DB, https://twiki.cern.ch/twiki/bin/view/CMS/SWGuideCondDB.*